SPECTROSCOPIC STUDIES OF TWO DIMENSIONAL CARBON NANOSTRUCTURES AND SEMICONDUCTOR QUANTUM DOTS

Ni Zhenhua

NATIONAL UNIVERSITY OF SINGAPORE

2007

SPECTROSCOPIC STUDIES OF TWO DIMENSIONAL CARBON NANOSTRUCTURES AND SEMICONDUCTOR QUANTUM DOTS

Ni Zhenhua

(B. Sc. Shanghai Jiao Tong University)

A THESIS SUBMITTED

FOR THE DEGREE OF DOCTOR OF PHILOSOPHY

DEPARTMENT OF PHYSICS

NATIONAL UNIVERSITY OF SINGAPORE

2007

ACKNOWLEDGMENTS

First of all, I would like to express my sincere gratitude and appreciation to my supervisors Assoc. Prof. Shen Zexiang and Prof. Feng Yuanping for their unfailing guidance and support throughout my Ph.D project.

Great appreciations to Mr. Wang Haomin and Assoc. Prof. Wu Yihong from Department of Electrical and Computer Engineering of NUS, Dr. Pan Hui from Department of Physics of NUS, and Assoc. Prof. Han Mingyong from Institute of Materials Research and Engineering, for providing precious samples and for helpful discussions.

Thanks Dr. Fan Haiming from Department of Physics of NUS, for working together and sharing his research experience with me.

Many thanks to all my colleagues, Dr Liu Lei, Dr Yu Ting, Mr. You Yumeng, Mr. Johnson Kasim, Ms. Ma Yun, Mr. Zheng Zhe… from Raman Spectroscopy Lab of Department of Physics of NUS and School of Physical and Mathematical Sciences of NTU, for their help during my Ph.D study.

Finally but most importantly, I would like to thank my gf Bing Dan and my parents for their support and encouragement all the way.

Table of contents

Acknowledgements i

Table of contents ii

Summary vi

List of Figures ix

Publications xiii

Chapter 1 Introduction

1.1 Introduction to graphene 1

1.2 Introduction to carbon nanowalls 2

1.3 Introduction to semiconductor quantum dots 3

1.4 Objectives and significance of the studies 5

1.5 Organization of this thesis 7

1.6 References 9

Chapter 2 Introduction to Raman Spectroscopy

2.1 Basic introduction 10

2.2 Definition of Raman scattering 11

2.3 Basic theory of Raman scattering 13

2.4 Quantum model of Raman scattering 16

2.5 Resonant Raman scattering 19

2.6 Micro Raman systems 20

2.7 References 22

Chapter 3 Graphene Thickness Determination Using Reflection and Contrast Spectroscopy

3.1 Introduction 23

3.2 Experimental 25

3.3 Results and discussion 27

3.4 Conclusion 36

3.5 References 37

Chapter 4 Anisotropy of Electron-hole Pair States in Graphene Layers Observed by Raman Spectroscopy

4.1 Introduction 39

4.2 Experimental 41

4.3 Results and discussion 42

4.4 Conclusion 49

4.5 References 50

Chapter 5 Tunable Strain and Controlled Thickness Modification in Graphene by Annealing

5.1 Introduction 51

5.2 Experimental 53

5.3 Results and discussion 55

5.4 Conclusion 64

5.5 References 65

Chapter 6 Raman Spectroscopic Investigation of Carbon Nanowalls (CNWs)

6.1 Introduction 67

6.2 Experimental

6.2.1 Growth of CNWs 69

6.2.2 Experimental detail 72

6.3 Results and discussion

6.3.1 Raman characterization of CNWs 74

6.3.2 Orientation dependent Raman study of CNWs 77

6.3.3 Laser excitation dependent Raman study off CNWs 80

6.4 Conclusion 83

6.5 References 84

Chapter 7 High Temperature Raman Spectroscopic Study of Carbon Nanowalls

7.1 Introduction 86

7.2 Experimental 87

7.3 Results and discussion 88

7.4 Conclusion 96

7.5 References 97

Chapter 8 High Pressure Raman and Photoluminescence (PL) Study of ZnCdSe Quantum Dots (QDs)

8.1 Introduction 98

8.2 Experimental

8.2.1 Introduction of diamond anvil cell 100

8.2.2 Experimental detail 101

8.3 Results and discussion 103

8.4 Conclusion 113

8.5 References 114

Chapter 9 High Pressure Raman and Photoluminescence (PL) Study of CdSe/CdS QDs

9.1 Introduction 116

9.2 Experimental 119

9.3 Results and discussion 122

9.4 Conclusion 126

9.5 References 127

Chapter 10 Conclusion and Future Work

10.1 Spectroscopic studies of graphene 128

10.2 Raman spectroscopic investigation of CNWs. 130

10.3 High pressure Raman and PL spectra study of semiconductor QDs (ZnCdSe and CdSe/ZnS QDs) 131

10.4 Future work 132

Summary

This thesis presents results on spectroscopic studies of two dimensional carbon nanostructures: graphene and carbon nanowalls (CNWs). It also includes the high pressure Raman and photoluminescence (PL) studies of two popular semiconductor quantum dots (QDs): ZnCdSe alloy QDs and CdSe/ZnS core/shell QDs.

Part 1. Graphene, the one monolayer thick flat graphite, has been attracting much interest since it was firstly discovered in 2004. Graphene has many unique properties which make it an attractive material for fundamental study as well as for potential applications. In this study, firstly, we proposed a fast and precise method to identify the single-, bilayer- and few-layer graphene (<10 layers) by using contrast spectra, which were generated from the reflection of a white light source. Calculations based on the Fresnel's Law are in excellent agreement with the experimental results (deviation 2%). The contrast image shows the reliability and efficiency of this new technique. The contrast spectrum is a fast, non-destructive, easy to be carried out, and unambiguous way to identify the numbers of layers of graphene sheet, which helps future research and application of graphene.

Secondly, Raman studies of single and few layers graphene were carried out. The defect-induced D mode, two-phonon G′ mode and three-phonon G″ mode show significant broadening and blue shift as the graphene thicknesses increase. The anisotropy of electron-hole interactions in graphene was discussed and used to explain the above phenomena based on double resonance theory. The energy difference between intra- and inter- layer excitons is about ~400 meV, which were estimated from the excitation energy dependent Raman results.

Thirdly, we report the first experimental study of process-induced defects and strains in graphene using Raman spectroscopy and imaging. While defects lead to the observation of defect-related Raman bands, strain causes shift in phonon frequency. A compressive strain (as high as 3.5 GPa) was induced in graphene by depositing a 5 nm SiO_2 followed by annealing, whereas a tensile strain (~ 1 GPa) was obtained by depositing a thin silicon capping layer. In the former case, both the magnitude of the tensile strain and number of graphene layers can be controlled or modified by the annealing temperature. As both the strain and thickness affect the physical properties of graphene, this study may open up the possibility of utilizing thickness and strain engineering to improve the performance of graphene-based devices.

Part 2. Two-dimensional carbon nanowalls (CNWs) were prepared by microwave plasma-enhanced chemical vapor deposition (PECVD). The Raman observations of different sample orientations and polarizations show that CNWs are well-crystallized. Micro-Raman scattering measurements were also carried out with different excitation laser. Besides, high temperature Raman experiment on CNWs was also performed. The Raman intensity of defect-induced D mode decreased significantly after annealing, which was attributed to the removal of surface amorphous carbon by oxidation. However, the intensity of D′ mode, another defect-induced Raman mode, did not change much after annealing, indicating that the surface amorphous carbon and surface impurity do not contribute as much to the intensity of D′ mode. The dominant contributor to the D′ mode would be the intrinsic defects.

Part 3. Raman and photoluminescence (PL) studies of alloy $Zn_xCd_{1-x}Se$ (x=0.2) and CdSe/ZnS core/shell QDs were carried out under hydrostatic pressure up to 160 kbar using the diamond anvil cell technique. For ZnCdSe QDs, The structural phase

transition from wurtzite to rock-salt was observed at 71 kabr, indicated by the disappearance of both PL and Raman peaks. Besides, the abrupt change of PL pressure coefficient and Raman peak split were observed at about 25.8 kbar, which may indicate a new unidentified structural phase transition of the alloy QDs. For CdSe/ZnS core/shell QDs, two phase transition at 69 and 79 kbar were found too, which correspond to wurtzite-rocksalt and rocksalt-cinnabar structure transformation, respectively. The high pressure cinnabar structure of CdSe was predicted by theoretical calculation and first confirmed in this experiment. The experimental results of CdSe/ZnS QDs show significant difference from that of CdSe QDs as well as bulk CdSe, implying the ZnS shell play a dominant role in structure stability and electron state of such system. This part of work provides a good model for the study of structural stability of semiconductor QDs.

List of Figures

Figure 2.1 Schematic spectrum of light scattering.

Figure 2.2 Schematic diagram representing Raman scattering process.

Figure 2.3 Schematic diagram of Raman system.

Figure 3.1 (a) optical image of graphene with 1, 2, 3 and 4 layers. (b) Raman spectra as a function of number of layers. (c) Raman image plotted by the intensity of G band. (d) The cross section of Raman image, which corresponds to the dash lines.

Figure 3.2 The contrast spectra of graphene sheets with different thicknesses, together with the optical image of all the samples. Besides the samples with 1, 2, 3, 4, 7 and 9 layers, samples a, b, c, d, e and f are more than ten layers and the thickness increases from a to f. The arrows in the graph show the trend of curves in terms of the thicknesses of graphene sheets.

Figure 3.3 The contrast spectrum of single layer graphene: experimental data (black line), the simulation result using n=2.0-1.1i (red line), and the simulation result using n_G=2.6-1.3i (dash line).

Figure 3.4 The contrast simulated by using both n_G (blue triangles) and n_z (red circles), the fitting curve for the simulations (blue and red lines), and our experiment data (black thick lines), respectively, for one to ten layers of graphene.

Figure 3.5 (a) The contrast image of the sample. (b) and (c): The cross section of contrast image, which corresponds to the dash lines. The contrast values of each thickness agree well with the contrast values of one to four layers as shown in Figure 4. (d) The 3D contrast image, which shows a better perspective view of the sample.

Figure 4.1: A schematic second-order double resonance Stokes process.

Figure 4.2 (a) optical image of graphene with 1, 2, and 3 layers. (b) Raman spectra as a function of number of graphene layers, as well as the Raman spectrum of HOPG. (c) Raman image plotted by the intensity of G band. (d) The cross section of Raman image, which corresponds to the dash line.

Figure 4.3 The G′ (a) and G″ (b) bands of graphene with one to four layers, as well as those of HOPG.

Figure 4.4 (a) The excitation energy dependence of the Raman spectrum of single layer graphene. The excitation source are 325 nm (3.81 eV), 488 nm (2.54 eV), 514 nm (2.41 eV), and 532 nm (2.33 eV). (b) The G′ band frequency of single layer graphene with different excitation energy.

Figure 4.5 (a) Raman spectra of graphene with one to four layers after SiO_2 deposition. (b)The D band bandwidth (triangles) and frequency (circles) of graphene with one to four layers.

Figure 5.1 (a) Optical image of graphene with 1, 2, 3 and 4 layers. (b) Raman spectra as a function of number of layers. (c) Raman image plotted by the intensity of G band. (d) The cross section of Raman image, which corresponds to the dash lines with corresponding colors in Raman image.

Figure 5.2 (a) Raman spectra of a graphene sheet before and after the 5 nm SiO_2 top layer deposition. (b) Raman spectra of graphene with one to four layers as well as that of bulk graphite after 5 nm SiO_2 top layer deposition. (c) Raman images of graphene sheets without SiO_2 cover generated from the intensity of the D band, and (d) the G band, together with the images generated from the sample graphene sheet after the 5 nm SiO_2 top layer deposition: (e) the D band, and (f) the G band.

Figure 5.3 (a) Raman spectra of single layer graphene coated by 5 nm SiO_2 and annealed at different temperature. (b) The intensity ratio of D band and G band of graphene sheets with one to four layers (coated with SiO_2) after annealing at different temperature.

Figure 5.4 The Raman frequency of G band (a), D band (b), and 2D band (c) of graphene sheets with one to four layers (coated with SiO_2) after annealing at differenet temperature. (d) Strain on single layer graphene controlled by annealing temperature. The red line is a curve fit to the experimental data.

Figure 5.5 Optical images of a graphene sheet with one, two, three, four, and six layer regions before (a) and after (b) after annealed at 600 ^oC for 30 min. Raman (G band intensity) images of the same graphene before (c) and after (d) annealing. Contrast images of the same graphene before (e) and after (f) annealing. The one to three layer regions disappeared, while the four to six layer regions remained after annealing. The thicknesses of three remained regions were two, three, and four layers.

Figure 6.1 Schematic of micro-wave plasma enhanced chemical vapor deposition (PECVD) used to grow CNWs.

Figure 6.2 SEM images of CNWs grown on Si substrate using PECVD: (A) Top view of the CNWs. (B) Cross section of CNWs. (C) Several single layers scratched from the sample.

Figure 6.3 Raman spectrum of CNWs excited by 514 nm laser line, the insert shows the 1000-1800 cm^{-1} range, together with fitted peaks.

Figure 6.4 Raman spectra of graphite and CNWs excited by 514 nm laser line.

Figure 6.5A Raman spectra of CNWs recorded at different configurations (see Figure 6.5B) using 514 nm laser line. (a) laser perpendicular to the substrate. (b) and (c), laser parallel to CNWs film (cross section) with the polarization of (b) parallel to the substrate and (c) parallel to the growth direction of the wall. (d) and (e), laser incident normally to the surface of a scratched sample, consisting several single walls. The polarization of (d) and (e) are parallel to the wall surface but with cross direction.
Figure 6.5B Schematic diagram showing the CNWs samples, the laser and its polarization, at five different configurations (a), (b), (c), (d), (e).

Figure 6.6. Raman spectra of CNWs excited by different laser lines: 325nm(3.8eV), 488nm(2.54eV), 514nm(2.41eV), 532nm(2.33eV), and 633nm(1.96eV).

Figure 6.7 The frequencies of Raman mode (D band, 2D band, D+G band) of CNWs as a function of excitation energy.

Figure 6.8. The intensity ratio of D band to G band I_D/I_G (squares) and D′ band to G band $I_{D'}/I_G$ (triangles) with excitation energy.

Figure 7.1 (a) SEM image of CNWs grown on Si substrate using PECVD. (b) TEM image of the cross section of CNWs. The graphene planes which formed the wall were vertically aligned. There is some amorphous carbon on the surface of the wall.

Figure 7.2 Raman spectrum of CNWs excited by 532nm laser. The inset shows the 1150-1750 cm^{-1} range, together with fitted peaks.

Figure 7.3 Frequencies of Raman modes (D, G and D′) of CNWs as the temperature increases.

Figure 7.4 The relative intensity ratio I_D/I_G (a) and $I_{D'}/I_G$ (b) of CNWs at different temperature in the: first heating process, first cooling process and second heating process.

Figure 7.5 The Raman spectra of CNWs before and after the heating process. The sample was grown with the presence of a small amount of water vapor in the growth chamber, and it had narrow peak width and separated G and D′ mode.

Figure 8.1 Schematic of Diamond Anvil Cell (DAC).

Figure 8.2 PL (a) and Raman (b) spectra of $Zn_xCd_{1-x}Se$ (x=0.2) QDs at ambient pressure excited by using 532nm laser line.

Figure 8.3a PL spectra taken from $Zn_xCd_{1-x}Se$ (x=0.2) quantum dots under high pressure at room temperature. Above 71 kbar, the PL peak can not be observed because of phase transition.
Figure 8.3b PL peak energy of $Zn_xCd_{1-x}Se$ (x=0.2) QDs as a function of pressure. At 25.8 kbar, the pressure coefficient changed from 4.64 meV/kbar to 2.76 meV/kbar.

Figure 8.4a Raman spectra of $Zn_xCd_{1-x}Se$ (x=0.2) QDs at pressure of 0 kbar and 30 kbar. The smooth solid curves are the lorentzian fitting of the peaks.
Figure 8.4b Raman shift of LO mode of $Zn_xCd_{1-x}Se$ (x=0.2) QDs as a function of pressure. After 25.8 kbar, a peak splitting was observed. Above 71 kbar, the Raman peaks can not be observed because of the semiconductor-metal phase transition.

Figure 8.5a Raman spectra of $Zn_xCd_{1-x}Se$ (x=0.2) QDs before and after applying the pressure.
Figure 8.5b PL spectra of $Zn_xCd_{1-x}Se$ (x=0.2) QDs before and after applying the pressure.

Figure 9.1 (a) Absorption and PL spectra of CdSe/ZnS QDs. The insert shows the TEM image. (b) Raman spectrum of CdSe/ZnS QDs excited with the 488 nm line from an Ar^+ laser, after subtraction of the PL background.

Figure 9.2. Pressure dependence of PL peak of CdSe/ZnS QDs. (a) PL spectra at different pressure. (b) Energy and FWHM of PL peak as a function of pressure

Figure 9.3. Pressure dependence of phonon frequencies of CdSe/ZnS QDs. (a) Raman spectra at different pressure. (b) Frequency of Raman peaks as a function of pressure. Inserts show their corresponding structures at different pressures.

Publications

Journal publications

1. **Ni ZH**, Wang HM, Kasim J, Fan HM, Yu T, Wu YH, Feng YP, Shen ZX *Graphene thickness determination using reflection and contrast spectroscopy* **Nano Letters** 07(09) : 2758 SEP 2007
2. **Ni ZH**, Fan HM, Fan XF, Wang HM, Zheng Z, Feng YP, Wu YH, Shen ZX *High temperature Raman spectroscopy studies of carbon nanowalls* **Journal of Raman Spectroscopy** 38: 1449 July 2007
3. **Ni ZH**, Fan HM, Feng YP, Shen ZX, Yang BJ, Wu YH *Raman spectroscopic investigation of carbon nanowalls* **Journal of Chemical Physics** 124 (20): 204703 MAY 2006 {Selected for publication in Virtual Journal of Nanoscale Science & Technology (June 5, 2006).}
4. **Ni ZH**, Liu L, Wang HM, Feng YP, Wu YH, Shen ZX *The electron-hole interactions evolved from graphene to graphite* **Physical Review Letters** (submitted)
5. **Ni ZH**, Wang HM, Ma Y, Kasim J, Wu YH, Shen ZX *Tunable strain and controlled thickness modification in graphene by annealing* **ACS Nano** (Revision)
6. **Ni ZH**, Chen W, Fan XF, Kuo JL, Yu T, Wee ATS, Shen ZX *Raman studies of epitaxial graphene on SiC substrate* **Physical Review B** (Revision)
7. **Ni ZH**, Fan HM, Feng YP, Kasim J, You YM, Shen ZX, Han MY, Li DF *High pressure photoluminescence and Raman studies of ZnxCd1-xSe quantum dots* **Journal of Physics: Condensed Matter** (Submitted)
8. Wang YY, **Ni ZH**, Wang HM, Wu YH, Shen ZX *Interference enhancement of Raman signal of graphene* **Applied Physics Letters** (Accepted)

9. Wang YY, Ni ZH, Yu T, Wang HM, Wu YH, Chen W, Wee ATS, and Shen ZX *Raman studies of monolayer graphene: the substrate effect* **Applied Physics Letters** (Submitted)
10. Wang HM, Wu YH, **Ni ZH**, Shen ZX *Electronic transport and layer engineering in multilayer graphene structures* **Applied Physics Letters** (Accepted)
11. Fan HM, **Ni ZH**, Fan XF, Shen ZX, Feng YP, Zou BS *Orientation dependent Raman spectroscopy of single wurtzite CdS nanowires* **Journal of Physical Chemistry** (Accepted)
12. Fan HM, **Ni ZH**, Feng YP, Fan XF, Kuo JL, Shen ZX, Zou BS *Anisotropy of electron-phonon coupling in single wurtzite CdS nanowires* **Applied Physics Letters** 91: 171911 Oct 2007.
13. Fan HM, **Ni ZH**, Feng YP, Fan XF, Shen ZX, Zou BS *High-pressure Raman and photoluminescence of highly anisotropic CdS nanowires* **Journal of Raman Spectroscopy** 38: 1112 May 2007
14. Fan HM, **Ni ZH**, Feng YP, Fan XF, Kuo JL, Shen ZX, Zou BS *High pressure photoluminescence and Raman investigations of CdSe/ZnS core/shell quantum dots* **Applied Physics Letters** 90(2): 021921 JAN 2007
15. Pan H, **Ni ZH**, Yi JB, Gao XY, Liu CJ, Feng YP, Ding J, Lin JY, Wee ATS, Shen ZX *Optical and magnetic properties of Ni-doped ZnO nanocones* **Journal of Nanoscience and Nanotechnology** 7: 1 March 2007
16. Pan H, **Ni ZH**, Sun H, Yong ZH, Feng YP, Ji W, Shen ZX, Wee ATS, Lin JY *Strong green luminescence of Mg-doped ZnO nanowires* **Journal of Nanoscience and Nanotechnology** 6 (8): 2529 AUG 2006

17. Pan H, Xing GC, **Ni ZH**, Ji W, Feng YP, Tang Z, Chua DHC, Lin JY, Shen ZX *Stimulated emission of CdS nanowires grown by thermal evaporation* **Applied Physics Letters** 91 (19): Art. No. 193105 NOV 5 2007
18. Liu L, Wu RQ, **Ni ZH**, Shen ZX, and Feng YP *Phase transition mechanism in KIO3 single crystals* **Journal of Physics**: Conference Series, 28: 105 June 2006
19. Yang HP, Ma Y, **Ni ZH**, Shen ZX, Feng YP, Yu T *Metal Hydroxide and Metal Oxide Nanostructures from Metal Corrosion* **Journal of Nanoscience and Nanotechnology** (Accepted)
20. Pan H, Zhu YW, **Ni ZH**, Sun H, Poh C, Lim SH, Sow C, Shen ZX, Feng YP, Lin JY *Optical and field emission properties of zinc oxide nanostructures* **Journal of Nanoscience and Nanotechnology** 5 (10): 1683 OCT 2005
21. Chen QJ, Xu S, Long JD, **Ni ZH**, Rider AE, Ostrikov K *High-rate, low-temperature synthesis of composition controlled hydrogenated amorphous silicon carbide films in low-frequency inductively coupled plasmas* **Journal of Physics : D** (Accepted)
22. Du CL, Gu ZB, You YM, Kaism J, Yu T, Shen ZX, **Ni ZH**, Ma Y, Cheng GX, Chen YF *Resonant Raman spectra study for (Mn,Co)-codoped ZnO films* **Journal of Applied Physics** (Accepted)
23. Wang HM, Wu YH, Choong CKS, Zhang J, Teo KL, **Ni ZH**, Shen ZX *Disorder induced bands in first order Raman spectra of carbon nanowalls* **Nanotechnology**, IEEE-NANO 2006. Sixth IEEE Conference on 1: 219 June 2006
24. Wong LH, Wong CC, Liu JP, Sohn DK, Chan L, Hsia LC, Zang H, **Ni ZH**, Shen ZX *Determination of Raman phonon strain shift coefficient of strained silicon*

and strained SiGe **Japanese Journal of Applied Physics** Part 1 44 (11): 7922 NOV 2005

25. You YM, Song H, Fan XF, **Ni ZH**, Yu T, Shen ZX, Cao LZ, Jiang H, Kuo JL *Visualization and investigation of Si-C covalent bonding of Single carbon nanotube grown on silicon substrate* **Journal of American Chemical Society (**Submitted)
26. Fan HM, Fan XF, Wang JX, **Ni ZH**, Feng YP, Zou BS, Shen ZX *Lasing in single CdS nanoribbon with elliptical cross-section microcavity* **Applied Physics Letters** (Submitted)
27. Kasim J, Tee XY, You YM, **Ni ZH**, Setiawan Y, Lee PS, Chan L, Shen ZX *Localized surface plasmons for strain characterization in Raman spectroscopy* **Applied Physics Letters** (Submitted)
28. Chen W, Chen S, Qi DC, Gao XY, Wee ATS, **Ni ZH**, Shen ZX *Band-bending at the Graphene-SiC Interfaces: Effect of the Substrate* **Applied Physics Letters** (Submitted)

Conference publications

1. **Ni ZH**, Fan HM, Feng YP, Kasim J, You YM, Shen ZX, Han MY, Li DF, *High pressure photoluminescence and Raman studies of ZnxCd1-xSe quantum dots* International Conference on Materials for Advanced Technologies (ICMAT) 2005, Singapore

2. **Ni ZH**, Fan HM, Feng YP, Shen ZX, Yang BJ, Wu YH, *Raman studies of carbon nanowalls* International conference of light scattering, Shanghai, 2005, China

3. **Ni ZH**, Fan HM, Feng YP, Shen ZX, Yang BJ, Wu YH, *Raman spectroscopic investigation of carbon nanowalls* Material Research Society (MRS) spring meeting, 2006, San Francisco, USA

4. **Ni ZH**, Fan HM, Feng YP, Kasim J, You YM, Shen ZX, Han MY, Wurtzite to zinc-blende phase transition of ZnCdSe QDs, International Conference on Nanoscience and Technology (ICN+T), 2006, Basel, Switzerland

5. **Ni ZH**, Fan HM, Wang HM, Fan XF, You YM, Wu YH, Feng YP and Shen ZX, Growth mechanism studies of carbon nanowalls by Raman spectroscopy, International Conference on Materials for Advanced Technologies (ICMAT), 2007, Singapore

Chapter 1

Introduction

General introduction

Raman scattering is associated with the light scattering by optical phonons in solids and liquids. Since its discovery, especially after the invention of lasers, Raman scattering has gradually become one of the most versatile spectroscopic tools to characterize the condensed matter systems, including analyzing crystalline disorder, defects, crystallographic axis orientation, chemical composition and the presence of stress, as well as for investigating elementary excitations such as phonons, electrons, polarons, plasmons magnons, etc.[1] In this thesis, Chapter 2 reviews briefly the historical development of the Raman scattering studies, and introduces the basic theory of Raman scattering.

1.1 Introduction to graphene

Graphene is the name of one monolayer thick carbon atoms, which packed into a two-dimensional (2D) honeycomb lattice.[2] It has attracted much interest since it was firstly discovered in 2004.[3,4] Graphene is the basic building block for other carbon nanomaterials, such as 0D fullerenes, 1D carbon nanotubes and 2D nanographite sheets. In the electronic band structure of graphene, the conduction band touches the

valence band at two points (*K* and *K'*)[5,6] in Brillouin zone, and in the vicinity of these points, the electron energy has a linear relationship with the wavevector, $E = \hbar k v_f$. Therefore, electrons in an ideal graphene sheet behave like massless Dirac-Fermions.[7,8] The peculiar properties of graphene make it a promising candidate for fundamental study as well as for potential device applications.[9-15]

Raman spectroscopy is one of the most commonly used tools to characterize carbon nano materials. Raman spectrum is very sensitive to the structure of materials, especially the chemical bonds, and the disordered structure. Besides, it has a high resolution, and can work under many experimental conditions. In Chapter 3 to Chapter 5, Raman and reflection spectroscopies were used as quick and precise methods for determining the thickness of graphene sheets, and also Raman studies of defects and strains in graphene were presented.

1.2 Introduction to carbon nanowalls

Carbon nano materials have received a lot of attention in the past decades. For example, CNTs have unique electronic properties, thermal stability, and high field emission efficiency, and they can be used as scanning probes, sensors, field emitters, electrodes, and so on.[16-18] Recently, two-dimensional (2D) carbon nanowalls (CNWs) have also been fabricated.[19] CNWs comprise flat graphene sheets which is very similar to that in graphite. The thickness of every carbon nanowall sheet is several nm,

but with a length of about several to tens of microns, and they are vertically aligned and well-separated. CNWs may have potential applications in energy storage and field emission displays due to their large surface areas. Besides, CNWs can also be used as template for fabrication of other types of nanostructured materials.[20]

As CNWs have many potential applications, physical characterization of CNWs becomes necessary. The characterization of carbon nano materials mainly focuses on the structure stability, behaviors under different conditions, quantum size effect, and also the disorder analysis. In Chapter 6 to Chapter 7, Raman characterizations of CNWs as well as the study of thermal stability were presented.

1.3 Introduction to semiconductor quantum dots

Ⅱ-Ⅵ wide band-gap semiconductors quantum dots (QDs), such as CdSe and ZnSe, have attracted much attention. Their optical properties make them suitable as visible light emitting diodes (LEDs), lasers, and other optoelectronic devices.[21-22] However, a major problem encountered over the years in fabricating high quality bare QDs is that defects and surface-trap states are usually formed during growth, resulting in low luminescence efficiency and stability. It remains a major challenge to develop new synthetic methods or strategies to produce highly luminescent and stable QDs.

One of the popular methods is to form alloy structured QDs. A composition-tunable emission across most of the visible spectrum can be achieved for alloy QDs, such as $Zn_xCd_{1-x}Se$ alloy QDs. The PL properties of alloy $Zn_xCd_{1-x}Se$ QDs

are comparable to the best reported CdSe-based QDs.[23] Furthermore, these alloy QDs exhibit high stability due to their large particle size, high crystallinity and "hardened" lattice structure.

Instead of fabricating alloy structured QDs, another popular method is to cover the bare QDs with a thin layer (a few angstroms) of another semiconductor or inorganic material which has a similar lattice constant and a larger band-gap. This is the so-called core/shell structured QDs, such as CdSe/ZnS QDs. The core/shell CdSe/ZnS QDs have higher photoluminescence (PL) efficiency and are more robust against chemical degradation or photo-oxidation than the bare CdSe QDs.[24-26]

As both the alloy $Zn_xCd_{1-x}Se$ and core/shell CdSe/ZnS QDs have many potential applications, the physical characterizations of these two QDs are important. Raman and PL spectroscopies are very useful techniques for the characterization of semiconductor QDs.[27] Beside the basic characterization, the stability of semiconductor QDs is not only an essential aspect for understanding their fundamental physical process related to emission and Raman scattering, but is also vital to their applications. One way to explore the structure phase stability of semiconductor QDs is to apply hydrostatic pressure. Under high pressure, the QDs will change from one solid structure to another, which is also called structural phase transition. In Chapters 8 and 9, the high pressure Raman and PL studies of ZnCdSe and CdSe/ZnS QDs were presented.

1.4 Objectives and significance of the studies

My Ph.D project focused on three parts.

The objectives of the first part were:

1. Identification of graphene thickness using reflection and contrast spectroscopy. The contrast between the graphene layers and the SiO_2/Si substrate, which makes the graphene visible, was generated from the reflection spectrum by using normal white light source. The contrast spectra of graphene sheets from one to ten layers and the relation between graphene thickness and contrast values were obtained. Calculations based on the Fresnel's equations were also carried out and the results were compared with the experimental data. This quick and precise method for determining the thickness of graphene sheets is essential for speeding up the research and exploration of graphene.

2. The Raman characterization of graphene. The Raman spectra of single and few-layer graphene were carried out. The Raman modes (D, G′, and G″) of graphene show significant broadening and blue shift as the graphene thicknesses increase. The anisotropy of excitons in graphene was used to explain these phenomena together with double resonance theory. The energy difference between intra- and inter- layer excitons were calculated from the excitation energy dependent Raman results.

3. Raman studies of defects and strains in graphene. The defects were introduced by depositing a thin SiO_2 layer on graphene, and the intensities of defect-induced D and D′ modes were used to estimate the amounts of defects. Besides, compressive

strain was introduced into graphene after annealing process and the frequency shift of in-plane vibrational G mode was used to calculate the magnitude of strain. Moreover, tensile strain in graphene was also realized by depositing a thin layer of silicon. As the strain may affect the physical properties of graphene analogy to what happened in CNTs, our findings should provide useful information critical to graphene device engineering and fabrication.

The objectives of the second part were:

1. Raman spectroscopy characterization of CNWs. This part included (1) Analysis and assignment of different Raman modes of CNWs: both the first order and high order modes. (2) Comparison of the CNWs Raman spectra with those of graphite, CNTs, and other carbon materials to identify their differences in structure and size effect. (3) Orientation and excitation energy dependence of the Raman modes of CNWs.

2. Studies of the temperature dependence of CNWs. In this part, high temperature Raman spectroscopy studies were carried out on CNWs to study their thermal stability. The effects of pure thermal effect and thermal expansion were distinguished. Another aim was to check whether the D mode of CNWs will be eliminated under high temperature, so as to determine if all the defects can be oxidized under high temperature.

The above study should contribute to a better understanding of the structure of

CNWs. This study may contribute to future applications of CNWs.

The objectives of the third part were:

High pressure Raman and PL inversigations of QDs. The pressure coefficients of PL energy and Raman peak frequency of ZnCdSe and CdSe/ZnS QDs were obtained. The transition pressure from wurtzite to rock-salt phase of ZnCdSe and CdSe/ZnS QDs was also compared with that of bulk ZnCdSe and bare CdSe QDs, so that the structural stability of these two QDs can be deduced. Considering the differences between ZnCdSe QDs and bulk ZnCdSe are mainly due to the finite size, the effect of quantum size effect as well as the surface energy on the ZnCdSe alloy was discussed. On the other hand, the differences between CdSe/ZnS QDs and bare CdSe QDs are mainly due to the ZnS shell, the effect of the ZnS shell on the structure of CdSe QDs was also discussed.

This part of study should contribute to a better understanding of the structures of alloy and core/shell QDs; the alloy mechanism as well as the effect of shell on the core QDs can be understood more clearly. Hence, this work should contribute to the synthesis of better quality QDs and their future applications, such as incorporation into solid state structure.

1.5 Organization of this thesis

In chapter 2, Raman scattering is introduced and explained by classical and quantum theory, respectively. The Raman system is also introduced. In Chapter 3 to

Chapter 5, Raman and reflection spectroscopies are used as quick and precise methods for determining the thickness of graphene sheets. The anisotropic of electron hole interactions are estimated. Raman studies of defects and strains in graphene are also presented. In Chapter 6 to Chapter 7, Raman characterizations of CNWs as well as the study of thermal stability are presented. In Chapters 8 and 9, the high pressure Raman and PL studies of ZnCdSe and CdSe/ZnS QDs are carried out. The conclusion and future will be presented in Chapter 10.

1.6 References

[1]. T. Jawhari, Analusis **28**, 15 (2000).
[2]. A. K. Geim, K. S. Novoselov, *Nature Materials* **2007**, *6*, 183.
[3]. K. S. Novoselov, A. K. Geim, S. V. Morozov, D. Jiang, Y. Zhang, S. V. Dubonos, I. V. Grigorieva, A. A. Firsov, *Science* **2004**, *306*, 666.
[4]. K. S. Novoselov, A. K. Geim, S. V. Morozov, D. Jiang, M. I. Katsnelson, I. V. Grigorieva, S. V. Dubonos, A. A. Firsov, *Nature* **2005**, *438*, 197.
[5]. P. R. Wallace, Phys. Rev. **1947**, 71, 622.
[6]. J. C. Slonczewski, P. R. Weiss, Phys. Rev. **1958**, 109, 272.
[7]. G. W. Semenoff, Phys. Rev. Lett. **1984**, 53, 2449.
[8]. F. D. M. Haldane, Phys. Rev. Lett. **1988**, 61, 2015.
[9]. Y. B. Zhang, Y. W. Tan, H. L. Stormer, P. Kim, Nature **2005**, 438, 201.
[10]. K. S. Novoselov, Z. Jiang, Y. Zhang, S. V. Morozov, H. L. Stormer, U. Zeitler, J. C. Maan, G. S. Boebinger, P. Kim, A. K. Geim, Science **2007**, 315, 1379.
[11]. K. S. Novoselov, E. McCann, S.V. Morozov, V. I, Fal'ko, M. I. Katsnelson, U. Zeitler, D. Jiang, F. Schedin, A. K. Geim, Nature Physics, **2006**, 2, 177.
[12]. J. Scott Bunch, Arend M. van der Zande, Scott S. Verbridge, Ian W. Frank, David M. Tanenbaum, Jeevak M. Parpia, Harold G. Craighead, Paul L. McEuen, Science **2007**, 315, 490.
[13]. Hubert B. Heersche, Pablo Jarillo-Herrero, Jeroen B. Oostinga, Lieven M. K. Vandersypen, Alberto F. Morpurgo, Nature **2007**, 446, 56.
[14]. Jannik C. Meyer, A. K. Geim, M. I. Katsnelson, K. S. Novoselov, T. J. Booth, S. Roth, Nature **2007**, 446, 60.
[15]. T. Ohta, A. Bostwick, T. Seyller, K. Horn, E. Rotenberg, Science **2006**, 313, 951.
[16]. E. W. Wong, P. E. Sheehan, C. M. Lieber, Science **1997**, 277, 971.
[17]. M. R. Falvo, G. J. Clary, R. M. Taylor, V. Chi, F. P. BrooksJr, S. Washburn, R. Superfine, Nature **1997**, 389, 582.
[18]. S. S. Fan, M. G. Chapline, N. R. Franklin, T. M. Tombler, A. M. Cassell, H. J. Dai, Science **1999**, 283, 512.
[19]. Y. H. Wu, P. W. Qiao, T. C. Chong, Z. X. Shen, Adv. Mater. **2002**, 14, 64.
[20]. B. J. Yang, Y. H. Wu, B. Y. Zong, Z. X. Shen, Nano Letters **2002**, 2, 751.
[21]. V. I. Klimov, A. A. Mikhailovsky, S. Xu, A. Malko, J. A. Hollingsworth, C. A. Leatherdale, H. J. Eisler, and M. G. Bawendi, Science **2000**, 290, 314.
[22]. S. Coe, W. K. Woo, M. Bawendi, and V. Bulovic, Nature **2000**, 420, 800.
[23]. X. H. Zhong, M. Y. Han, Z. L. Dong, Timothy J White, and W. Knoll, J. Am. Chem. Soc. **2003**, 125, 8589.
[24]. M. Stockman, Nature Mater. **2004**, 3, 423.
[25]. D. Alexander, J. Bruce, C. Zuhlke, B. Koch, R. Rudebusch, J. Deogun and H. Hamza, Optics lett. **2006**, 31, 1957.
[26]. H. Mattoussi, J. M. Mauro, E. R. Goldman, G. P. Anderson, V. C. Sundar, F. V. Mikulec, and M. G. Bawendi, J. Am. Chem. Soc. **2000**, 122, 12142.
[27]. R. W. Meulenberg and G. F. Strouse, Phys. Rev. B **2002**, 66, 035317.

Chapter 2

Introduction to Raman Spectroscopy

2.1 Basic introduction

Raman scattering is one of the processes resulting from the interaction of radiation with matter. It was discovered simultaneously by C. V. Raman and K. S. Krishnan in liquids [1] and by G. S. Landsberg and L. I. Mandelstam in crystals (quartz) [2] in 1928. The effect had been predicted theoretically in 1923 by A. Smekal,[3] and is therefore sometimes also referred to as the Smekal-Raman effect. A characteristic feature of Raman scattering is the change of the scattering light: the frequency of the scattered radiation is different from the frequency of the exciting radiation, and the frequency difference Δv is related to the molecule vibration of the matter.[4]

After the discovery of Raman scattering, it was soon realized this effect can be an excellent tool to study excitations of molecules and molecular structures. In the years following its discovery, Raman spectroscopy was used to provide the first catalog of molecular vibrational frequencies. It was also used to identify chemical compounds because the values of Δv are indicative of different chemical species and also the frequencies of vibrational transitions depend on the atomic masses and the bond strengths.

However, the application of Raman spectroscopy for “real world” analysis was impeded by both fundamental and technical issues, including weak intensity of

Raman, fluorescence interference, and inefficient light collection and detection. In 1960s, with the introduction of lasers, which provide strong, coherent monochromatic light in a wide range of wavelength, and lately the charge-coupled devices (CCD), which permit multiwavenumber detection, together with other development later on, such as laser rejection filters, and personal computers, Raman spectroscopy has become an important analytical technique for the identification of virtually any material. A major improvement of Raman spectroscopy is the emergence of integrated Raman spectrometers that incorporated laser, spectrometer, sample accessories, and software into a complete system. These new instruments were more reliable and simpler to use and help greatly on the widespread application of Raman spectroscopy in different research fields, such as chemistry, biology, and engineering.[5]

2.2 Definition of Raman scattering

When monochromatic radiation of frequency v_0 is incident on a sample, in addition to the reflectance, transmission or/and absorption, some scattering of the radiation occurs. The main part of the scattering has the same frequency as the incident radiation, which is called Rayleigh scattering, after Lord Rayleigh,[6] who explained the essential features of this phenomenon in terms of classical radiation theory in 1871. The Rayleigh scattering arises from scattering centers, like molecules, which are much smaller than the wavelength of the incident radiation. Besides Rayleigh scattering, there is still other scattering which has the same frequency as the

incident radiation. This scattering arises from larger scattering centers like dust particles, and is generally referred to as Mie scattering.[7] Consequently, what is usually referred to, loosely, as Rayleigh scattering consists in practice of true Rayleigh scattering, together with some Mie scattering and unresolved Brillouin scattering, which will be introduced later.

Besides the Rayleigh scattering, the remaining scattering has frequencies different from that of the incident radiation, as it originates from an inelastic scattering process, which is called Raman scattering. The Raman scattering is caused by modulation of susceptibility (or, equivalently, polarizability) of the medium by the vibrations (as well as the scattering by other excitations in solids, including plasmas, excitons, and magnons, occurs by the same mechanism). If some material is irradiated by monochromatic light of frequency ν_0 (laser), then as a result of the electronic polarization induced in the material by this incident beam, the light of frequency ν_0 (Rayleigh scattering) as well as that of frequency $\nu_0 \pm \nu_n$ (Raman scattering) are scattered. The Raman scattering consists of two bands, with one band at lower frequency than the incident radiation ($\nu_0 - \nu_n$) referred to as Stokes band, and another at frequency higher than the incident radiation ($\nu_0 + \nu_n$) referred to as anti-Stokes band. Note that the Raman scattering is very weak compared to the incident radiation, even compared to Rayleigh scattering. The intensity of Rayleigh scattering is generally about 10^{-3} of the intensity of the incident exciting radiation; and the intensity of strong Raman bands is generally about 10^{-3} of the intensity of Rayleigh scattering. [8]

One more scattering needs to mention here is the Brillouin scattering, scattering

with change of frequency originating from a Doppler effect, can also be observed with gases, liquids, and solids. Scattering of this kind was predicted in 1922 by Brillouin,[9] but was not observed until 1930 by Gross.[10] In Brillouin scattering, the change of frequency is very small and of the order of 0.1 cm^{-1}. Brillouin scattering is therefore not separated from the scattered radiation under the experimental conditions used for most studies of Raman scattering. Figure 2.1 shows the schematic of the light scattering.

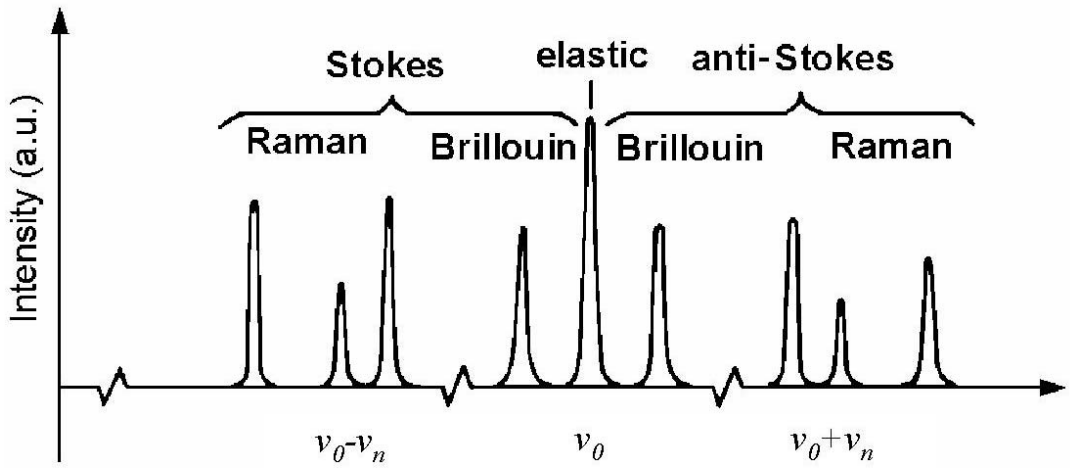

Figure 2.1 Schematic spectrum of light scattering

2.3 Basic theory of Raman scattering

A molecule placed in an electromagnetic field has its charge distribution periodically disturbed by the field. The resultant induced, alternating dipole moment

acts as a source of radiation and gives rise to the entire class of light scattering phenomena.

The alternating dipole moment is generally expressed as the dipole moment per unit volume, the polarization. In the case of interest here, the polarization is proportional to the induced field

$$P_o = \alpha E_o \qquad (1)$$

The constant α, the polarizability, is of central importance in the theory of the Raman effect. Although the description of the detail of the Raman effect requires quantum theory, the existence of the effect is easily predicted from classical electromagnetic theory.

Consider a light of wave of frequency v_0 with an electric field strength E. Since E fluctuates at frequency v_0, we can write

$$E = E_0 \cos 2\pi v_0 t \qquad (2)$$

We then expect a polarization

$$P = \alpha E_0 \cos 2\pi v_0 t \qquad (3)$$

The polarizability, α, consists of two parts. The first is a constant, α_0, which represents the static polarizability. The second is a sum of terms having the periodic time dependence of the normal frequencies of the system under consideration.

$$\alpha = \alpha_0 + \sum \alpha_n \cos 2\pi v_n t \qquad (4)$$

The polarizability may then be written as

$$\begin{aligned} P &= \alpha_0 E_0 \cos 2\pi v_0 t + E_0 \sum \alpha_n \cos 2\pi v_0 t \cos 2\pi v_n t \\ &= \alpha_0 E_0 \cos 2\pi v_0 t + 1/2 E_0 \sum \alpha_n \{\cos 2\pi (v_0 - v_n) t + \cos 2\pi (v_0 + v_n) t\} \end{aligned} \qquad (5)$$

The above equation correctly predicts the major qualitative features of the Raman effect. First, there is a leading term, which represents the component of the polarization having the frequency of the exciting field. This accounts for Rayleigh scattering. Second, each variable component of the polarizability, α_n, give rise to components of the polarization having frequencies ($v_0 + v_n$) and ($v_0 - v_n$), account for the anti-Stokes and Stokes Raman bands.[11]

In actual molecules, both *P* and *E* are vectors consisting of three components in the *x*, *y* and *z* direction. Consequently, *Eq.* (1) is written as

$$\begin{aligned} P_x &= \alpha_{xx}E_x + \alpha_{xy}E_y + \alpha_{xz}E_z \\ P_y &= \alpha_{yx}E_x + \alpha_{yy}E_y + \alpha_{yz}E_z \\ P_z &= \alpha_{zx}E_x + \alpha_{zy}E_y + \alpha_{zz}E_z \end{aligned} \qquad (6)$$

In matrix form, this is written as

$$\begin{pmatrix} P_x \\ P_y \\ P_z \end{pmatrix} = \begin{pmatrix} \alpha_{xx} & \alpha_{xy} & \alpha_{xz} \\ \alpha_{yx} & \alpha_{yy} & \alpha_{yz} \\ \alpha_{zx} & \alpha_{zy} & \alpha_{zz} \end{pmatrix} \begin{pmatrix} E_x \\ E_y \\ E_z \end{pmatrix} \qquad (7)$$

The 3×3 matrix is called as the polarizability tensor. In normal Raman scattering, this tensor is symmetric: $\alpha_{xy} = \alpha_{yx}$, $\alpha_{xz} = \alpha_{zx}$ and $\alpha_{yz} = \alpha_{zy}$.[12] Accordingly, the vibration is Raman-active if one of these components of the polarizability tensor is changed during the vibration, which is known as the Raman selection rules.

Because of the Raman selection rules, not all vibrational transitions will be "Raman active", i.e. some vibrational transitions will not appear in the Raman spectrum. As compared to IR spectroscopy, where a transition can only be observed when that vibration causes a change in dipole moment of the molecule, in Raman only

transition where the polarizability of the molecule changes can be observed. This is due to the fundamental difference in how IR and Raman spectroscopy interact with the vibrational transitions. In Raman spectroscopy, the incoming photon causes a momentary distortion of the electron distribution around a bond in a molecule, followed by reemission of the radiation as the bond returns to its normal state. This causes temporary polarization of the bond, and an induced dipole that disappears upon relaxation. In a molecule with a center of symmetry, a change in dipole is accomplished by loss of the center of symmetry, while a change in polarizability is accomplished by preservation of the center of symmetry. Thus, in a centrosymmetric molecule, asymmetrical stretching and bending will be Raman inactive and IR active, while symmetrical stretching and bending will be Raman active and IR inactive. Hence, in a centrosymmetric molecule, IR and Raman spectroscopy are mutually exclusive. For molecules without a center of symmetry, each vibrational mode may be IR active, Raman active, both, or neither. Symmetrical stretches and bends, however, tend to be Raman active.

2.4 Quantum model of Raman scattering

In quantum theory, Raman scattering is considered as an inelastic collision process in which a quantum of the incident radiation is annihilated or a quantum of the scattered radiation is created with creation (Stokes process) or annihilation (anti-Stokes process) of a phonon. According to quantum theory, radiation is emitted

or absorbed as result of a system making a downward or upward transition between two discrete energy levels and the radiation itself is also quantized.[13]

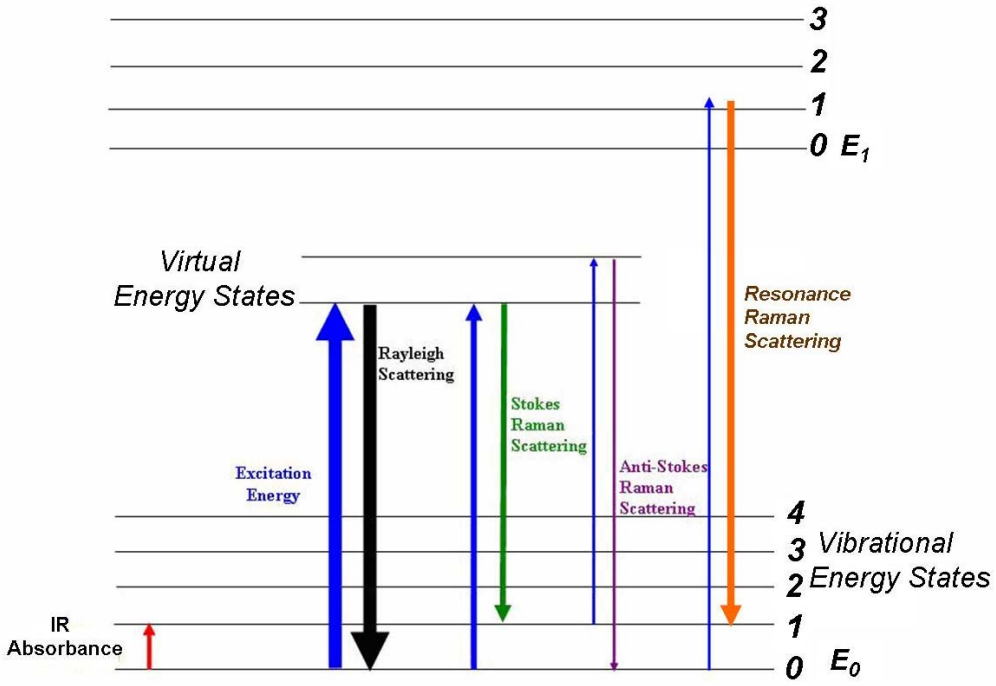

Figure 2.2 Schematic diagram representing Raman scattering process

If the molecule is assumed to be a harmonic oscillator, the vibrational energy is quantized as:

$$E_n = h\nu \cdot (n + \frac{1}{2}) \qquad (8)$$

where ν is the frequency of vibration of the molecule and n is the vibrational quantum number and having integer values of 0, 1, 2, 3,…etc.

If a molecule is placed in an electromagnetic field, a transfer of energy will occur when the following Bohr's frequency condition is satisfied:[12]

$$\Delta E = h\nu \qquad (9)$$

where ΔE is the difference in energy between two quantized states.

Consequently, if the energy difference of an excited state E and ground states E_0 satisfies:

$$\Delta E = E - E_0 \qquad (10)$$

The molecule can "absorb" or "emits" ΔE when it is excited from E_0 to E or revert from E to E_0.

Figure 2.2 shows the schematic diagram of the quantum theory description of Raman scattering. The virtual states[14] are usually intermediate states between the ground and first excited state of the system. In Raman scattering process, the system is excited by absorbing a photon and goes back by emitting a photon. The Rayleigh scattering arises from transitions which start and end at the same vibrational energy level. Stokes Raman scattering arises from transitions which start at the ground energy state and finish at a higher energy level, whereas anti-Stokes Raman scattering involves a transition from a higher to a lower level. The Raman frequency shift corresponds to the energy difference between the vibrational levels, also known as phonon energy. Thus, Raman frequency shift is an inherent characteristic of the material and is independent of the incident radiation. Normally, the anti-Stokes lines are less intense than the corresponding Stokes lines. This is because anti-Stokes lines arise from the excited states and Stokes lines arise from the ground state, while few molecules are initially in excited vibrational states compared to that in the ground state.

2.5 Resonance Raman scattering

As has been mentioned above, Raman scattering is generally very weak, it is only about 10^{-6} of the incident radiation. However, in certain conditions, the normally weak Raman signal can be greatly enhanced. If the wavelength of the incident laser radiation is close to that of an electronic absorption band, the Raman scattering may be enhanced by several orders of magnitude, typically in the range 10^3 to 10^6, which is known as resonance Raman scattering (RRS). The RRS can also be understood by looking at Figure 3.1, in which the excitation line energy is close to any of the energy level of the excited state E_1. In that case, rather than exciting the molecule to a virtual energy state, it is excited to near one of the excited electronic transition states. The main advantage of RRS over traditional Raman spectroscopy is the large increase in intensity of the peaks, which makes sample with very low concentration or very weak signal can be observable under Raman spectroscopy. The RRS is also widely used in the application of nanostructured materials, like nanowires, nanotubes or quantum dots, in which the strong resonance enhance the Raman signals of those nanosize materials.

2.6 Micro Raman systems

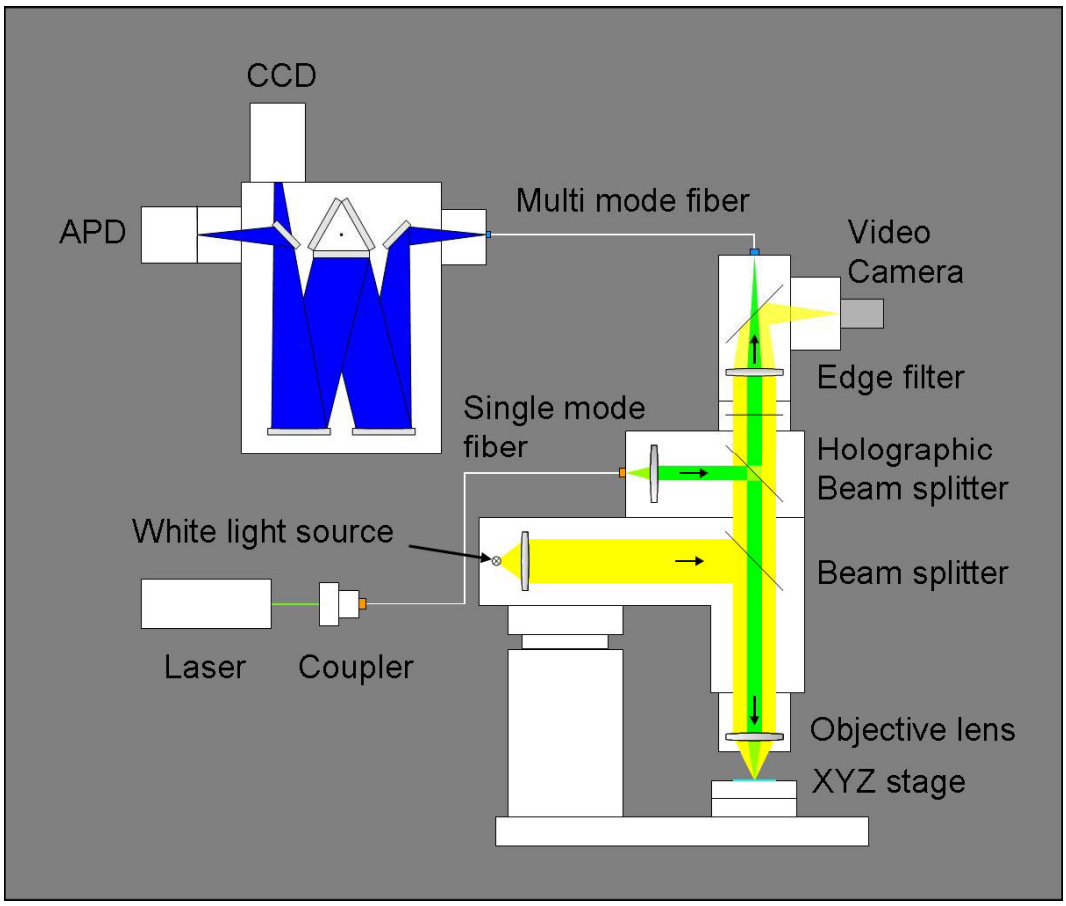

Figure 2.3 Schematic diagram of Raman system

Three micro Raman systems were used in our experiments: WITEC CRM200 (532 nm, DPSSL laser), JY-T64000 (488 and 514 nm, Ar+ laser), and Renishaw inVia (325nm, He-Ne laser) Raman systems. Figure 2.3 shows the schematic diagram of the WITEC CRM200 system. A normal white light source (tungsten halogen lamp, excitation range from 350 nm to 850 nm) is used to illuminate and focus the sample. The reflected white light is collected and the optical image is recorded with a video camera. A 532 nm laser is coupled into a single mode fiber and then directed to the

sample through an objective lens to excite the Raman signals. The laser spot size at focus point is around 500 nm with a ×100 (NA=0.95) objective lens. To avoid laser induced sample heating, the power of laser at sample is below 1 mW. The sample is put on a translation stage which can be moved coarsely along *x*- and *y-axes*. It also can be finely moved with a piezostage. The piezostage has 100 μm of travel distance along *x*- and *y*-directions and 20 μm in the *z*-direction, which is appropriate as a mapping stage. The Raman scattering light as well as the Rayleigh light are collected in backscattering mode. An edge filter is used to block the Rayleigh light and only the Raman and a very small fraction of Rayleigh signals go to the 1800/600/150 grooves/mm grating and detected using a TE-cooled charge-coupled-device (CCD) or avalanche photodiode (APD). During the Raman image, the sample is scanned under the illumination of laser. The Raman spectra from every spot of the sample are recorded and Raman images using peak intensity, peak position, or peak width can be generated after data analysis. The stage movement and data acquisition were controlled using ScanCtrl Spectroscopy Plus software from WITec GmbH, Germany. Data analysis was done using WITec Project software.

2.7 References

[1]. C. V. Raman, K. S. Krishnan, *Nature* **1928,** 121, 501.
[2]. G. Landsberg, L. Mandelstam, *Naturwiss* **1928,** 16, 557.
[3]. A. Smekal, *Naturwiss* **1923,** 11, 873.
[4]. M. M. Sushchinskii, *Raman spectra of molecules and crystals* **1972**, John Wiley & Sons.
[5]. R. L. McCreery, *Raman spectroscopy for chemical analysis* **2000**, Wiley interscience (New York).
[6]. L. Rayleigh, *Phil. Mag.* **1871,** 274, 447.
[7]. G. Mie, *Ann. Physik* **1908,** 25, 377.
[8]. D. A. Long, *Raman spectroscopy* **1977**, McGraw Hill.
[9]. L. Brillouin, *Ann. Phys. (Paris)* **1922,** 88, 17.
[10]. E. *Z.* Gross, *Physik* **1930,** 63, 685.
[11]. M. C. Tobin, *Laser Raman spectroscopy* **1971**, Wiley.
[12]. K. Nakamoto, *Infrared and Raman Spectra of Inorganic and Coordination Compounds*. **1997**, John Wiley & Sons, Inc., New York.
[13] L. Liu, Raman Scattering and First-Principles Analysis of Ge Nanostructures, h-BN and KIO_3, Thesis (Ph.D.)--Dept. of Physics, Faculty of Science, National University of Singapore, 2003.
[14]. M. Born and K. Huang, *Dynamical Theory of Crystal Lattices* **1954**, Clarendon Press, Oxford.

Chapter 3

Graphene Thickness Determination Using Reflection and Contrast Spectroscopy

3.1 Introduction

The recent success in extracting few layers graphite sheet, even monolayer graphene from highly ordered pyrolytic graphite (HOPG) using a technique called micromechanical cleavage[1,2] has stimulated great interest in both the fundamental physics study and potential applications of graphene.[3] Graphene has a two-dimensional (2D) crystal structure, which is the basic building block for other sp^2 carbon nanomaterials, such as nanographite sheets, and carbon nanotubes. The peculiar properties of graphene arise from its unique electronic band structure, in which the conduction band touches the valence band at two points (K and K')[4,5] in Brillouin zone, and in the vicinity of these points, the electron energy has a linear relationship with the wavevector, $E = \hbar k v_f$. Therefore, electrons in an ideal graphene sheet behave like massless Dirac-Fermions.[6,7] Some of these unique properties have been observed experimentally[8-21] and many new ideas[22-29] about the fundamental physics and device applications of single and few layer graphene have been proposed. As presently micromechanical cleavage is still the most effective way to produce high-quality graphene sheets, a quick and precise method for determining the thickness of graphene sheets is essential for speeding up the research and exploration

of graphene. Although atomic force microscopy (AFM) measurement is the most direct way to identify the number of layers of graphene, the method has a very slow throughput and may also cause damages to the crystal lattice during the measurement. Furthermore, an instrumental offset of ~0.5 nm (caused by different interaction force) always exists, which is even larger than the thickness of a monolayer graphene and a data fitting is required to extract the true thickness of graphene sheets.[30] Unconventional Quantum Hall effects[8-10] are often used to differentiate monolayer and bilayer graphene from few-layers. However, it is not a practical and efficient way. Researchers have attempted to develop more efficient ways to identify different layers of graphene without destroying the crystal lattice. Raman spectroscopy is the potential candidate for non-destructive and quick inspection of thickness of graphene.[30-32] Unfortunately, the differences between two and few layers of graphene sheets are not obvious and unambiguous in the Raman spectra. Another possible way is to identify the graphene layers of different thickness with the "naked eyes" under optical microscope. However, this is not a quantitative method because the color/contrast often varies from one laboratory to another.[1,9]

In this chapter, we report a direct method for efficient and accurate inspection of the graphene sheet using contrast spectrum. The contrast between the graphene layers and the SiO_2/Si substrate, which makes the graphene visible, was generated from the reflection spectrum by using normal white light source. Clear contrast difference for graphene sheets from one to ten layers can be observed. Calculations based on the Fresnel's equations have been carried out and the results show excellent agreement

with the experimental data. The contrast image provides good evidence that this new method is an efficient and unambiguous way to identify the number of graphene layers.

3.2 Experimental

The graphene samples were prepared by micromechanical cleavage and transferred to Si wafer with a 285 nm SiO_2 capping layer.[1] The optical microscope was used to locate the few layers graphene and the thickness was further confirmed by Raman spectra/image. In the reflection experiments, the incident light was emitted from a normal white light source (tungsten halogen lamp, excitation range from 350 to 850 nm, through a 1 mm aperture). The reflected light was collected using backscattering configuration (with a 100 um pinhole) and directed to a 150 lines/mm grating and detected with a TE-cooled charge-coupled-device (CCD). The obtained reflection spectra were compared with that of background spectrum from SiO_2/Si to generate the contrast spectra. The Raman spectra were carried out with a WITEC CRM200 Raman system. The excitation source is 532 nm laser (2.33 eV) with a laser power below 0.1 mW on the sample to avoid laser induced heating. A 100× objective lens with a NA=0.95 was used both in the Raman and reflection experiments, and the spot sizes of 532 nm laser and white light were estimated to be 500 nm and 1 um, respectively, which we determined by using a scanning edge method.[33] For the contrast and Raman image, the sample was placed on an *x-y*

piezostage and scanned under the illumination of laser and white light. The Raman and reflection spectra from every spot of the sample were recorded.

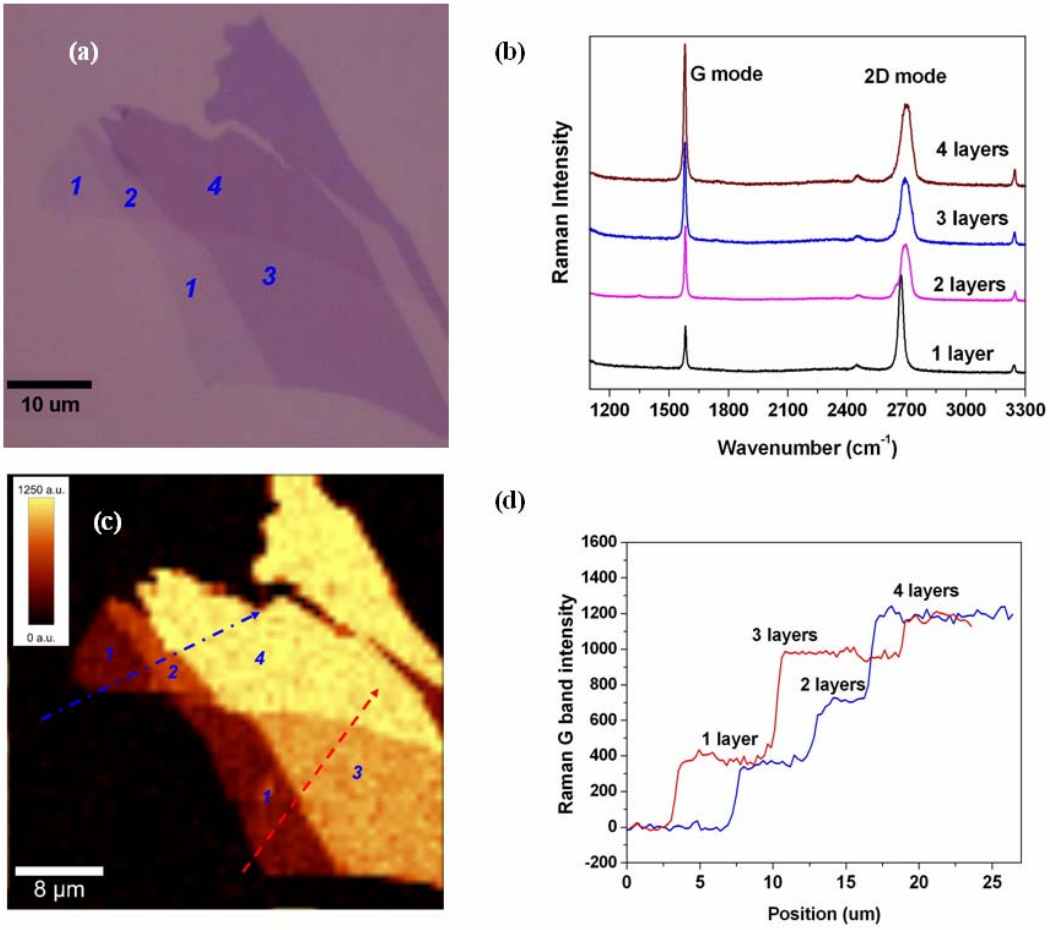

Figure 3.1 (a) optical image of graphene with 1, 2, 3 and 4 layers. (b) Raman spectra as a function of number of layers. (c) Raman image plotted by the intensity of G band. (d) The cross section of Raman image, which corresponds to the dash lines.

3.3 Results and Discussion

Figure 3.1a shows the optical image of a graphene sample on the SiO_2/Si substrate. The graphene sheet shows four different contrast regions, which can be understood as having four different thicknesses. The Raman spectra were then taken from different regions of the sample and the results are shown in Figure 3.1b. As has been proposed by Ferrari et al., the second order Raman 2D band is sensitive to the number of layers of graphene[31,32] and the 2D band of single layer graphene is very sharp and symmetric compared to that of bilayer and few-layer graphemes.[34] In our Raman spectra, the sharp 2D band of the single layer graphene can be clearly observed and distinguished. However, the difference of 2D band is not obvious for two to four layers. A clear difference between those layers is that G band intensity shows an increase with the number of layers (the spectra are recorded under the same condition). Once the single layer graphene is identified by the 2D band of Raman scattering, we can further identify different layers of graphene from the G band intensity plot, as shown in Figure 3.1c. This can be done as the intensity of G band almost linearly increases with the number of layers for few-layer graphene.[32] Figure 3.1d plots the Raman intensity of the G band along two dash lines drawn in Figure 3.1c. It is obvious that the graphene sheet contains one, two, three and four layers. These can be compared with the contrast spectrum/image discussed later.

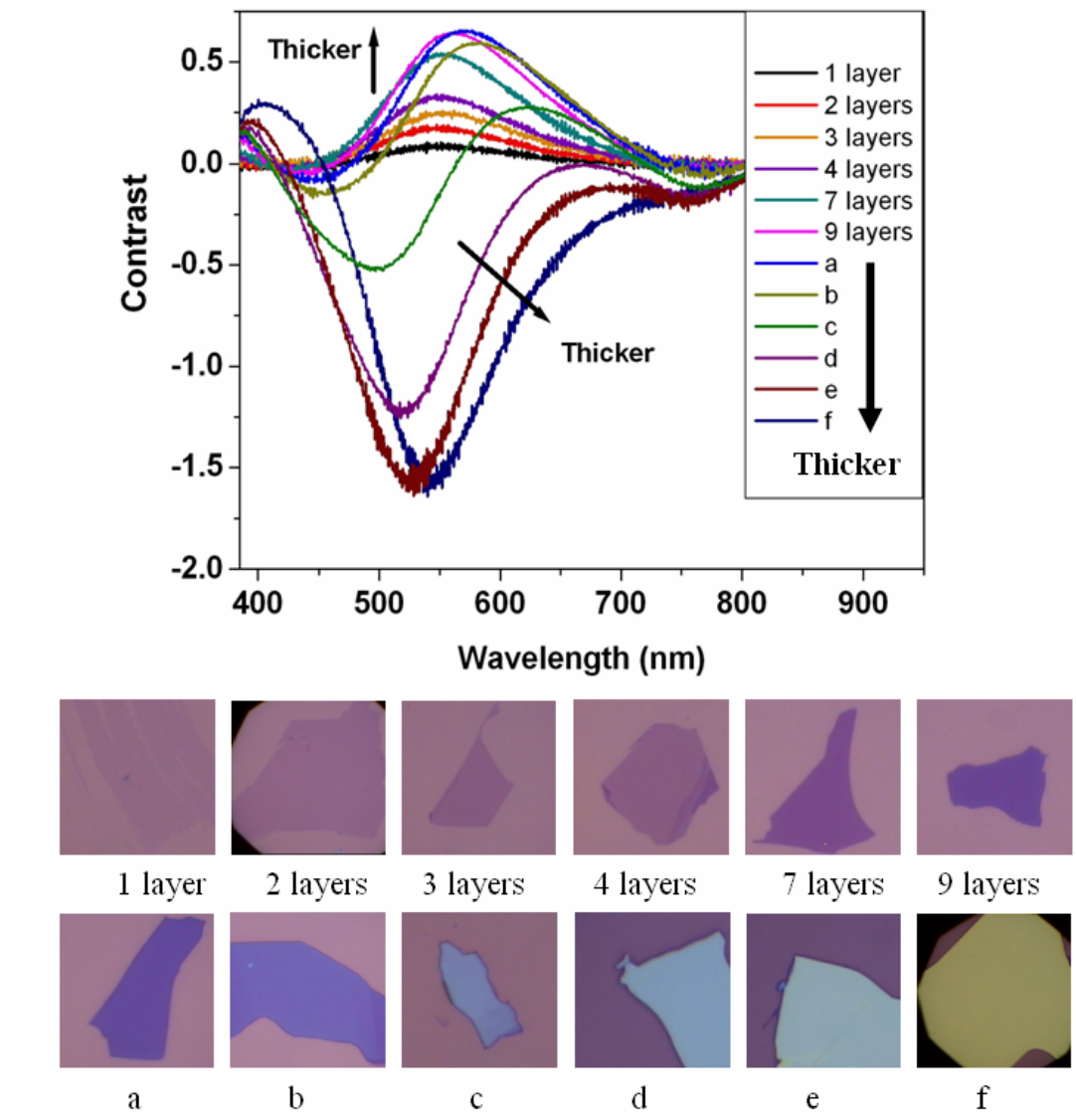

Figure 3.2 The contrast spectra of graphene sheets with different thicknesses, together with the optical images of all the samples. Besides the samples with 1, 2, 3, 4, 7 and 9 layers, samples a, b, c, d, e and f are more than ten layers and the thickness increases from a to f. The arrows in the graph show the trend of curves in terms of the thicknesses of graphene sheets.

Figure 3.2 shows the contrast spectra for different thicknesses of graphene sheets, together with the optical images of all the samples used. Besides the samples with 1, 2, 3, 4, 7 and 9 layers, samples a, b, c, d, e and f are more than ten layers thick and the thickness increases from a to f. The contrast spectra are obtained by the following calculation $C(\lambda)= (R_0(\lambda)- R(\lambda))/ R_0(\lambda)$, where $R_0(\lambda)$ is the reflection spectrum from the SiO_2/Si substrate and $R(\lambda)$ is the reflection spectrum from graphene sheet. Using this method, the contrast across the whole visible range (with a spectrum resolution higher than 1 nm) can be recorded continually and no bandpass filter which was used in reference 35 is needed. Although one can observe different colors/contrasts for graphene sheets of different thickness using the optical image with "naked eyes", the graphene's visibility strongly varies from one laboratory to another and it relies on experience of the observer. Contrast spectra can make it quantitative and accurate. The contrast spectrum for single layer graphene has a peak centered at 550 nm, which is in green-orange range and it makes the single layer graphene visible. The contrast peak position is almost unchanged (550 nm) with increasing number of layers up to ten. The contrast for single layer graphene is about 0.09 ± 0.005 and it increases with the number of layers, for example, 0.175 ± 0.005, 0.255 ± 0.010, 0.330 ± 0.015 for two, three, and four layers, respectively. For graphene of around ten layers in thickness, the contrast of the sample saturates and the contrast peak shifts towards higher wavelength (samples a and b). For samples with larger number of layers (c to f), negative contrast occurs. This can easily be understood that these samples are so thick

that the reflections from their surface become more intense than that from the SiO_2/Si substrate, resulting in negative value contrast.

The origin of the contrast can be explained by the Fresnel's equations. Consider the incident light from air (n_0=1) onto a graphene, SiO_2, and Si tri-layer system. The reflected light intensity from the tri-layer system can then be described by:[35,36]

$$R(\lambda) = r(\lambda)r^*(\lambda) \quad (1)$$

$$r(\lambda) = \frac{r_a}{r_b} \quad (2)$$

$$r_a = (r_1 e^{i(\beta_1+\beta_2)} + r_2 e^{-i(\beta_1-\beta_2)} + r_3 e^{-i(\beta_1+\beta_2)} + r_1 r_2 r_3 e^{i(\beta_1-\beta_2)}) \quad (3)$$

$$r_b = (e^{i(\beta_1+\beta_2)} + r_1 r_2 e^{-i(\beta_1-\beta_2)} + r_1 r_3 e^{-i(\beta_1+\beta_2)} + r_2 r_3 e^{i(\beta_1-\beta_2)}) \quad (4)$$

where $r_1 = \frac{n_0 - n_1}{n_0 + n_1}, r_2 = \frac{n_1 - n_2}{n_1 + n_2}, r_3 = \frac{n_2 - n_3}{n_2 + n_3}$ are the reflection coefficients for different interfaces and $\beta_1 = 2\pi n_1 \frac{d_1}{\lambda}, \beta_2 = 2\pi n_2 \frac{d_2}{\lambda}$ are the phase difference when the light passes through the media which is determined by the path difference of two neighboring interfering light beams. In the above equations, n_0, n_1, n_2, n_3 are the refractive indexes of air, graphene, SiO_2, and Si, while d_1, d_2 are the thickness of graphene and SiO_2. The thickness of the graphene sheet can be estimated as $d_1 = N\Delta d$, where N represents the number of layers and Δd is the thickness of single layer graphene (Δd=0.335 nm).[37,38] The refractive index of graphene (n_1) may differ from that of bulk graphite (n_G=2.6-1.3i),[35] which can be used as a fitting parameter. The thickness of SiO_2, d_2, is 285 nm, with a maximum 5% error. The refractive index of SiO_2, n_2, is wavelength dependent, which was taken from reference.[39] The Si substrate can be considered semi-infinite and the refractive index of Si, n_3, is also wavelength

dependent.[39] The reflection from SiO_2 background, $R_0(\lambda)$, was calculated by using a d_1=0.

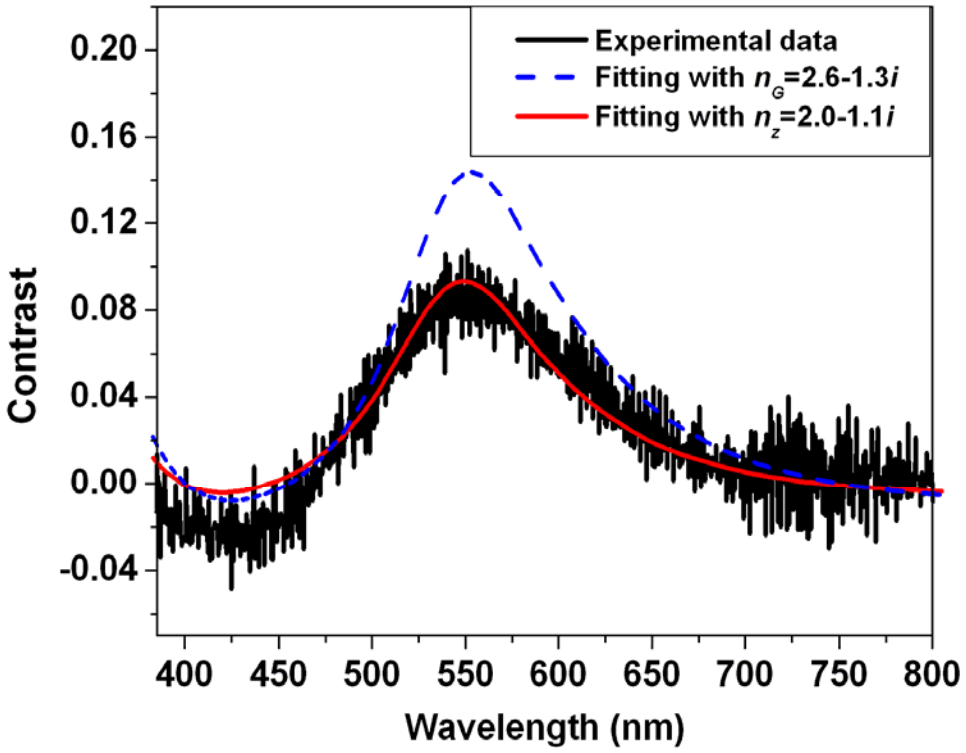

Figure 3.3 The contrast spectrum of single layer graphene: experimental data (black line), the simulation result using n=2.0-1.1i (red line), and the simulation result using n_G=2.6-1.3i (dash line).

The calculated contrast spectra of single layer graphene are shown in Figure 3.3. The optimized simulation result was obtained with refractive index of single layer graphene n_z=2.0-1.1i, whereas the simulation result using the bulk graphite value of n_G (2.6-1.3i) shows large deviation from our experimental data. The variation of the refractive index of graphene from that of graphite may be ascribed to the decrease of interlayer interaction when the sample is ultra thin. Using the optimized refractive index n_z, we calculated the contrast spectra of two to ten layers and a significant improvement of agreement between the fitting results and the experimental data was readily achieved as shown in Figure 3.4. The deviation between the experimental results and simulation is only 2%. By using this technique, the thickness of unknown graphene sheet can be determined directly by comparing the contrast value with the standard values shown in Figure 3.4. Alternatively, it can be obtained using the following equation:

$$C=0.0046+0.0925N-0.00255N^2 \qquad (5)$$

where N ($\leqslant$10) is the number of layers of graphene sheet.

Our technique does not need a single layer graphene as reference (as in Raman), and it does not have an instrument offset problem caused by different interaction forces between probe and medium (as in AFM).[30] Moreover, the simulation shows that the highest contrast of graphene sheet is almost unchanged for the thickness of

SiO_2 substrate between 280 to 320 nm. Thus, our results can be applied directly to 300 nm SiO_2 capping layer, which is also commonly used. With simple modification, our technique can also be used to identify the number of graphene layers on 90 nm SiO_2 substrate, which was suggested by Blake et al.[35] that this substrate may provide better contrast.

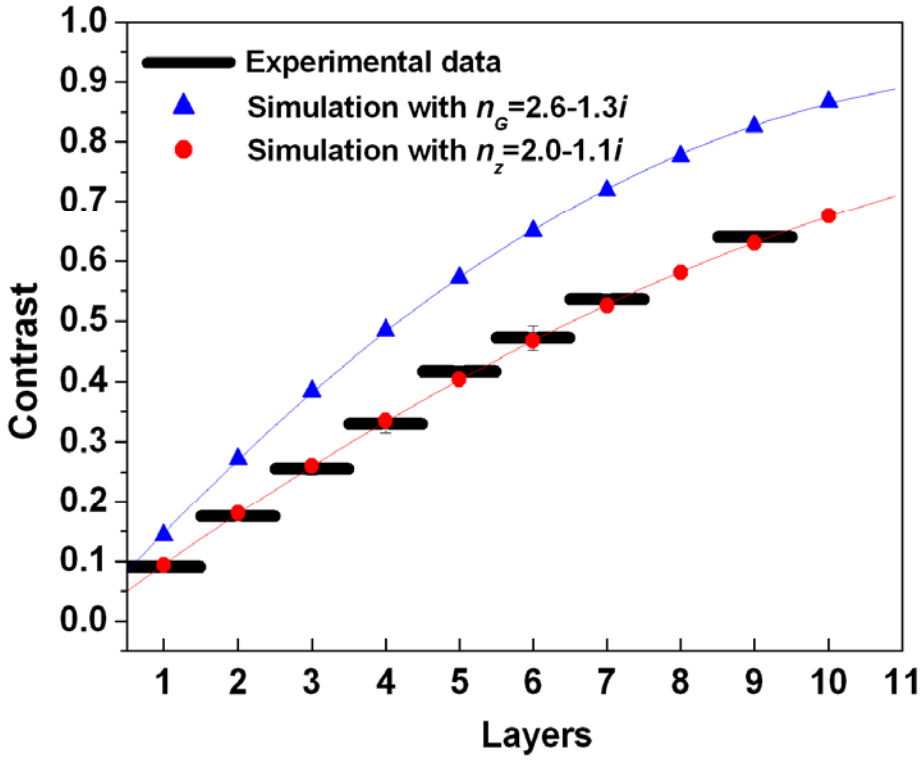

Figure 3.4 The contrast simulated by using both n_G (blue triangles) and n_z (red circles), the fitting curve for the simulations (blue and red lines), and our experiment data (black thick lines), respectively, for one to ten layers of graphene.

In order to demonstrate the effectiveness of the contrast spectra in graphene thickness determination, we carried out the contrast imaging, which was performed by scanning the sample under white light illumination, with an *x*-*y* piezostage and recording the reflection spectrum from every spot of the sample. As shown in Figure 3.5a, distinct contrast for different thicknesses of graphene can be observed from the image. It is worth noting that the contrast image measurement can be done in a few minutes. Figures 3.5b and 3.5c show contrast along the two dash lines on the image. The contrast value for each thickness agrees well with those shown in Figure 3.4. Using equation 5, the N values along the two dash lines are calculated, where the N along the blue line is: 0.99, 1.93, and 3.83; and along the red line is: 0.98, 2.89 and 3.94. Again our results show excellent agreement. The 3D contrast image is shown in Figure 3.5d which gives a better perspective view of the sample.

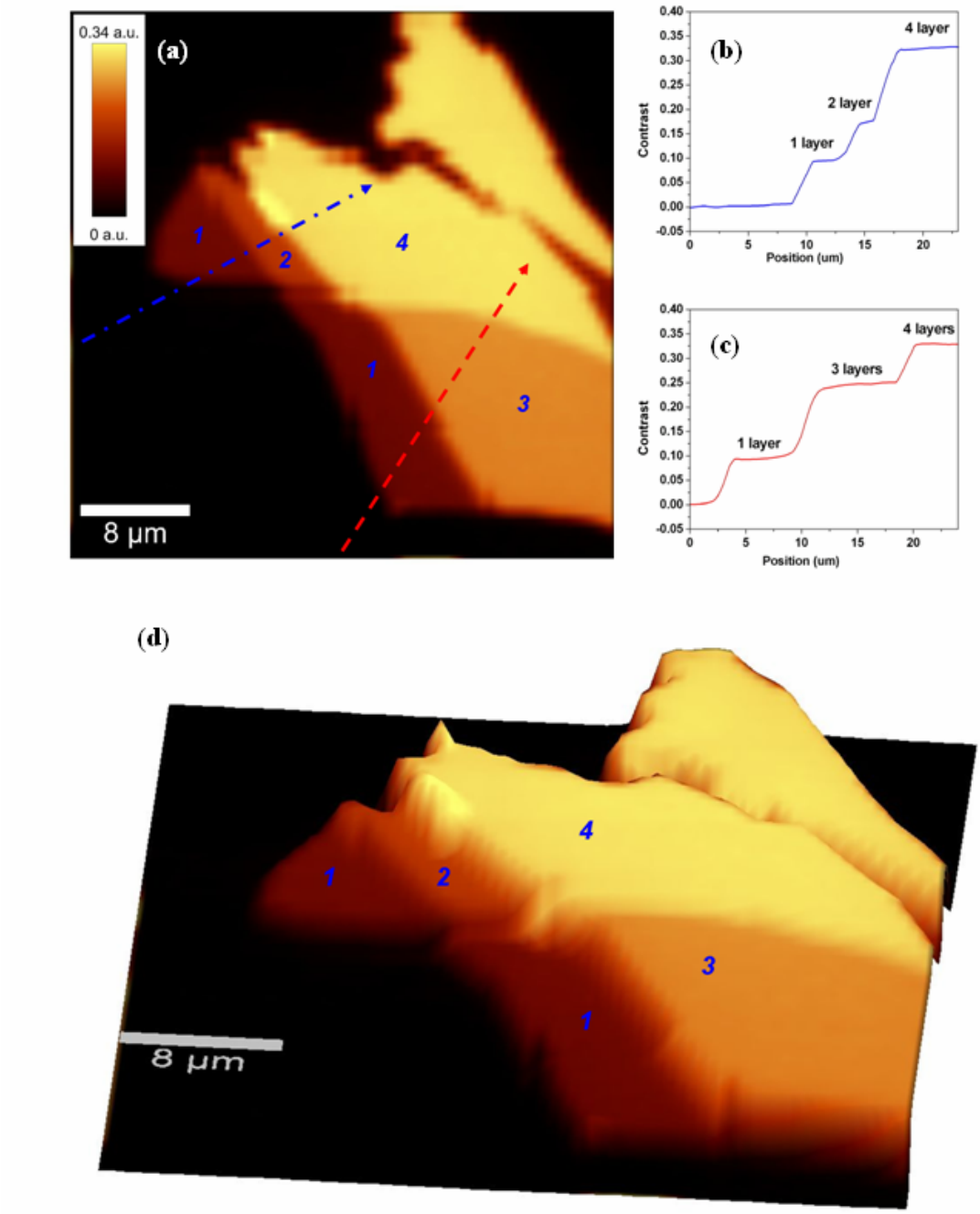

Figure 3.5 (a) The contrast image of the sample. (b) and (c): The cross section of contrast image, which corresponds to the dash lines. The contrast values of each thickness agree well with the contrast values of one to four layers as shown in Figure 4. (d) The 3D contrast image, which shows a better perspective view of the sample.

3.4 Conclusion

In summary, we have demonstrated that by using contrast spectra, we can easily determine the number of graphene layers. We have also calculated the contrast using the Fresnel's equations and the results show an excellent match with the experimental data. From the simulation, we extracted the refractive index of graphene below ten layers as n_z=2.0-1.1i, which is different from that of bulk graphite. Our experimental values can be directly used as a standard to identify the thickness of graphene sheet on Si substrate with ~300 nm SiO_2 capping layer. We have also given an analytical expression for determining number of layers. From the contrast image, we have demonstrated the effectiveness of this new technique. Although current research mainly focuses on the single and bilayer graphene, we believe that the few layers (less than 10 layers) graphene also have interesting properties as they still exhibit the two-dimensional properties.[3] Reflection and contrast spectroscopy provides a fast, non-destructive, easy-to-use, and accurate method to identify the numbers of graphene layers (below 10 layers), which helps future research and application of graphene.

3.5 References

[1]. K. S. Novoselov, A. K. Geim, S. V. Morozov, D. Jiang, Y. Zhang, S. V. Dubonos, I. V. Grigorieva, A. A. Firsov, Science **2004**, 306, 666.

[2]. K. S. Novoselov, D. Jiang, F. Schedin, T. J. Booth, V. V. Khotkevich, S. V. Morozov, A. K. Geim, PNAS **2005**, 102, 10451.

[3]. A. K. Geim, K. S. Novoselov, Nature Materials **2007**, 6, 183.

[4]. P. R. Wallace, Phys. Rev. **1947**, 71, 622.

[5]. J. C. Slonczewski, P. R. Weiss, Phys. Rev. **1958**, 109, 272.

[6]. G. W. Semenoff, Phys. Rev. Lett. **1984**, 53, 2449.

[7]. F. D. M. Haldane, Phys. Rev. Lett. **1988**, 61, 2015.

[8]. K. S. Novoselov, A. K. Geim, S. V. Morozov, D. Jiang, M. I. Katsnelson, I. V. Grigorieva, S. V. Dubonos, A. A. Firsov, Nature **2005**, 438, 197.

[9]. Y. B. Zhang, Y. W. Tan, H. L. Stormer, P. Kim, Nature **2005**, 438, 201.

[10]. K. S. Novoselov, Z. Jiang, Y. Zhang, S. V. Morozov, H. L. Stormer, U. Zeitler, J. C. Maan, G. S. Boebinger, P. Kim, A. K. Geim, Science **2007**, 315, 1379.

[11]. K. S. Novoselov, E. McCann, S. V. Morozov, V. I. Fal'ko, M. I. Katsnelson, U. Zeitler, D. Jiang, F. Schedin, A. K. Geim, Nature Physics, **2006**, 2, 177.

[12]. J. Scott Bunch, Arend M. van der Zande, Scott S. Verbridge, Ian W. Frank, David M. Tanenbaum, Jeevak M. Parpia, Harold G. Craighead, Paul L. McEuen, Science **2007**, 315, 490.

[13]. Hubert B. Heersche, Pablo Jarillo-Herrero, Jeroen B. Oostinga, Lieven M. K. Vandersypen, Alberto F. Morpurgo, Nature **2007**, 446, 56.

[14]. Jannik C. Meyer, A. K. Geim, M. I. Katsnelson, K. S. Novoselov, T. J. Booth, S. Roth, Nature **2007**, 446, 60.

[15]. T. Ohta, A. Bostwick, T. Seyller, K. Horn, E. Rotenberg, Science **2006**, 313, 951.

[16]. A. Bostwick, T. Ohta, T. Seyller, K. Horn, E. Rotenberg, Nature Physics **2007**, 3, 36.

[17]. E. W. Hill, A. K. Geim, K. S. Novoselov, F. Schedin, P. Blake, IEEE Trans. Magn. **2006**, 42, 2694.

[18]. Z. H. Chen, Y. M. Lin, Michael J. Rooks, P. Avouris, Preprint at http://arxiv.org/abs/cond-mat/0701599 (**2007**).

[19]. M. Y. Han, B. Oezyilmaz, Y. B. Zhang, P. Kim, Preprint at http://arxiv.org/abs/cond-mat/0702511 (**2007**).

[20]. C. Berger, Z. M. Song, X. B. Li, X. S. Wu, N. Brown, C. Naud, D. Mayou, T. B. Li, J. Hass, Alexei N. Marchenkov, Edward H. Conrad, Phillip N. First, Walt A. de Heer, Science **2006**, 312, 1191.

[21]. E. V.; Castro, K. S. Novoselov, S. V. Morozov, N. M. R. Peres, J. M. B. Lopes dos Nilsson, J. Santos, F. Guinea, A. K. Geim, A. H. Castro Neto, Preprint at http://arxiv.org/abs/cond-mat /0611342 (**2006**).

[22]. N. M. R. Peres, F. Guinea, A. H. Castro Neto, Phys. Rev. B **2006**, 73, 125411.

[23]. J. Nilsson, A. H. Castro Neto, F. Guinea, N. M. R. Peres, Preprint at http://arxiv.org/abs/cond-mat/0604106 (**2006**).
[24]. M. Titov, C. W. J. Beenakker, Phys. Rev. B **2006**, 74, 041401.
[25]. Y. W. Son, M. L. Cohen, S. G. Louie, Nature **2006**, 444, 347.
[26]. M. I. Katsnelson, K. S. Novoselov, A. K. Geim, Nature Physics **2006**, 2, 620.
[27]. V. V. Cheianov, V. Fal'ko, B. L. Altshuler, Science, **2007**, 315, 1252.
[28]. A. Rycerz, J. Tworzyd ł o, C. W. J. Beenakker, Nature Physics **2007**, 3, 172.
[29]. B. Trauzettel, Denis V. Bulaev, D. Loss, G. Burkard, Nature Physics **2007**, 3, 192.
[30]. A. Gupta, G. Chen, P. Joshi, S. Tadigadapa, P. C. Eklund, Nano Lett. **2006**, 6, 2667.
[31]. A. C. Ferrari, J. C. Meyer, V. Scardaci, C. Casiraghi, M. Lazzeri, F. Mauri, S. Piscanec, D. Jiang, K. S. Novoselov, S. Roth, A. K. Geim, Phys. Rev. Lett. **2006**, 97, 187401.
[32]. D. Graf, F. Molitor, K. Ensslin, C. Stampfer, A. Jungen, C. Hierold, L. Wirtz, Nano Lett., **2007**, 7, 238.
[33]. G. Veshapidze, M. L. Trachy, M. H. Shah, B. D. DePaola, Applied Optics **2006**, 45, 8197.
[34]. C. Thomsen, S. Reich, Phys. Rev. Lett. **2000**, 85, 5214.
[35]. P. Blake, K. S. Novoselov, A. H. Castro Neto, D. Jiang, R. Yang, T. J. Booth, A. K. Geim, E. W. Hill, Preprint at http://arxiv.org/abs/ cond-mat /0705.0259 (**2007**).
[36]. H. Anders, Thin Films in Optics; Focal Press: London, **1967**.
[37]. B. T. Kelly, Physics of Graphite; Applied Science: London, **1981**.
[38]. M. S. Dresselhaus, G. Dresselhaus, P. C. Eklund, Science of Fullerenes and Carbon Nanotubes; Academic Press: San Diego, CA, **1996**; p 965.
[39]. E. D. Palik, Handbook of Optical Constants of Solids; Academic Press: New York, **1991**.

Chapter 4

Anisotropy of Electron-hole Pair States in Graphene Layers Observed by Raman Spectroscopy

4.1 Introduction

Graphene has exhibited a series of new electronic properties such as anomalously quantized Hall effects, absence of weak localization and the existence of a minimum conductivity[1,2,3]. These properties can be ascribed to its unique band structure whose conical valence and conduction bands meet at the single point of Dirac crossing energy(E_D)[4,5]. As a result of that, quasiparticles in graphene behave as massless Dirac fermions and follow the rules of 2+1 dimensional quantum electrodynamics. As confined within the highly anisotropic layer lattice, electrons and holes, the two elementary quasiparticles of graphene, would undergo stronger interaction. Theoretically, the binding energy of 2D confined excitons would be four times larger relative to that of 3D cases[6]. Obviously, such effect will modify the dynamics of electrons and holes in graphene and affect its optical and transport properties too. For example, recently, Bostwick *et al.* found that the electron-hole (e-h) coupling may be responsible partially to the kink feature near E_D of the graphene band structure from angle-resolved photoemission spectroscopy (ARPES) observations.[7] Here, we would present our resonant Raman study on the e-h interaction behavior of graphene layers. From the dependence of the resonant Raman peak position on the layer number, the

2D confinement effect on the e-h interaction is demonstrated and measured.

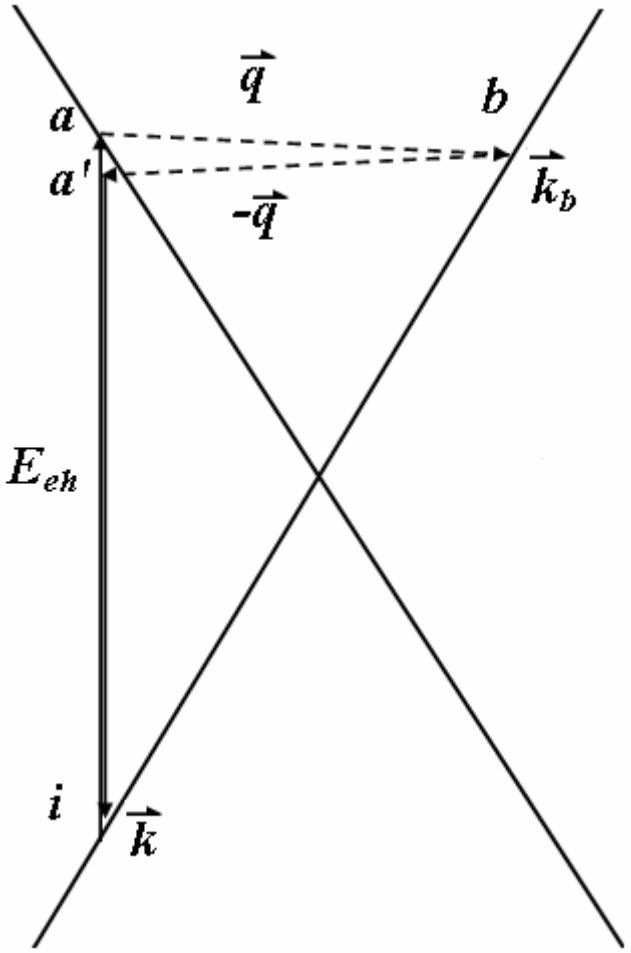

Figure 4.1: A schematic second-order double resonance Stokes process.

In Raman spectra of graphite, the frequency of bands under resonance would shift with the excitation energy, *i.e.* it is indeed an identifier of the resonant state energy. For example, the disorder-induced D band which appears at about 1350 cm^{-1} for 532 nm laser is a typical one. Due to double resonance effect, its frequency is highly dispersive and shifts with excitation energy by 44-51 cm^{-1}/eV over a wide energy range[8,9]. However, the D band would not appear in the Raman spectra of defect-free

graphite or graphene layers. For such systems, two-phonon scattering with zero total momentum would be enhanced by the double resonance effect too. Figure 4.1 illustrates a schematic second-order double resonance Stokes process with four virtual transitions: (i) e-h pair creation at wave vector k ($i \rightarrow a$ vertically) with the same energy as identical to the incident photon; (ii) electron-phonon scattering with an exchanged momentum $\boldsymbol{q}$ ($a \rightarrow b$); (iii) electron-phonon scattering with an exchanged momentum $-\boldsymbol{q}$ ($b \rightarrow a'$); (iv) e-h recombination ($a' \rightarrow i$ vertically). Under double resonance, as the excited e-h state is selected by the incident photon, the corresponding phonon states are tuned as well to match the energy and quasi-momentum conservation. It has been found that, the phonon dispersion relations of graphite can be probed over a wide range of the Brillouin zone by double resonance Raman spectroscopy[10]. Reversely, by the monotonic phonon dispersion ω_{ph} on the photon energy, the energy (E_{eh}) of e-h pairs of graphene can be deduced too.

4.2 Experimental

The graphene samples used in this study were prepared using the same method as described in Chapter 3.[1] Raman spectra and Raman image were carried out with WITEC CRM200 (532 nm, DPSSL laser), JY-T64000 (488 and 514 nm, Ar+ laser), and Renishaw inVia (325nm, He-Ne laser) Raman systems.

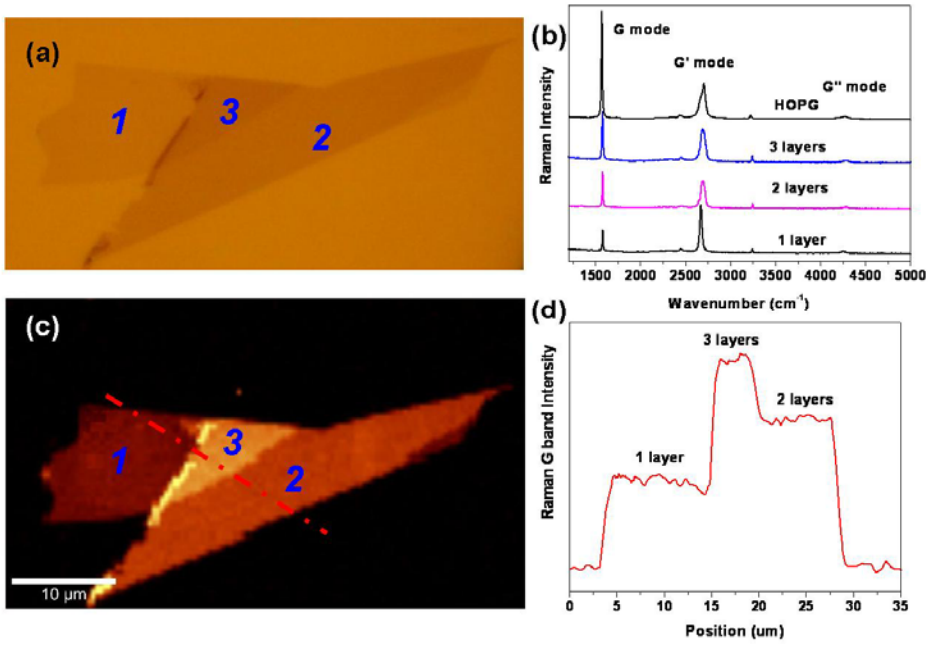

Figure 4.2 (a) optical image of graphene with 1, 2, and 3 layers. (b) Raman spectra as a function of number of graphene layers, as well as the Raman spectrum of HOPG. (c) Raman image plotted by the intensity of G band. (d) The cross section of Raman image, which corresponds to the dash line.

4.3 Results and discussion

Figure 4.2a shows the optical image of a graphene sample on the SiO_2/Si substrate. Raman spectra were then taken from the different regions of the sample and the results are shown in Figure 4.2b. For comparison, the Raman spectrum of bulk graphite, highly ordered pyrolytic graphite (HOPG), is also shown. There are two intense features in the spectra, which are the in-plane vibrational G band and the two

phonon G′ band, respectively. The frequency of G band is almost unchanged for graphene with different thickness. The single layer graphene has a sharp and symmetric G′ band, which makes it distinguishable from double- and multi- layer graphenes.[10] We further identified different layers of graphene from the G band intensity plot, as shown in Figure 4.2c.[11] Figure 4.2d plots the Raman intensity of the G band along the dash line. It is obvious that the graphene sheet contains one, two, three layers.

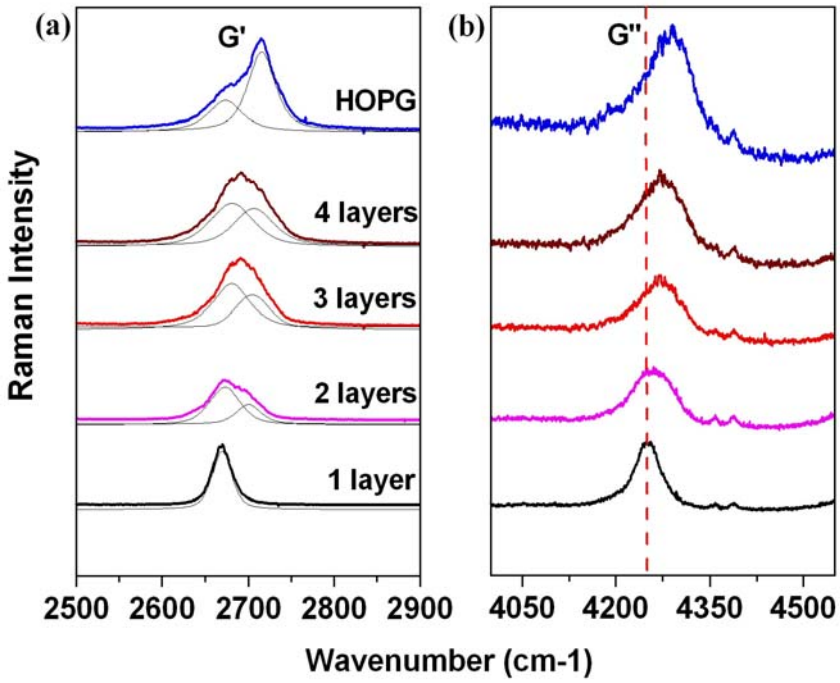

Figure 4.3 The G′ (a) and G″ (b) bands of graphene with one to four layers, as well as those of HOPG.

Figure 4.3a plots the G′ bands of graphene sheets in dependence of layer numbers, which shows a significant broadening and blue shift (center frequency) from single-layer graphene to double- and multi-layer graphene. Considering the two types of e-h pairs (intra- and inter-layer pairs) in graphene sheets, the broadening and blue shift can be easily understood. Since they have different interaction energy, the intra- and inter-layer e-h states select different phonon states and broaden the G′ bands of double- and multi- layer graphene sheets. On the other hand, selected by the high-energy intra-layer e-h states only, the G′ band of single-layer graphene is certainly sharper and with low frequency. Accordingly, by introducing the anisotropic behaviors of e-h pair states, we can explain clearly our observed Raman features: broadening and blue shift of G′ bands of graphene. In Figure 4.3a, the two fitted curves of double- and multi- layer graphene and HOPG correspond to the intra- and inter-layer e-h states. For HOPG, the split of two curves of G′ band is about 38 cm^{-1}, which will be used to estimate the energy difference of intra- and inter-layer e-h states later. Similarly, the three-phonon band (G″) which is located at ~4300 cm^{-1} can be ascribed to the different e-h states under triple resonance. Figure 4.3b shows the Raman G″ band of graphene sheet with one to four layers as well as that of bulk graphite. Similar to the two-phonon band, the G″ band of single layer graphene is as expected sharper and has a lower frequency than that of thicker graphene sheets and the bulk graphite. However, so far the resonant Raman features of graphene layers have not been clearly understood. Recently, from the electronic band splitting of double-layer graphene, Ferrari et al. successfully explained the broadening of the G′

band[10]. However, their model cannot explain the significant blueshift of the G′ band center frequency, as well as that of the three-phonon band (G″) and defect-induced band (D).

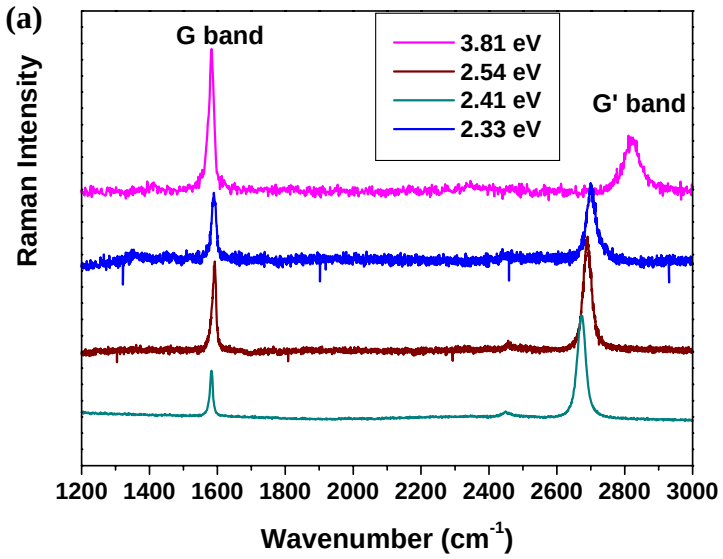

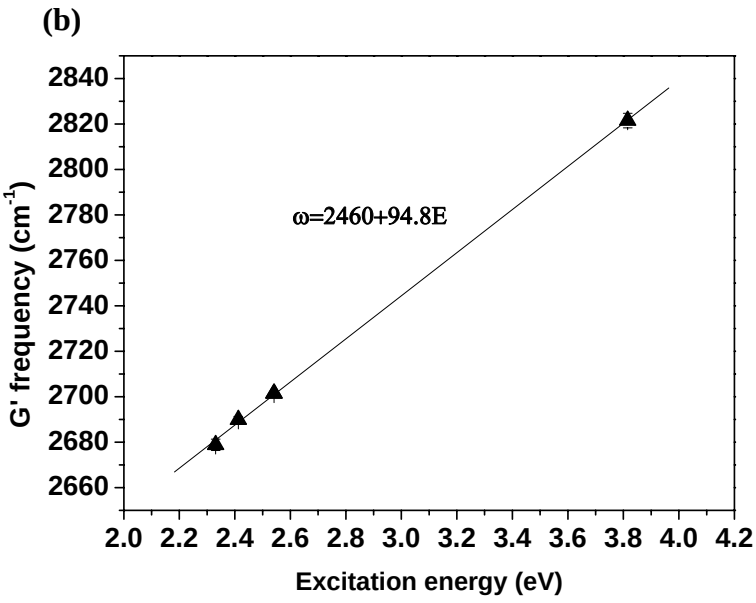

Figure 4.4 (a) The excitation energy dependence of the Raman spectrum of single layer graphene. The excitation source are 325 nm (3.81 eV), 488 nm (2.54 eV), 514 nm (2.41 eV), and 532 nm (2.33 eV). (b) The G′ band frequency of single layer graphene with different excitation energy.

Measuring the dispersion curve of the *G′* band of graphene on the incident laser energy is the key step to measure the energy difference ($E_{anisotropic}$) between the intra- and inter-layer e-h states. The idea is simple. Suppose, *G′* band under double resonance, the incident photon with energy of E_1 excites the intra-layer e-h state (E_1, $\boldsymbol{k}(\boldsymbol{q})$) and the inter-layer e-h state (E_1, $\boldsymbol{k'}(\boldsymbol{q'})$). As the intra-layer e-h state (E_2, $\boldsymbol{k'}(\boldsymbol{q'})$) can be obtained from the *G′* band dispersion curve of single layer graphene, we will have $E_{anisotropic}$ ($=E_2-E_1$) at the point of $\boldsymbol{k'}(\boldsymbol{q'})$. The excitation energy dependent Raman studies of graphene and the results of single layer graphene are shown in Figure 4.4a, with the excitation wavelength of 325, 488, 514 and 532 nm, respectively. Figure 4.4b shows the G′ frequency for different excitation energy, where the G′ frequency shifts with the equation:

$$\omega=2460+94.8E. \qquad (1)$$

where ω is the G′ frequency in cm^{-1} and E is the excitation energy in eV.

From equation (1), we calculated that the 38 cm^{-1} split ($\omega_2-\omega_1$) of bulk graphite G′ band corresponds to an excitation energy difference:

$$E_{anisotropic}=E_2-E_1=(\omega_2-\omega_1)/94.8=0.4 \text{ eV}, \qquad (2)$$

i.e. the anisotropy energy between the intra- and inter-layer e-h states is ~400 meV for 532 nm (2.33eV) excitation.

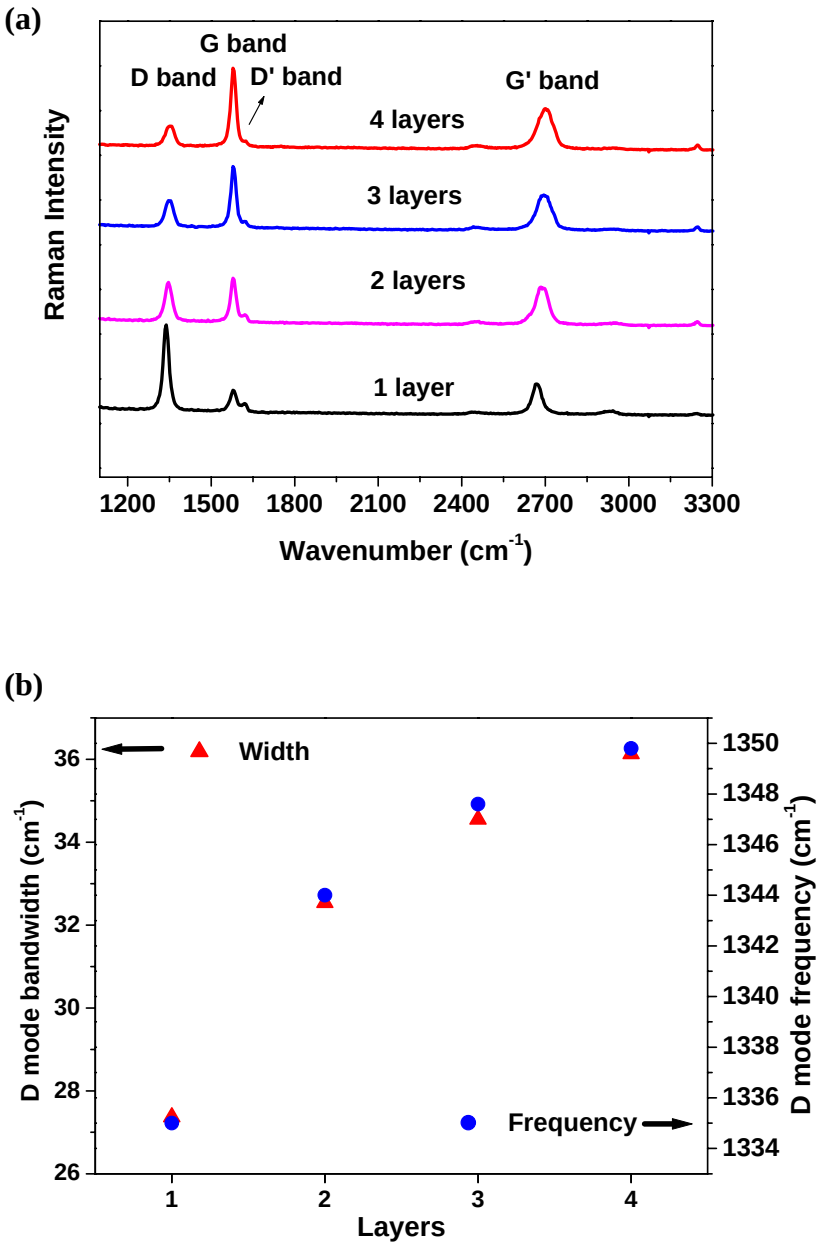

Figure 4.5 (a) Raman spectra of graphene with one to four layers after SiO_2 deposition. (b)The D band bandwidth (triangles) and frequency (circles) of graphene with one to four layers.

The D band is not observable in normal graphene samples as they are of high quality and do not contain defects. Only a very weak D band at the edge of the graphene sheet is sometimes observed. In order to study the thickness dependence of the one-phonon D band, we intentionally induced defects in the graphene samples by depositing a thin layer (5 nm) of SiO_2 on the samples. The Raman spectra of the SiO_2 coated samples are shown in Figure 4.5a. Both the D band and another defect-related Raman D′ band[12] located ~1620 cm^{-1} become observable, where the thinner sheets show stronger D band. The relative intensity of the D' band is also stronger for the thinner samples. Our observation can be understood as thicker samples are stiffer and more difficult to get damaged. As shown in Figure 4.5b, the D band of graphene becomes broader and shows blue shift as the graphene thicknesses increase, similar to that of G′ band. The simulation by Graf et al.[11] which interprets the G′ band using the evolution of electronic structure without considering e-h interactions reveals no significant shift (or even a slight red shift) of the phonon frequency (center of the peak) for thicker graphene sheets, which is inconsistent to the experimental results. Our model with e-h states in low dimension can interpret the phenomena properly.

4.4 Conclusion

In summary, the Resonant Raman features on the graphene layer numbers have be understood by the different selection from intra-layer and inter-layer e-h states. Taking the advantage of double resonance Raman effect, we have observed the confinement effect on e-h interaction energy of graphene, which may be as much as 400 meV for the 2.33 eV e-h state. At about 17 percent of the total energy of e-h pairs, such e-h attraction energy would modify significantly the qusiparticle dynamics of graphene layers. Therefore, in addition to the single particle behaviors within graphene layer systems, the e-h interaction should also be taken into account to understand their electronic and optical properties in further experimental and theoretical studies.

4.5 References

[1].K. S. Novoselov, A. K. Geim, S. V. Morozov, D. Jiang, Y. Zhang, S. V. Dubonos, I. V. Grigorieva, A. A. Firsov, *Science* **2004,** 306, 666.

[2].K. S. Novoselov, A. K. Geim, S. V. Morozov, D. Jiang, M. I. Katsnelson, I. V. Grigorieva, S. V. Dubonos, A. A. Firsov, *Nature* **2005,** 438, 197.

[3]. A. K. Geim, and K. S. Novoselov, K. S. Nature Mater. **2007,** 6, 183.

[4].P. R. Wallace, *Phys. Rev.* **1947,** 71, 622.

[5].G. W. Semenoff, *Phys. Rev. Lett.* **1984,** 53, 2449.

[6].X. F. He, *Phys. Rev. B* **1991,** 43, 2063.

[7]. A. Bostwick, T. Ohta, J. L. McChesney, K. V. Emtsev, T. Seyller, K. Horn, E. Rotenberg, *Preprint at http://arxiv.org/abs/cond-mat/07053705* **2006**.

[8]. C. Thomsen, S. Reich, *Phys. Rev. Lett.* **2000,** 85, 5214.

[9]. R. Saito, A. Jorio, A. G. Souza Filho, G. Dresselhaus, M. S. Dresselhaus, and M. A. Pimenta. *Phys. Rev. Lett.* **2000,** 88, 027401.

[10]. A. C. Ferrari, J. C. Meyer, V. Scardaci, C. Casiraghi, M. Lazzeri, F. Mauri, S. Piscanec, D. Jiang, K. S. Novoselov, S. Roth, A. K. Geim, *Phys. Rev. Lett.* **2006,** 97, 187401.

[11]. D. Graf, F. Molitor, K. Ensslin, C. Stampfer, A. Jungen, C. Hierold, L. Wirtz, *Nano Lett.* **2007,** 7, 238.

[12]. E. B. Barros, N. S. Demir, A. G. S. Filho, J. M. Filho, A. Jorio, G. Dresselhaus, M. S. Dresselhaus, *Phys. Rev. B* **2005,** 71, 165422.

Chapter 5

Tunable Strain and Controlled Thickness Modification in Graphene by Annealing

5.1 Introduction

Graphene has many exceptionally high crystallization and unique electronic properties, making it a promising candidate for ultrahigh speed nanoelectronics.[1-4] However, in order to make it a real technology, several critical issues need to be resolved which include but are not limited to (1) microelectronics compatible processes for fabricating both single layer and few layer graphene and related devices and (2) viable way of creating an energy gap at K and K′ points in the Brillouin zone. Researchers have successfully developed an energy gap in graphene by patterning it into nanoribbon,[5,6] forming quantum dots [4] or making use of mutilayer graphene sheets with or without the application of an external electrical field.[7-9] Besides global back gates,[10-12] top local gates [13-17] have also been employed to develop more complex graphene devices, such as pn junction,[18] Veselago lens [19] and Klein tunneling.[20] The top gate oxides that have been used so far include H_fO_2, Al_2O_3 and SiO_2. Although efforts have been made to deposit the gate oxides without damaging the graphene or changing its electrical properties,[13-17] the gate oxides should influence the graphene sheets in at least three ways: doping, defects, and various mechanical deformations. Although theoretical studies suggest that chemical doping shifts the neutral point

[1,21-23] and defects increase carrier scattering in graphene,[24-26] so far they have not been studied experimentally. It is known that the sp^2 bonds in graphitic carbon can hold extremely high mechanical strains [27,28] and exhibit interesting electromechanical properties, as observed in carbon nanotubes (CNTs).[29,30] Remarkable strain effects on optical and electronic properties have been found in CNTs.[29-36] As both the CNTs and graphene share the same honeycomb structure,[37] it is plausible to expect similar type of effects in graphene, especially in gapped structures such as graphene nanoribbon, quantum dot, and nano-constrictions.

We have studied systematically graphene sheets subjected to defects and mechanical deformations induced by insulating capping layers using Raman spectroscopy and Raman microscopy. Different insulating materials were deposited on top of graphene by electron beam evaporation, pulsed laser deposition (PLD), sputtering and followed by annealing at different temperatures. Here we present the results of using SiO_2 as a typical example. A thin layer of SiO_2 (5 nm) was deposited on top of the graphene sheets by PLD and Raman spectroscopy was used to investigate the interaction between the SiO_2 and graphene. Defect-induced Raman bands were observed after the deposition of SiO_2. The amount of defects was significantly reduced by annealing. A striking feature in our spectroscopic data is that compressive strain as high as ~3.5 GPa was observed after the annealing process. The compressive strain may be useful to tune the electronic properties of graphene nanostructures. Possible applications to graphene based devices and spectroscopic research are also presented. To the best of our knowledge, this is the first

experimental report on defects and strain induced in graphene. We further show that the graphene thickness, and hence its properties, can be changed in a controlled manner by annealing in air.

5.2 Experimental

The graphene samples were prepared by micromechanical cleavage on Si wafer substrate with a 300 nm SiO_2 cap layer and optical and Raman microscopies were used to locate the graphene sheet as described in Chapters 3 and 4. A 5 nm SiO_2 top layer was deposited by PLD with a 248 nm KrF pulsed laser. The laser power used was very weak (~200 mJ and repetition rate of 10Hz) to achieve the slow and smooth deposition (1Å/min) and ellipsometry was used to measure the total thickness of SiO_2. The SiO_2 thickness on the Si substrate was 303.5 $\pm$ 0.5 nm before deposition and 308.5 $\pm$ 0.5 nm after deposition, indicating that the thickness of top SiO_2 layer was 5 nm. The sample was annealed in a tube furnace at different temperatures for 30 min. Experimental details on Raman and contrast spectra and imaging are the same as described in Chapter 3.

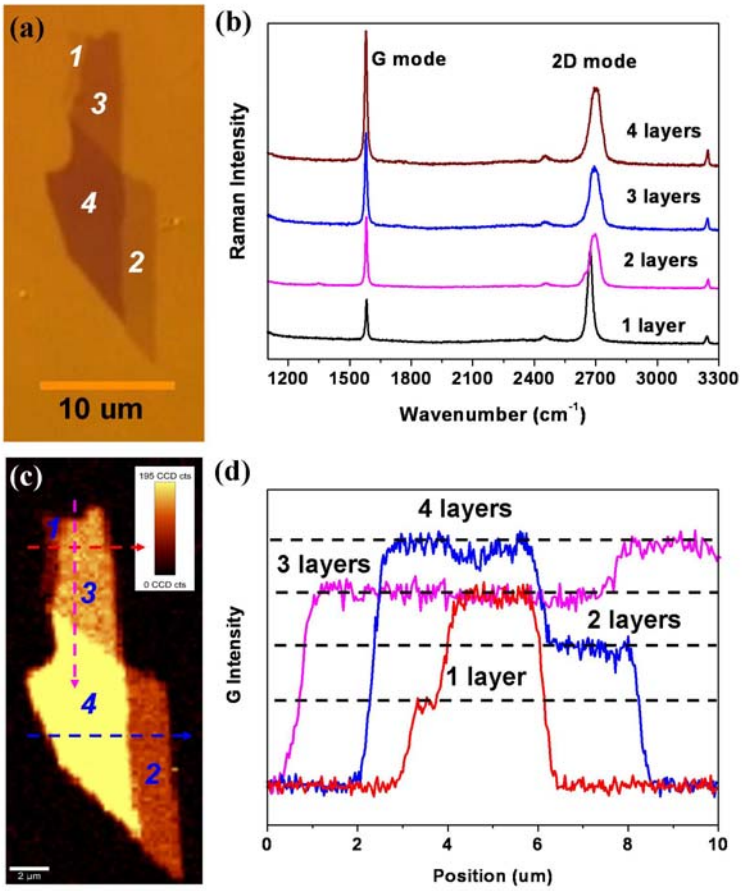

Figure 5.1 (a) Optical image of graphene with 1, 2, 3 and 4 layers. (b) Raman spectra as a function of number of layers. (c) Raman image plotted by the intensity of G band. (d) The cross section of Raman image, which corresponds to the dash lines with corresponding colors in Raman image.

5.3 Results and discussion

Figure 5.1a shows the optical image of a graphene sample on the SiO_2/Si substrate. The Raman spectra recorded from different regions are shown in Figure 5.1b. There are two intense features in the spectra, which are the in-plane vibrational G band and the two phonon 2D band, respectively. The single layer graphene has a sharp and symmetric 2D band, which makes it distinguishable from bilayer and few-layer graphenes.[38] We further identify the thickness of other layers from the G band intensity plot, as shown in Figure 5.1c.[39] The cross section in Figure 5.1d clearly shows that the graphene sheet contains one, two, three and four layers.

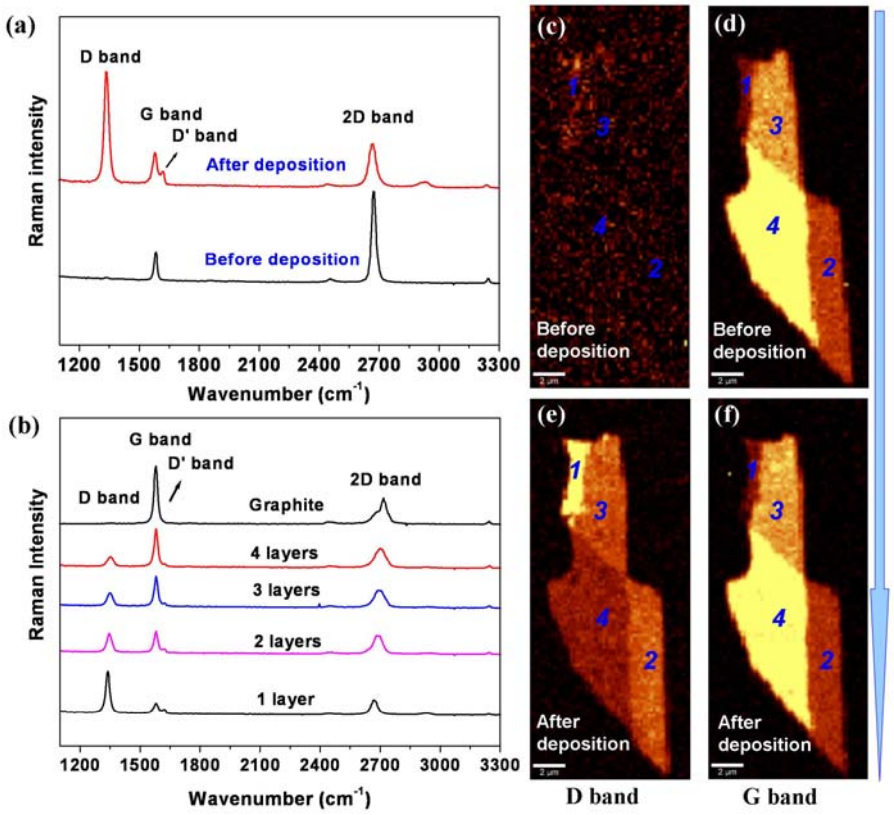

Figure 5.2 (a) Raman spectra of a graphene sheet before and after the 5 nm SiO_2 top layer deposition. (b) Raman spectra of graphene with one to four layers as well as that of bulk graphite after 5 nm SiO_2 top layer deposition. (c) Raman images of graphene sheets without SiO_2 cover generated from the intensity of the D band, and (d) the G band, together with the images generated from the sample graphene sheet after the 5 nm SiO_2 top layer deposition: (e) the D band, and (f) the G band.

The Raman spectra of graphene before and after 5 nm SiO_2 deposition were shown in Figure 5.2a. A clear difference is that two extra Raman bands, located at 1350 and 1620 cm^{-1}, were observed after deposition. Those two Raman bands were both defects induced: The stronger one at 1350 cm^{-1} is assigned to the so-called disorder-induced D band, which is activated by a double resonance effect by defects, such as in-plane substitutional hetero-atoms, vacancies, or grain boundaries.[40] The

weaker band at 1620 cm^{-1} is assigned to D′ band. The D′ band corresponds to the highest frequency feature in the density of state, which is forbidden under defect-free conditions.[41] Its observation is also associated with the presence of defects in the lattice and originates from the double resonance process. The observation of D and D′ bands indicate that defects were introduced into graphene after the 5 nm SiO_2 top layer deposition. This may be caused by the damage on the sample during deposition, or by the interaction between SiO_2 and graphene which may produce vacancy, dislocation and/or dangling bonds. The defect peaks were also observed in graphene with 5 nm SiO_2 top layer deposited by e-beam evaporation. Annealing is carried out to eliminate the defects, which will be discussed in latter section. Figure 5.2b shows the Raman spectra of graphene sheet with one to four layers as well as that of bulk graphite after SiO_2 deposition. The Raman spectra were taken under same conditions. The D band intensity decreases with the increase of graphene thickness and is invisible for bulk graphite, demonstrating that defects are more easily introduced into thinner graphene sheets.[42] Figure 5.2c and 5.2e show Raman images generated from the intensity of D band before and after deposition respectively. Before deposition, there is no D band hence the Raman image is dark. After deposition, the thinner graphene (single layer graphene) shows the strongest D band, which is consistent with the discussion above. Figure 5.3d and 5.3f show the images generated from the intensity of the corresponding G band, and they do not show noticeable difference. Hence the G band intensity is still a good criterion in determining the thickness of the graphene sheet.

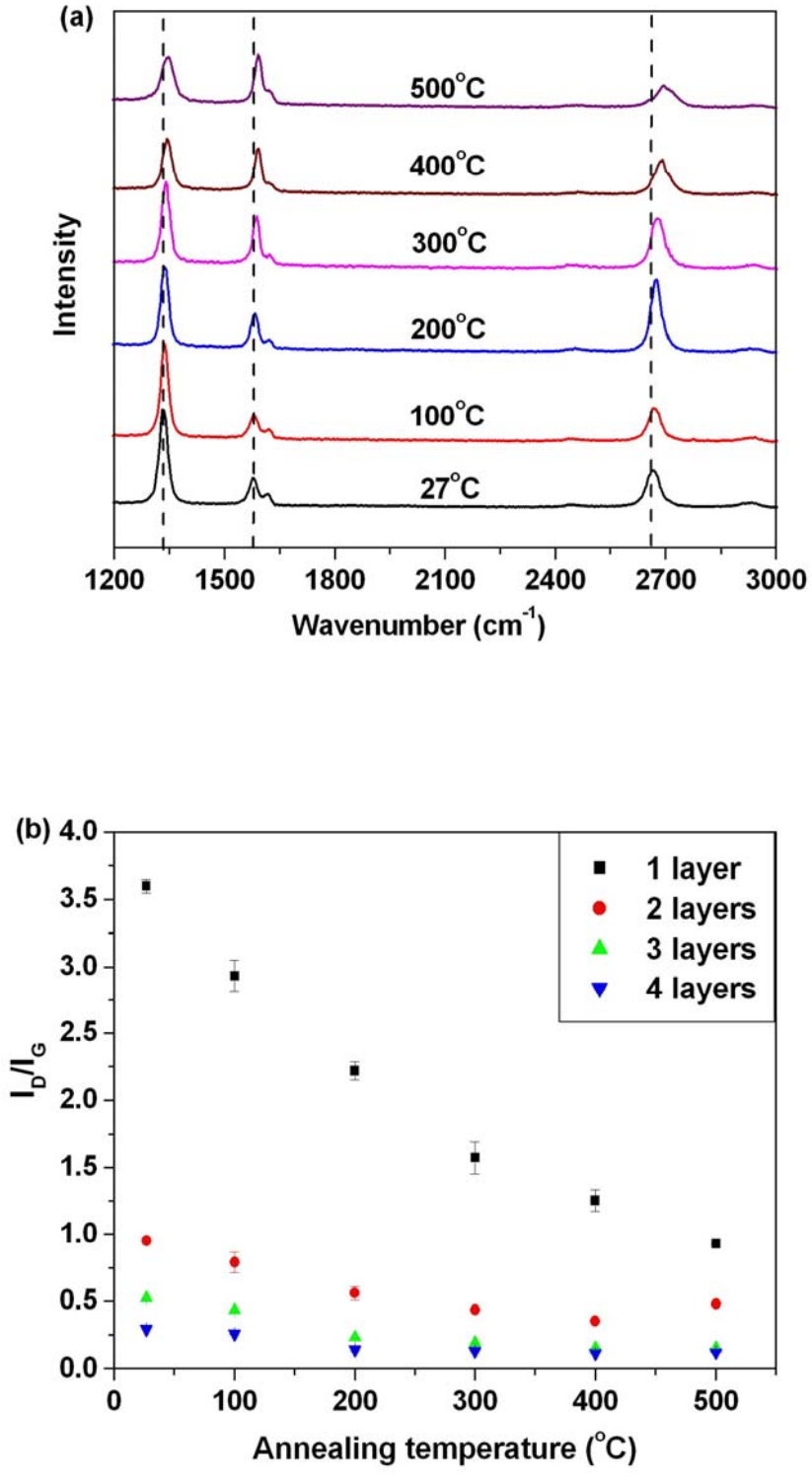

Figure 5.3 (a) Raman spectra of single layer graphene coated by 5 nm SiO_2 and annealed at different temperature. (b) The intensity ratio of D band and G band of graphene sheets with one to four layers (coated with SiO_2) after annealing at different temperatures.

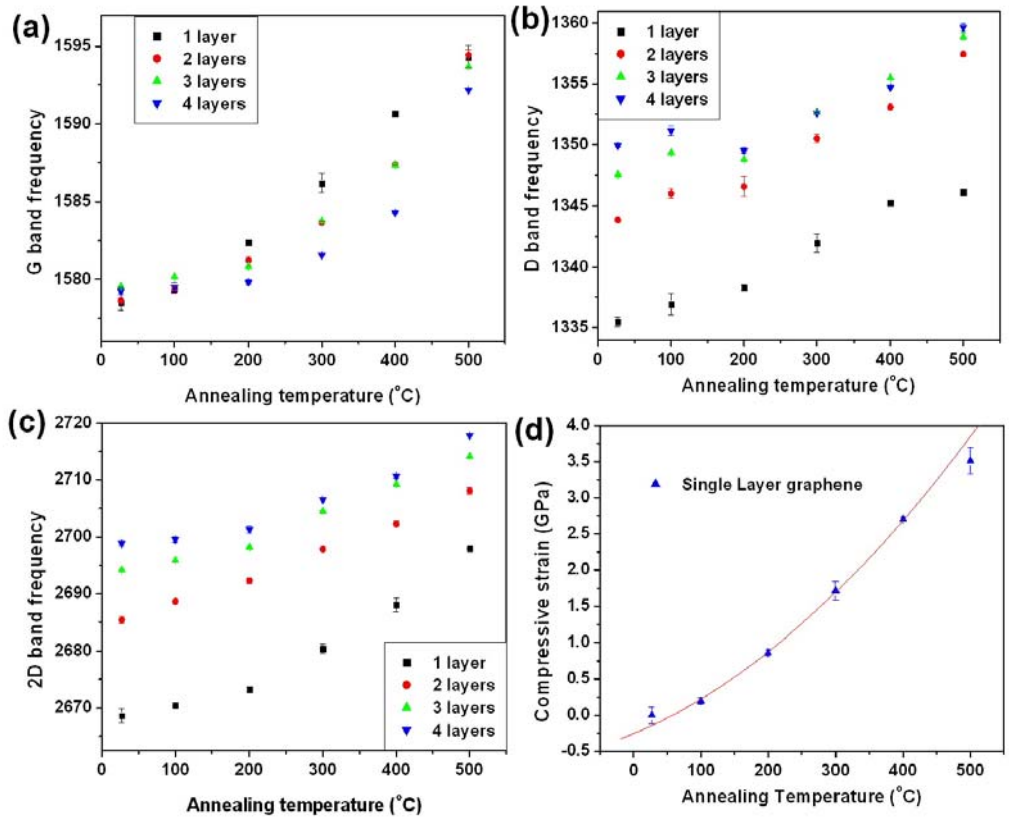

Figure 5.4 The Raman frequency of G band (a), D band (b), and 2D band (c) of graphene sheets with one to four layers (coated with SiO_2) after annealing at differenet temperature. (d) Strain on single layer graphene controlled by annealing temperature. The red line is a curve fit to the experimental data.

The Raman spectra of single layer graphene after annealing in air ambient at different temperatures are shown in Figure 5.3a. An obvious observation is that the intensity of D band decreases upon annealing. This is clearly demonstrated in Figure 5.3b, which shows the intensity ratio between the D band and G band (I_D/I_G) that is often used to estimate the amount of defects in carbon materials. For one to four-layer graphene sheets, this ratio decreases with increase in annealing temperature. This can be understood as due to the recovery of damaged graphene at high temperature.

Figure 5.4a-c show another important observation, where the G, D, and 2D bands shifted to higher frequency with increase in annealing temperature. The G band blue shifted ~15 cm^{-1}, while the D band blue shifted ~13 cm^{-1} and 2D band ~25 cm^{-1} after annealing at 500 ^{o}C. We attribute this significant blueshift of Raman bands to the compressive strain on graphene created by SiO_2 cover layer. The SiO_2 top layer becomes denser upon anneal so it exerted a stronger compressive strain on the graphene. For comparison, the Raman bands of bulk graphite did not shift after deposition and annealing, which supported the above explanation, as bulk graphite is too thick and it is not easily compressed by the thin SiO_2 layer. We also annealed the graphene without SiO_2 cover layer and no blueshift was observed for any of the Raman bands because the SiO_2 substrate is quite dense before annealing and its density does not change after annealing. This confirms that SiO_2 top layer plays an important role on the significant shift of Raman bands (compressive strain) of graphene after annealing. The strain was calculated by employing the pressure coefficient obtained from high hydrostatic pressure experiment. The pressure coefficient of G band frequency for graphite is 4.5 cm^{-1}/GPa,[43] and we have also performed high pressure experiment on another 2D carbon material (carbon nanowalls) where the pressure coefficient is 4.2 cm^{-1}/GPa, similar to that of graphite. Since they are all carbon materials with similarity in structure, it is reasonable to use the G band coefficient of 4.5 cm^{-1}/GPa as a rough estimate of the strain value. The strains on single layer graphene with annealing temperature are shown in Figure 5.4d. The compressive strain on graphene was as high as 3.5 GPa after depositing SiO_2 and

annealing at 500 ^{o}C, and the strain on single layer graphene in our experiment can be fitted by the following formula:

$$\varepsilon = -0.257 + 3.90\times10^{-3}\,T + 8.60\times10^{-6}\,T^{2}$$

where ε is the compressive strain in GPa and T is temperature in ^{o}C. The appearance of such large strain is mainly because graphene sheets are very thin (0.325 nm in thickness for single layer graphene),[44,45] so that they can be easily compressed or expanded. It has been reported that even the very weak van der waals interaction can produce large strain on the single wall carbon nanotubes.[36] We have also introduced tensile strain (~1GPa) onto graphene by depositing a thin cover layer of silicon. We suggest that tensile strain can be also achieved by depositing other materials with larger lattice constant than graphene. In combination with annealing, both compressive and tensile strains can be introduced and modified in graphene in a controllable manner. The strained graphene may have very important applications as the properties of graphene (optical and electronic properties) can be adjusted by strain, where strain studies in CNTs have already set good examples,[29-36] e.g. the bandgap of CNTs can be tuned by strain with a parameter of 100 meV per 1% strain.[31] Strain engineering using SiGe alloy has already been used in the IC fabrication to improve the device performance.

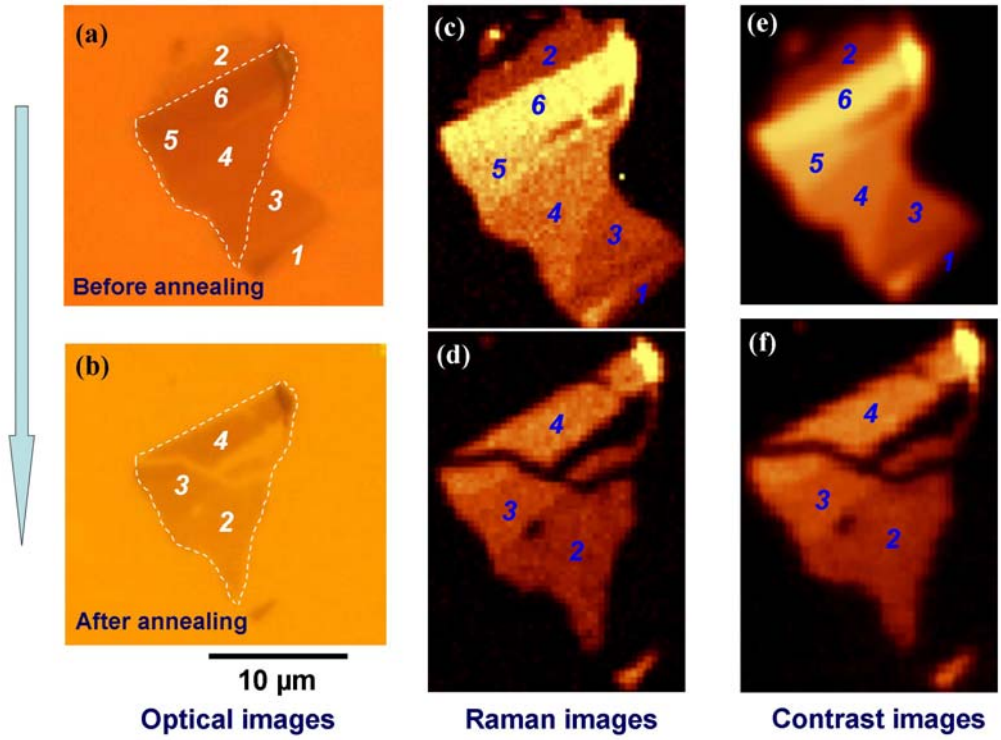

Figure 5.5 Optical images of a graphene sheet with one, two, three, four, and six layer regions before (a) and after (b) after annealed at 600 ^{o}C for 30 min. Raman (G band intensity) images of the same graphene before (c) and after (d) annealing. Contrast images of the same graphene before (e) and after (f) annealing. The one to three layer regions disappeared, while the four to six layer regions remained after annealing. The thicknesses of three remained regions were two, three, and four layers.

Figure 5.5a shows the optical image of a graphene sheet with one, two, three, four, five and six-layer regions, as denoted by the numbers on the image. After annealing at 600 ^{o}C for 30 min, the thinner part of graphene sheet (one to three layers) disappeared due to oxidation. However, the thicker part (four to six layers) still remained, as shown in Figure 5.5b. The thickness of different regions before and after anneal is determined by a combination of Raman imaging (Figure 5.5c and 5.5d) and contrast imaging (Figure 5.5e and 5.5f).[46] Optical spectroscopic imaging techniques have a

clear advantage in this case over other techniques, e.g. atomic force microscopy (AFM), in determining the layer thickness, as AFM does not work properly due to the presence of SiO_2 top layer on the graphene. Although the exact mechanism of graphene annihilation is unknown, it is most likely due to oxidation of carbon by oxygen diffused through the SiO_2 cover layer from the air ambient as the thickness of the graphenes does not change when anneal is carried out in vacuum. This result suggests that annealing in the presence of oxygen provides a practical method of manipulating the graphene thickness in a controllable manner. For example, a local heating techniques may be used to either induce the strain or reduce the thickness selectively, opening another avenue for fabricating graphene-based devices.

5.4 Conclusion

In summary, we have used Raman spectroscopy and microscopy to investigate the influence of top gate insulator (5 nm SiO_2) on graphene sheets mainly on two important aspects, defects and strain. The results show that defects were introduced in graphene sheets during deposition and the amounts of defects increase as the graphene thickness decreases. After annealing, the defects in graphene can be greatly reduced. Moreover, significant Raman shifts of all the graphene bands were observed after SiO_2 deposition and annealing, which was attributed to the compressive strain on graphene caused by the SiO_2 top layer. Importantly, the strain can be controlled by the annealing temperature, which maybe used to tune the optical and electronic properties similar to what has been observed in CNTs. Finally, the graphene thickness can be modified in a controllable manner using anneal. Our findings provide useful information critical to graphene device engineering and fabrication.

5.5 References

[1]. K. S. Novoselov, A. K. Geim, S. V. Morozov, D. Jiang, Y. Zhang, S. V. Dubonos, I. V. Grigorieva, A. A. Firsov, *Science* **2004**, *306*, 666.

[2]. K. S. Novoselov, A. K. Geim, S. V. Morozov, D. Jiang, M. I. Katsnelson, I. V. Grigorieva, S. V. Dubonos, A. A. Firsov, *Nature* **2005**, *438*, 197.

[3]. Y. B. Zhang, Y. W. Tan, H. L. Stormer, P. Kim, *Nature* **2005**, *438*, 201.

[4]. A. K. Geim, K. S. Novoselov, *Nature Materials* **2007**, *6*, 183.

[5]. Z. H. Chen, Y. M. Lin, M. J. Rooks, P. Avouris, Preprint at http://arxiv.org/abs/cond-mat/0701599 (**2007**).

[6]. M. Y. Han, B. Ozyilmaz, Y. B. Zhang, P. Kim, *Phys. Rev. Lett.* **2007**, *98*, 206805.

[7]. E. V. Castro, K. S. Novoselov, S. V. Morozov, N. M. R. Peres, J. M. B. Lopes dos Santos, J. Nilsson, F. Guinea, A. K. Geim, A. H. Castro Neto, Preprint at http://arxiv.org/abs/cond-mat /0611342 (**2006**).

[8]. E. McCann, *Phys. Rev. B* **2006**, *74*, 161403.

[9]. S. Latil, L. Henrard, *Phys. Rev. Lett.* **2006**, *97*, 036803.

[10]. Y. Zhang, Z. Jiang, J. P. Small, M. S. Purewal, Y. W. Tan, J. D. Fazlollahi, J. D. Chudow, J. A. Jaszczak, H. L. Stormer, P. Kim, *Phys. Rev. Lett.* **2006**, *96*, 136806.

[11]. K. S. Novoselov, E. McCann, S. V. Morozov, V. I. Fal'ko, M. I. Katsnelson, U. Zeitler, D. Jiang, F. Schedin, A. K. Geim, *Nature Physics* **2006**, *2*, 177.

[12]. Hubert B. Heersche, Pablo Jarillo-Herrero, Jeroen B. Oostinga, Lieven M. K. Vandersypen, Alberto F. Morpurgo, *Nature* **2007**, *446*, 56.

[13]. M. C. Lemme, T. J. Echtermeyer, M. Baus, H. Kurz, *IEEE Electr. Dev. Lett.* **2007**, *28*, 282.

[14]. G. Gu, S. Nie, R. M. Feenstra, R. P. Devaty, W. J. Choyke, W. K. Chan, M. K. Kane, *Appl. Phys. Lett.* **2007**, *90*, 253507.

[15]. B. Huard, J. A. Sulpizio, N. Stander, K. Todd, B. Yang, D. Goldhaber-Gordon, Preprint at http://arxiv.org/abs/ 0704.2626 (**2007**).

[16]. J. R. Williams, L. DiCarlo, C. M. Marcus, Preprint at the http://arxiv.org/abs/0704.3487 (**2007**).

[17]. B. Ozyilmaz, P. Jarillo-Herrero, D. Efetov, D. A. Abanin, L. S. Levitov, P. Kim, Preprint at http://arxiv.org/abs/ 0705.3044 (**2007**).

[18]. V. V. Cheianov, V. I. Fal′ko, *Phys. Rev. B* **2006**, *74*, 041403(R).

[19]. V. V. Cheianov, V. I. Fal'ko, B. L. Altshuler, *Science*, **2007**, *315*, 1252.

[20]. M. I. Katsnelson, K. S. Novoselov, A. K. Geim, *Nature Physics* **2006**, *2*, 620.

[21]. T. O. Wehling, K. S. Novoselov, S. V. Morozov, E. E. Vdovin, M. I. Katsnelson, A. K. Geim, A. I. Lichtenstein, Preprint at http://arxiv.org/abs/ cond-mat /0703390 (**2007**).

[22]. F. Schedin, K. S. Novoselov, S. V. Morozov, D. Jiang, E. H. Hill, P. Blake, A. K. Geim, Preprint at http://arxiv.org/abs/ cond-mat / 0610809 (**2006**).

[23]. E. H. Hwang, S. Adam,; S. Das Sarma, A. K. Geim, Preprint at http://arxiv.org/abs/ cond-mat / 0610834 (**2006**).

[24]. N. M. R. Peres, F. Guinea, A. H. Castro Neto, *Phys. Rev. B* **2006**, *73*, 125411.

[25]. P. M. Ostrovsky, I. V. Gornyi, A. D. Mirlin, *Phys. Rev. B* **2006**, *74*, 235443.

[26]. Vitor M. Pereira, F. Guinea, J. M. B. Lopes dos Santos, N. M. R. Peres, A. H. Castro Neto, *Phys. Rev. Lett.* **2006**, *96*, 036801.
[27]. M. F. Yu, O. Lourie, M. J. Dyer, K. Moloni, T. F. Kelly, R. S. Ruoff, *Science* **2000**, *287*, 637.
[28]. J. P. Salvetat, J. M. Bonard, N. H. Thomson, A. T. Kulik, L. Forro, W. Benoit, L. Zuppiroli, *Appl. Phys. A* **1999**, *69*, 255.
[29]. A. Maiti, A. Svizhenko, M. P. Anantram, *Phys. Rev. Lett.* **2002**, *88*, 126805.
[30]. J. Lee, H. Kim, S. J. Kahng, G. Kim, Y. W. Son, J. Ihm, H. Kato, Z. W. Wang, T. Okazaki, H. Shinohara, Y. Kuk, *Nature* **2002**, *415*, 1005.
[31]. E. D. Minot, Y. Yaish, V. Sazonova, J. Y. Park, M. Brink, P. L. McEuen, *Phys. Rev. Lett.* **2003**, *90*, 156401.
[32]. T. W. Tombler, C. Zhou, L. Alexseyev, J. Kong, H. Dai, L. Liu, C. S. Jayanthi, M. Tang, S. Wu, *Nature* **2000**, *405*, 769.
[33]. R. Heyd, A. Charlier, E. McRae, *Phys. Rev. B* **1997**, *55*, 6820.
[34]. L. Yang, J. Han, *Phys. Rev. Lett.* **2000**, *85*, 154.
[35]. S. B. Cronin, A. K. Swan, M. S. Ünlü, B. B. Goldberg, M. S. Dresselhaus, M. Tinkham, *Phys. Rev. Lett.* **2004**, *93*, 167401.
[36]. H. Son, G. G. Samsonidze, J. Kong, Y. Y. Zhang, X. J. Duan, J. Zhang, Z. F. Liu, *Appl. Phys. Lett.* **2007**, *90*, 253113
[37]. J. W. Mintmire, C. T. White, *Carbon* **1995**, *33*, 893.
[38]. A. C. Ferrari, J. C. Meyer, V. Scardaci, C. Casiraghi, M. Lazzeri, F. Mauri, S. Piscanec, D. Jiang, K. S. Novoselov, S. Roth, A. K. Geim, *Phys. Rev. Lett.* **2006**, *97*, 187401.
[39]. D. Graf, F. Molitor, K. Ensslin, C. Stampfer, A. Jungen, C. Hierold, L. Wirtz, *Nano Lett.* **2007**, *7*, 238.
[40]. C. Thomsen, S. Reich, *Phys. Rev. Lett.* **2000**, *85*, 5214.
[41]. E. B. Barros, N. S. Demir, A. G. Souza Filho, J. Mendes Filho, A. Jorio, G. Dresselhaus, M. S. Dresselhaus, *Phys. Rev. B* **2005**, *71*, 165422.
[42]. A. Gupta, G. Chen, P. Joshi, S. Tadigadapa, P. C. Eklund, *Nano Lett.* **2006**, *6*, 2667.
[43]. J. Sandler, M. S. P. Shaffer, A. H. Windle, M. P. Halsall, M. A. Montes-Moran, C. A. Cooper, R. J. Young, *Phys. Rev. B* **2003**, *67*, 035417.
[44]. B. T. Kelly, Physics of Graphite; Applied Science: London, **1981**.
[45]. M. S. Dresselhaus, G. Dresselhaus, P. C. Eklund, Science of Fullerenes and Carbon Nanotubes; Academic Press: San Diego, CA, **1996**; p 965.
[46]. Z. H. Ni, H. M.Wang, J. Kasim, H. M. Fan, T. Yu, Y. H. Wu, Y. P. Feng, Z. X. Shen, *Nano Lett* (online in press)

Chapter 6

Raman Spectroscopic Investigation of Carbon Nanowalls

6.1 Introduction

Self-assembled carbon nanostructures such as fullerenes and carbon nanotubes (CNTs) represent unusual forms of carbon in the nanometer regime.[1] Their unique crystalline structure and dimensionality bring about new mechanical, chemical and electronic properties. Recently, the two-dimensional carbon nanostructures have also been grown. Wu et al. [2, 3] reported the fabrication of two-dimensional carbon nanostructures—carbon nanowalls (CNWs), grown vertically using microwave plasma-enhanced chemical vapor deposition (PECVD). Hiramatsu et al. [4] have done further research on controlled fabrication of aligned carbon nanowalls.

Unlike CNTs, which are made from rolled up graphene sheets, CNWs comprise flat graphene sheets very similar to that in graphite. Due to the structural similarity, its properties (and hence Raman peaks) are closer to graphite than CNTs do. The large surface area of aligned carbon nanowalls are useful as templates for the fabrication of other types of nanostructured materials, which have potential applications in energy storage, as electrodes for fuel cells, sensors and field emission.[5] Furthermore, carbon sheets can be seen as the starting material to roll into nanotubes. A good understanding of its physical properties would help to know more about CNTs. Here, we employ Raman spectroscopy to investigate the crystalline structural and optical

properties of the CNWs.

Raman spectroscopy is a powerful tool and widely applied to determine the structural and electronic properties of various forms of carbon nanostructures. Single crystal graphite belongs to the D_{6h}^4 symmetry group, with the following optical vibrational modes, [6, 7]

$$\Gamma_{opt} = 2E_{2g}(R) + E_{1u}(IR) + 2B_{2g} + A_{2u}(IR)$$

The two E_{2g} modes are Raman active and have been identified with the Raman bands at ~1582 cm^{-1} (G band) and ~47 cm^{-1}, while the E_{1u} (~1588 cm^{-1}) and A_{2u} (~868 cm^{-1}) are IR active and observable with IR reflectance. In addition, there are also two Raman bands at ~1360 and ~1620 cm^{-1}, which are often designated as D and D′ modes. Wang et al. [7] have examined the first- and second-order Raman spectral features of graphite and related sp^2 bulk carbon materials with broad range of laser wavelengths. Siegal et al. [8] and Ohgoe et al. [9] studied the diamond like carbon (DLC) films and found sp^3 together with sp^2 in the DLC. Maultzsch et al. [10] found that only CNTs with $(n_1-n_2)/3$ being integer contribute to the D mode spectrum because of their particular electronic structure, the so-called chirality-selective Raman scattering of D band. In this chapter, we measured the Raman spectra of CNWs grown on silicon substrate. No unexpected peak was observed and all the peaks in the spectra are assigned. Compared with graphite and CNTs, the D band of CNWs is very strong due to the high edge density and surface oxidation. Excitation energy dependence of the D band was also carried out from 1.95 to 3.8 eV and discussed using the double resonance model.

6.2 Experimental

6.2.1 Growth of CNWs

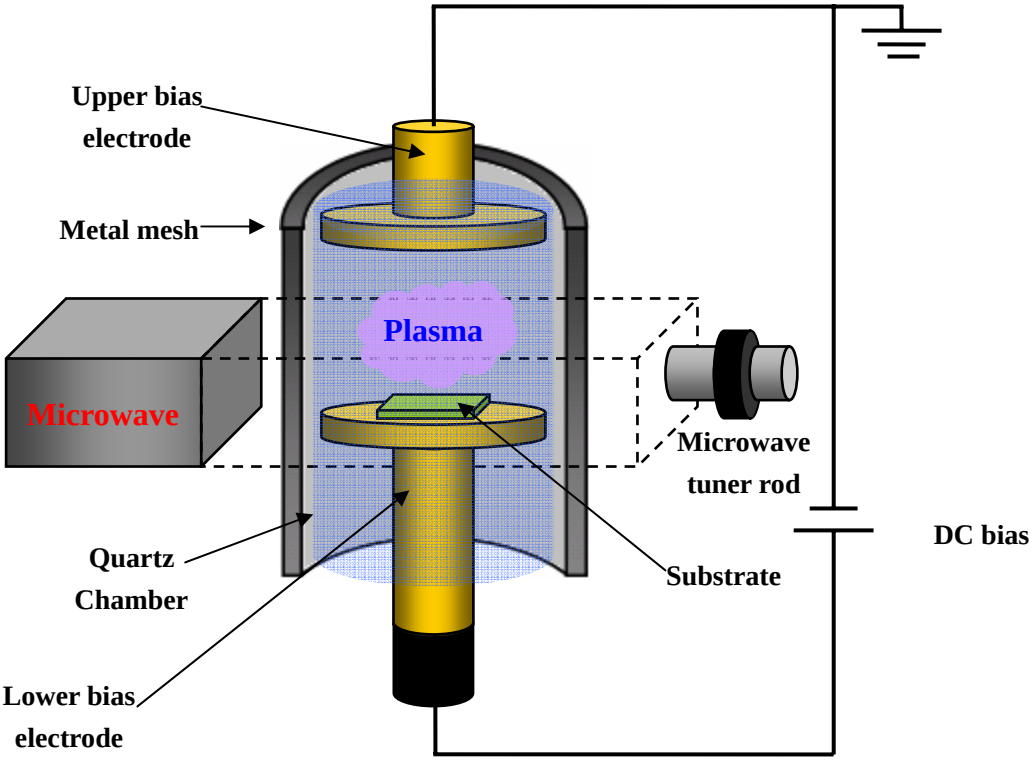

Figure 6.1 Schematic of micro-wave plasma enhanced chemical vapor deposition (PECVD) used to grow CNWs

CNWs were prepared using micro-wave plasma enhanced chemical vapor deposition (PECVD) on Si substrates (~ 1cm × 1cm in size).[2, 3] The Schematic of PECVD is shown in Figure 6.1. The PECVD system is equipped with a 500 W microwave source and a cavity to couple the microwave to a quartz tube for generating the plasma. Inside the quartz tube are two parallel plate electrodes placed 2 cm away from each other in the longitudinal direction of the tube that were used to

apply a DC bias to promote the growth and alignment of the both nanotubes and nanowalls. The gases used were mixtures of CH_4 and H_2. The typical flow rates of H_2 and CH_4 are 40 and 10 sccm, respectively. Before CH_4 was introduced to the quartz tube to commence the growth of nanotubes and nanowalls, the substrate was preheated to about 650-700 ^{0}C in hydrogen plasma without a bias for 8-10 min. During both preheating and growth, the process pressure was maintained at 1 Torr. A DC bias of -185 V was applied to the lower electrode on which the substrate was mounted while the top electrode was grounded.

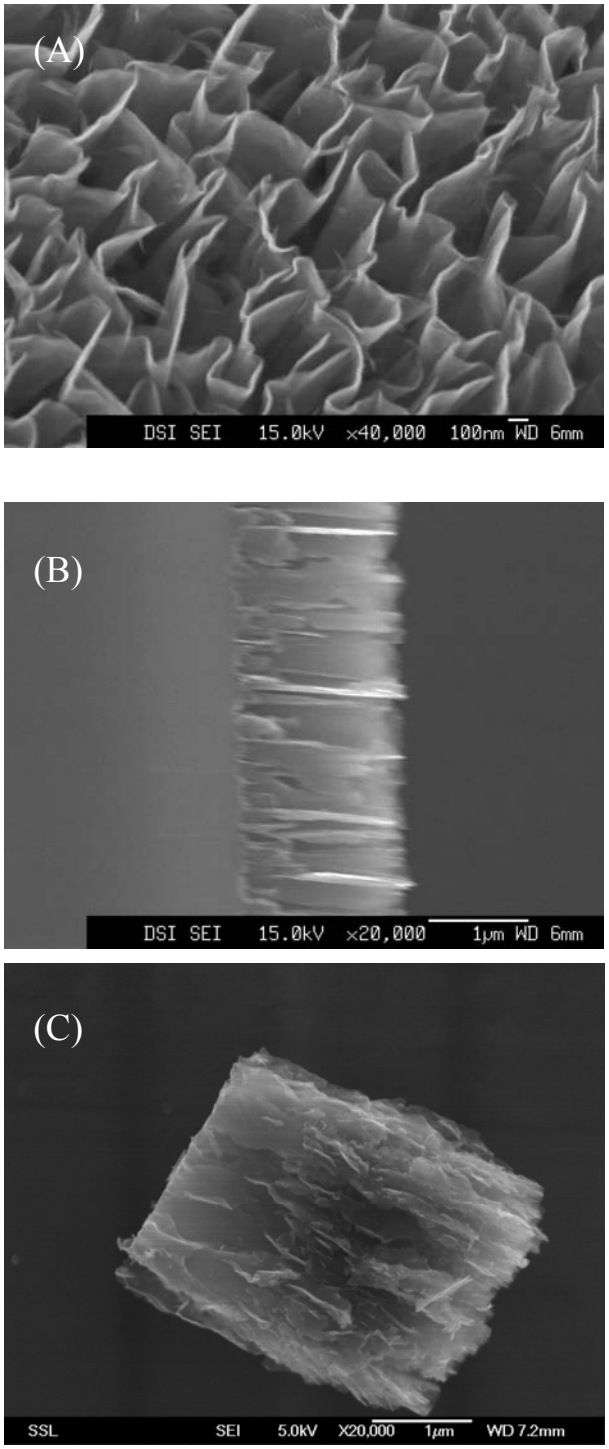

Figure 6.2 SEM images of CNWs grown on Si substrate using PECVD: (A) Top view of the CNWs. (B) Cross section of CNWs. (C) Several single layers scratched from the sample.

6.2.2 Experimental detail

The CNWs film samples grown by this method are very smooth and uniform. Figure 6.2 shows the SEM images of the CNWs samples. As can be seen in Figure 6.2 (A) and (B), the two-dimensional carbon sheets were grown vertically on the substrate. These CNWs have a lateral dimension in the micron range and a thickness of several nanometers. Figure 6.2 (C) shows the SEM image of carbon nanowall "mat" scratched out from the substrate, showing that the carbon nanowalls can be detached mechanically from substrate with ease. Micro-Raman spectra were recorded with different excitation lasers: 325, 633, 488, 514.5 and 532nm. Raman measurements were recorded in different sample orientations and polarizations. All the Raman spectra were performed in the backscattering geometry at room temperature. The laser power on sample is kept below 1 mW to ensure that the lasers do not heat the samples, which can induce Raman shift. The resolution of the micro-Raman is below 1 cm^{-1}.

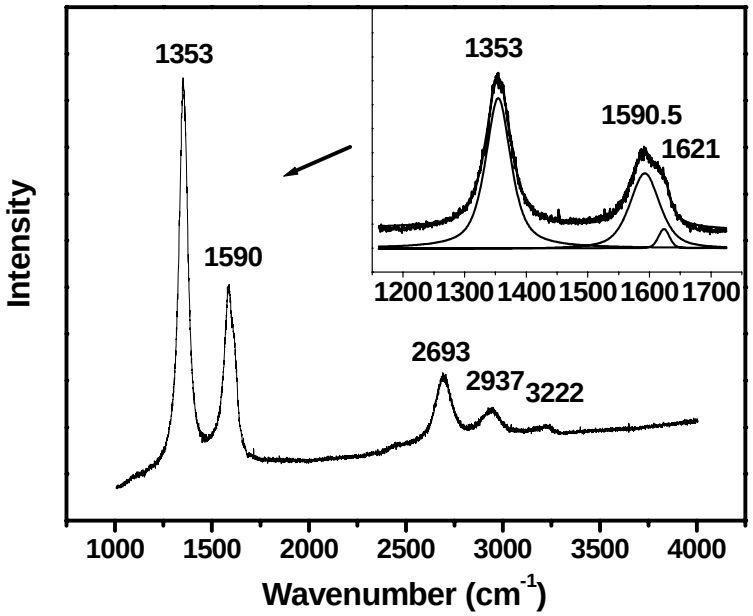

Figure 6.3 Raman spectrum of CNWs excited by 514 nm laser line, the insert shows the 1000-1800 cm^{-1} range, together with fitted peaks.

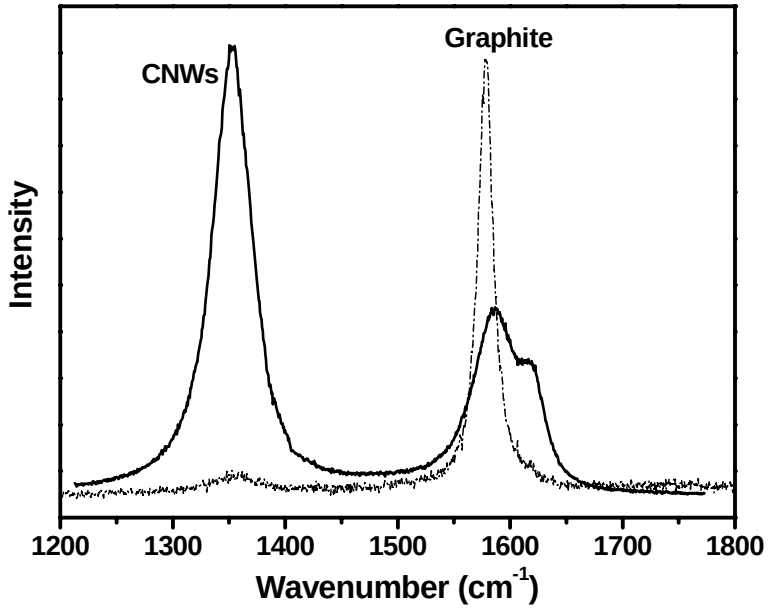

Figure 6.4 Raman spectra of graphite and CNWs excited by 514 nm laser line.

6.3 Results and discussion

6.3.1 Raman characterization of CNWs

Figure 6.3 shows the Raman spectrum of CNWs using 514 nm excitation. There are total five peaks from 1000 to 4000 cm^{-1}. We have also made measurement below 1000 cm^{-1}. As expected, no "breathing mode", which is characteristic of CNTs, was observed in the range of 100 cm^{-1} to 1000 cm^{-1}. The peak at 1590 cm^{-1} is the Raman-active G band (E_{2g}) originated from the in-plane vibrational mode. [6, 7] The peak at 1353 cm^{-1} is assigned to the so-called disorder-induced D band, which is activated in the first-order scattering process and usually thought to be due to the presence of in-plane substitutional hetero-atoms, vacancies, grain boundaries or other defects, all of which lower the crystalline symmetry. In the case of highly ordered pyrolytic graphite (HOPG), the D band disappears and only the G band exhibits in the fundamental region between 1100 and 1700 cm^{-1}.[11-13] Beside the G band, a distinct shoulder peak at 1621cm^{-1} attributed to D′ band is often observed in some disordered graphite-like carbons. The D′ band corresponds to the highest frequency feature in the density of states, which is forbidden under defect-free conditions.[11] Its observation is also associated with the presence of defects in the lattice and originates from the $q \sim 2k$ phonons close to the Brillouin zone center.[14-16] In the region of the higher order Raman spectrum, three distinct peaks are attributed to combinations of the Raman fundamentals, 2693 (2D), 2937 (D+G) and 3222 cm^{-1}(2D′). These bands have also been observed in the Raman spectra of HOPG. [17-19]

For a better understanding of the features of CNWs, the Raman spectrum of CNWs is compared with that of the bulk graphite (shown in Figure 6.4). The G band of CNWs has a slightly higher frequency and is also broader than that of graphite, which can be attributed to the breakdown of selection rule caused by defects and small size. Maultzsch et al. [20] have measured the phonon dispersion of graphite by inelastic x-ray scattering. It showed that the E_{2g} LO phonon branch (~1582 cm^{-1}) has positive phonon dispersion near the Γ point. The breakdown of |q|=0 selection rule allows the observation of vibrational modes correspond to a wider wave vector range, which resulted in the upshift and broadening of the G band. The intensity ratio of the D and G bands is about 2.2 for CNWs using 514nm excitation laser. This ratio is higher than that of graphite [6,7] as the CNWs contains more defects. However, one must exercise care in such comparison since the intensity of the band not only depends on the defects but also excitation energy. Unlike the SWCNTs, [10] the D band for CNWs can be fitted with a single Lorentzian peak and does not show any fine structure.

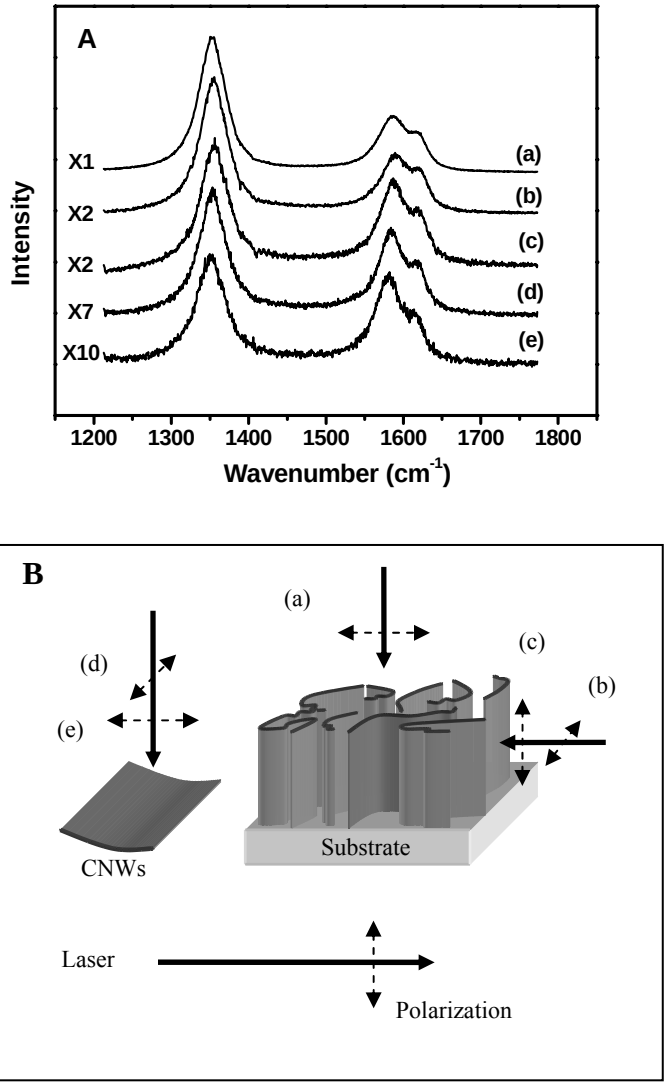

Figure 6.5A Raman spectra of CNWs recorded at different configurations (see Figure 6.5B) using 514 nm laser line. (a) laser light perpendicular to the substrate. (b) and (c), laser light parallel to CNWs film (cross section) with the polarization of (b) parallel to the substrate and (c) parallel to the growth direction of the wall. (d) and (e), laser incident normally to the surface of a scratched sample, consisting several single walls. The polarization of (d) and (e) are parallel to the wall surface but with cross direction.
Figure 6.5B Schematic diagram showing the CNWs samples, the laser light and its polarization, at five different configurations (a), (b), (c), (d), (e).

6.3.2 Orientation dependent Raman study of CNWs

Figure 6.5A shows Raman spectra of CNWs for five different configurations between the laser light polarization and CNWs orientation (illustrated in Figure 6.5B) recorded using the 514 nm laser line. The I_D/I_G ratio for the five configurations is 2.43(a), 2.31(b), 1.48(c), 1.46(d) and 1.35(e) respectively. This difference can be explained as due to the polarization effect of G band.[21] In spectrum (a), the Raman spectrum was recorded perpendicularly to the substrate. In this configuration, the laser polarization does not affect the experiment result as it represents the average of different angles between the laser light polarization and normal direction of CNWs. This is consistent with the fact that the spectrum is almost unchanged in this orientation with the change in the laser polarization. In spectra (b) and (c) (cross-section scattering), the laser was scanned from the cross section of the CNWs film. Taken into account the randomness of the CNWs orientations in the substrate plane, spectrum (b) should be identical to spectrum (a). In our experiments, the I_D/I_G ratio of these two conditions is quite similar: 2.43(a) and 2.31(b). In spectrum (c), the in-plane vibrational G mode is enhanced because the polarization is parallel to all of the walls (not affected by the random arrangement within the substrate plane). Obviously, the I_D/I_G ratio of 1.48(c) is smaller compared with the first two conditions. Spectra (d) and (e) were taken perpendicularly to several single walls (SEM in Figure 6.2C). Similar to (c), the polarizations of laser for both (d) and (e) are parallel to the wall surface. The I_D/I_G ratio of 1.46(d) and 1.35(e) are quite similar to 1.48 (c). From

the above results, the dependence of intensity on polarization direction implies that the graphene planes in the CNWs are parallel to the surface of individual CNWs and well-crystallized.

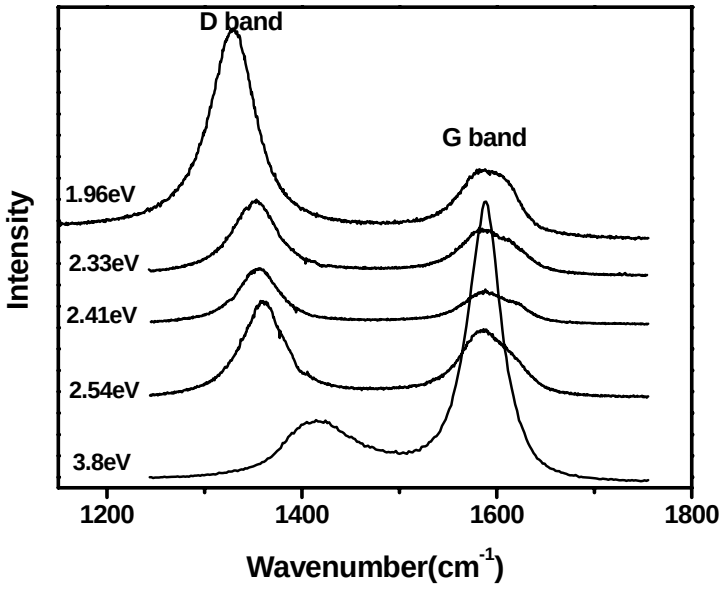

Figure 6.6. Raman spectra of CNWs excited by different laser lines: 325nm(3.8eV), 488nm(2.54eV), 514nm(2.41eV), 532nm(2.33eV), and 633nm(1.96eV).

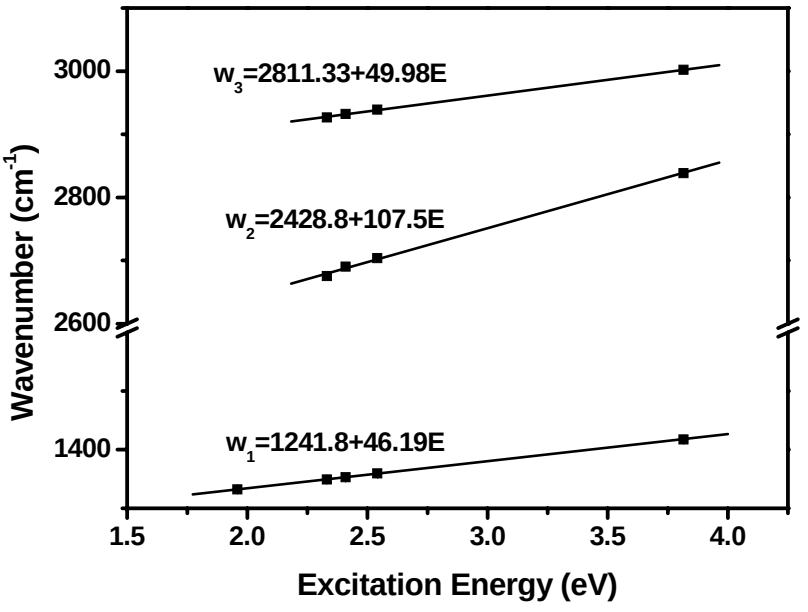

Figure 6.7 The frequencies of Raman mode (D band, 2D band, D+G band) of CNWs as a function of excitation energy.

6.3.3 Laser excitation dependent Raman study off CNWs

The excitation laser energy dependence of the frequency of disorder-induced D band is one of the most interesting features of the Raman spectra in sp^2 carbon materials. [22] Its frequency is highly dispersive and increases with increasing laser excitation energy at a rate of about 51 cm^{-1}/eV. [23] This dispersive nature [24] as well as discrepancy between the D-band Stokes and anti-Stokes frequencies [25] has been explained recently by a double resonance process.[16, 26] Double resonances, where two of the intermediate electronic states in the scattering process have to be real, occur more easily in semimetal-like graphite if the sample contains symmetry breaking elements. Based on the double resonance mechanism, the intensity of the observed D-band is proportional to the density of defects.

The Raman spectra of CNWs with different excitation energy are shown in Figure 6.6. The peak positions of the D band are plotted as a function of laser energy as shown in Figure 6.7, which also contains the peak position dependence on laser energy of the 2693 (2D) and 2937 cm^{-1} (D+G) bands. The G band is almost independent of excitation laser energy, while the D band shows a good linear shift (a rate of 46.19 cm^{-1}/eV). The 2D band has a slope of 107.5 cm^{-1}/eV, which is approximately twice that of the D band. The D+G band has a slope of 48.98 cm^{-1}/eV similar to that of the D band, which is expected since the G band does not shift with excitation energy. Recently, J. Maultzsch et al.[27] presented an in-depth analysis of double-resonant Raman scattering. The calculation result indicates that the D-mode

shows a shift between 43-61 cm^{-1} /eV, agreeing well with our experimental result.

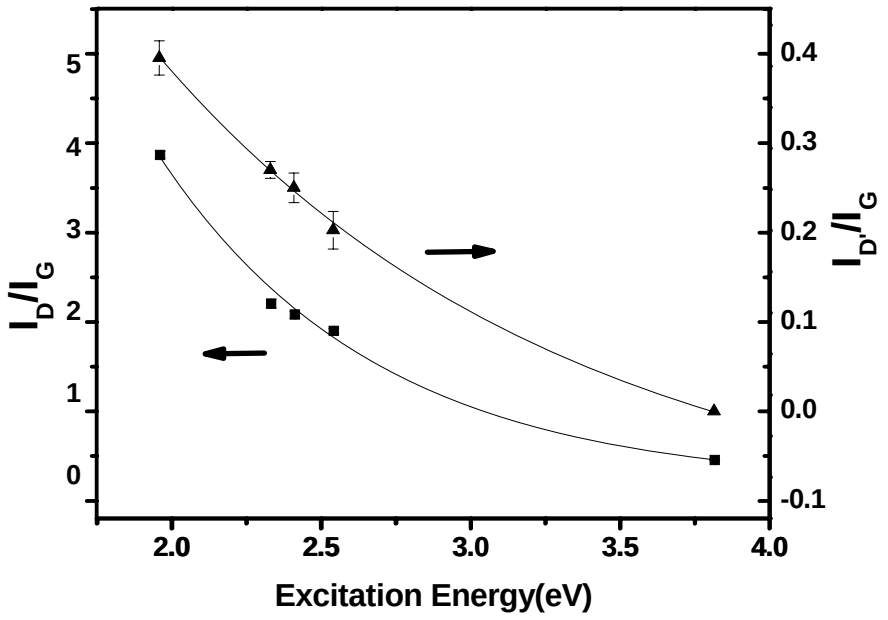

Figure 6.8. The intensity ratio of D band to G band I_D/I_G (squares) and D′ band to G band $I_{D'}/I_G$ (triangles) with excitation energy.

Besides, we have also measured the intensity ratio of the D and G bands, shown in Figure 6.8 (squares). The ratio I_D/I_G decreases as the excitation energy increases. Similar result has also been observed by Mernagh et al. [28] in graphon carbon and Wang et al. [7] in glassy carbon. It was likely due to the resonance (vibronic) enhancement. The resonance enhancement for the D mode favors longer wavelength while the G mode favors shorter wavelength, which resulted in the relatively smooth changes of I_D/I_G. There is significant variation in the peak intensity ratio I_D/I_G by about a factor of 16 between Raman spectra recorded using λ = 325 and 633 nm lasers. The variation is much larger than that of glassy carbon and graphon, indicating that

the CNWs may have electronic structure and phonon dispersion that differ from these materials.

Similarly, the relative intensity $I_{D'}/I_G$ of the D′ band (1620 cm^{-1}) and G band also decreases as the excitation energy increases as shown in Figure 6.8 (triangles). The excitation laser energy dependence of the D′ band intensity follows that of the D band. Tan et al. [14] observed in graphite whiskers that the frequency of the D′ band shifts slightly as the excitation energy varies. This shift is not easy to observe in CNWs where the G and D′ bands overlap. The similar behaviors of the D band and D′ band again indicates that the D′ band is associated with the presence of defects and originates also from a double resonance process involving $q \sim 2k$ phonons close to the Brillouin zone center but with a relatively flat dispersion.

6.4 Conclusion

In summary, 2D CNWs were grown by PECVD and SEM was used to study the morphology, and micro-Raman scattering experiments have been performed. All the observed peaks were assigned and compared with graphite. The extremely strong D band of CNWs was mainly attributed to the defects and high edge density. The G band shows strong polarization dependence. Different laser lines were used to excite the sample. The frequency of the D band shifts with the laser energy at a rate of 46.19 cm^{-1}/eV, and this result agrees well with the theoretical value by double resonance effect. The 2D and D+G bands shift at the rate of 107.5 cm^{-1}/eV and 48.98 cm^{-1}/eV respectively. The decreasing intensity ratios I_D/I_G and $I_{D'}/I_G$ with the increasing laser energy are observed and discussed.

6.5 References

[1]. M. S. Dresselhaus, G. Dresselhaus, P. C. Eklund, Science of Fullerenes and Carbon Nanotubes, Academic Press, New York **1996**.
[2]. Y. H. Wu, P. W. Qiao, T. C. Chong, and Z. X. Shen, Adv. Mater. **2002**, 14, 64.
[3]. Y. H. Wu and B. J. Yang, Nano Letters **2002**, 2, 355.
[4]. M. Hiramatsu, K. Shiji, H. Amano, and M. Hori, Applied Physics Letters **2004**, 84, 4708.
[5]. B. J. Yang, Y. H. Wu, B. Y. Zong and Z. X. Shen, Nano Letters **2002**, 2, 751.
[6]. P. H. Tan, Y. M. Deng, and Q. Zhao, Physical Review B **1998**, 58, 5435.
[7]. Yan Wang, Daniel C. Alsmeyer and Richard L. McCreery, Chem. Mater. **1990**, 2, 557.
[8]. M. P. Siegal and D. R. Tallant, et al. , Physical Review B **2000**, 61, 10451.
[9]. Yasuharu Ohgoe and Kenji K. Hirakuri, Journal of Applied Physics **2005**, 97, 024906.
[10]. J. Maultzsch, S. Reich, and C. Thomsen, Physical Review B, **2001**, 64, 121407(R).
[11]. R. J. Nemanich, S. A Solin, Physical Review B **1979**, 20, 392.
[12]. R. Vidano, D. B. Fischbach, J. Am. Ceram. SOC. **1978**, 61, 13.
[13]. R. Al-Jishi, G. Dresselhaus, Physical Review B **1982**, 26, 4514.
[14]. P. H. Tan, C. Y. Hu, J. Dong, W. C. Shen, and B. F. Zhang, Physical Review B **2001**, 64, 214301.
[15]. E. B. Barros, N. S. Demir, A. G. Souza Filho, J. Mendes Filho, A. Jorio, G. Dresselhaus, and M. S. Dresselhaus, Physical Review B **2005**, 71, 165422.
[16]. R. Saito, A. Joria, A. G. Souza Filho, G. Dresselhaus, M. S. Dresselhaus, and M. A. Pimenta, Physical Review Letters **2002**, 88, 027401.
[17]. B. S. Elman, M. Shayegan, M. S. Dresselhaus, H. Mazurek, and G. Dresselhaus, Physical Review B **1982**, 25, 4142.
[18]. B. S. Elman, M. S. Dresselhaus, G. Dresselhaus, E. W. Maby, and H. Mazurek, Physical Review B **1981**, 24, 1027.
[19]. M. A. Pimenta, E. B. Hanlon, A. Marucci, P. Corio, S. D. M. Brown, S. A. Empedocles, M. G. Bawendi, G. Dresselhaus, M. S. Dresselhaus, Braz. J. Phys. **2000**, 30, 423.
[20]. J. Maultzsch, S. Reich, C. Thomsen, H. Requardt, and P. Ordejon, Physical Review Letters **2004**, 92, 075501.
[21]. Yasushi Kawashima and Gen Katagiri, Physical Review B **1999**, 59, 62.
[22]. A. C. Dillon, P. A. Parilla, J. L. Alleman, T. Gennett, K. M. Jones and M. J. Heben, Chemical Physics Letters **2005**, 401, 522.
[23]. M. J. Matthews and M. A. Pimenta et al. , Physical Review B **1999**, 59, 6585.
[24]. R. Saito, A. Jorio, A. G. Souza Filho, G. Dresselhaus, M. S. Dresselhaus, A. Gruneis, L. G. Cancado, M. A. Pimenta, Jpn. J. Appl. Phys. **2002**, 41, 4878.
[25]. V. Zolyomi, J. Kurti, Physical Review B **2002**, 66, 073418.
[26]. C. Thomsen and S. Reich, Physical Review Letters **2000**, 85, 5214.
[27]. J. Maultzsch, S. Reich, and C. Thomsen, Physical Review B **2004**, 70, 155403.

[28]. Terrence P. Mernagh, Ralph P. Cooney and Robert A. Johnson, Carbon **1984**, 22, 39.

Chapter 7

High Temperature Raman Spectroscopy Studies of Carbon Nanowalls

7.1 Introduction

Thermal stability is an important property of the carbon materials. The temperature-induced shifts of the first-order Raman peaks have been reported on diamond by Zouboulis *et al.* [1] and on graphite by Tan *et al*. [2] For the carbon nanomaterials, Ci *et al*. found that the G mode temperature coefficient is different for different sizes of CNTs.[3] Osswald *et al*. carried out high temperature Raman spectroscopy studies of single wall carbon nanotubes (SWCNTs) and double wall carbon nanotubes (DWCNTs).[4] They found that the temperature coefficient of DWCNTs is between that of SWCNTs and graphite. Moreover, they observed the elimination of D mode between 440 ℃- 500 ℃ for SWCNTs and 370 ℃ - 400 ℃ for DWCNTs, and they concluded that the D mode of CNTs comes from amorphous carbon on the surface and also the damaged tubes.

So far, there has been no study on temperature dependence of CNWs, though such study is necessary for a clearer understanding of thermal stability of CNWs. In this chapter, we studied the contribution of surface amorphous carbon on the intensity of the D mode, as well as the origin of the extremely strong D mode of CNWs. What is more, by heating the sample at air condition, we would be able to eliminate the

surface amorphous carbon and hence its related defects in CNWs.

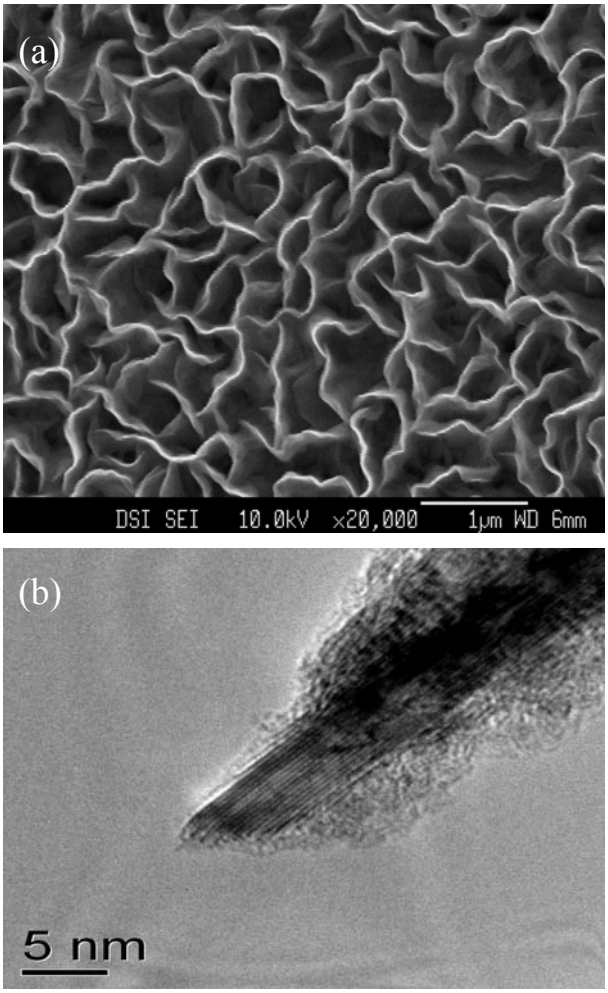

Fig. 7.1 (a) SEM image of CNWs grown on Si substrate using PECVD. (b) TEM image of the cross section of CNWs. The graphene planes which formed the wall were vertically aligned. There is some amorphous carbon on the surface of the wall.

7.2 Experimental

The growth of CNWs has been described in detail in chapter 6. Figure 7.1a shows the SEM micrograph of CNWs. The TEM image (Figure 7.1b) shows the cross section of a single carbon nanowall, the graphene planes which form the wall are clearly shown. In addition, there is some amorphous carbon on the surface of the wall. The high temperature Raman experiments were carried out in static air ambient using

a THMS 600 Linkam thermal stage with ~1°C temperature accuracy and stability. The sample was heated up to 600 °C at 5 °C/min, and held for 5 min at every measurement point. Raman spectra were recorded as described in Chapter 6. The integral (area) intensities of Raman bands were used in calculating the intensity ratio.

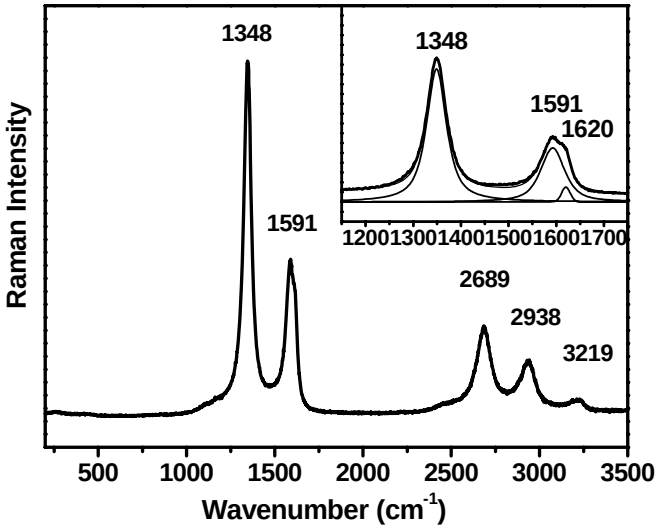

Fig. 7.2 Raman spectrum of CNWs excited by 532nm laser. The inset shows the 1150-1750 cm^{-1} range, together with fitted peaks.

7.3 Results and discussion

Figure 7.2 shows the Raman spectrum of CNWs using 532 nm excitation. The peak at 1591 cm^{-1} is the Raman-active G band (E_{2g}) originated from the in-plane vibrational mode. The peak at 1348 cm^{-1} is assigned to the so-called disorder-induced D band, which is activated by a double resonance effect by defects, such as in-plane substitutional hetero-atoms, vacancies, grain boundaries.[5] Beside the G band, a distinct shoulder peak at 1620 cm^{-1} is attributed to D′ band. The D′ band corresponds

to the highest frequency feature in the density of state.[6] Its observation is also associated with the presence of defects in the lattice.[7,8] In the region of the higher order Raman spectrum, three peaks can be observed and attributed to combinational modes: 2689 (2D), 2938 (D+G) and 3219 cm^{-1}(2D′).

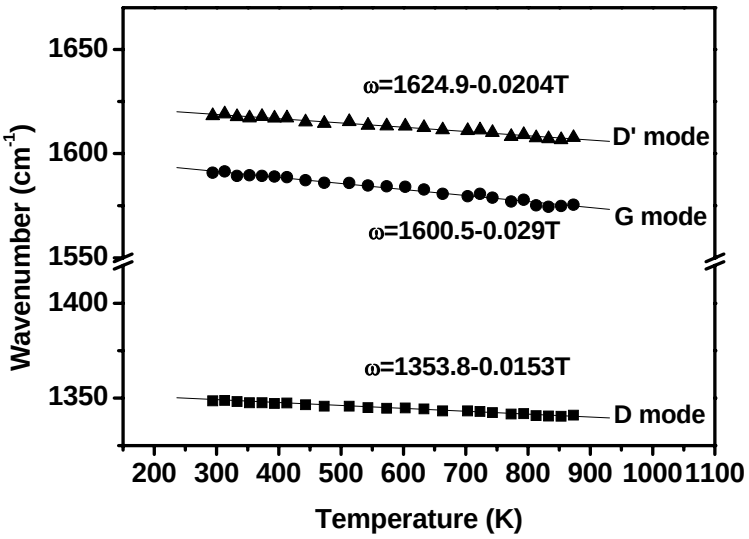

Fig. 7.3 Frequencies of Raman modes (D, G and D′) of CNWs as the temperature increases

For a better understanding of the thermal stability of CNWs, high temperature Raman spectroscopy studies of CNWs were carried out. Figure 7.3 shows the frequencies of Raman peaks of CNWs as the temperature increases. The G mode temperature coefficient of CNWs is 0.029 cm^{-1}/K, which is much bigger compared to that of highly oriented pyrolytic graphite (HOPG, 0.011 cm^{-1}/K).[2] The phonon frequency change at high temperature can be written as:[1,9]

$$\Delta\omega = \left[\frac{d\omega}{dT}\right]_V \Delta T + \left[\frac{d\omega}{dV}\right]_T \left[\frac{dV}{dT}\right]_P \Delta T = \chi_T \Delta T + \chi_V \Delta T$$

The former term describes the pure temperature effect, and latter describes the pure volume effect, which is also known as thermal expansion effect. The pure temperature effect depends on both the anharmonic (third and fourth) terms of the potential and the phonon occupation number *n*. The thermal expansion related frequency change can be expressed as: [1,9]

$$\omega(T) = \omega(0)\exp[-3\gamma\int_0^T \alpha(T)dT]$$

where α(T) is the thermal expansion coefficient and γ is the Grüneisen constant. The thermal expansion effect of HOPG is very weak, because HOPG has a very small thermal expansion coefficient, and also the expansion is almost exclusively along *c* direction, which will not affect the in-plane vibrational G mode.[2] Furthermore, the anharmonic contribution of HOPG and other carbon materials can be ignored, because their Debye temperatures are around 2500 K, which is much higher than the experimental temperature.[2,10] As a result, the 0.011 cm^{-1}/K G mode thermal coefficient of HOPG is mainly attributed to the pure temperature effect due to phonon occupation number. For CNWs, the big difference of 0.029-0.011=0.018cm^{-1}/K probably comes from the thermal expansion effect. Because of the higher amount of defects and impurities, CNWs have smaller crystal domain size. Thus, the crystal planar domains in CNWs expand easier with temperature than those in HOPG, resulting in a more notable temperature effect.[2,11] Similar results have also been reported for carbon (^{12}C) ions implanted graphite (CHOPG) and CNTs, which have G mode frequency coefficients of about 0.028-0.030 cm^{-1}/K.[2,4,12] However, the intrinsic (pure)

temperature effect of CNWs may differ from that of HOPG, which can also contribute to the great difference of the G mode coefficients, further study will be carried out on this part. As also can be seen from Figure 7.3, the D mode and D′ mode have thermal coefficients of 0.015 cm^{-1}/K and 0.020 cm^{-1}/K, respectively. The D mode thermal coefficient of CNWs is quite close to that of DWCNTs (0.015 cm^{-1}/K), but is slightly larger than that of SWCNTs (0.014 cm^{-1}/K).[4]

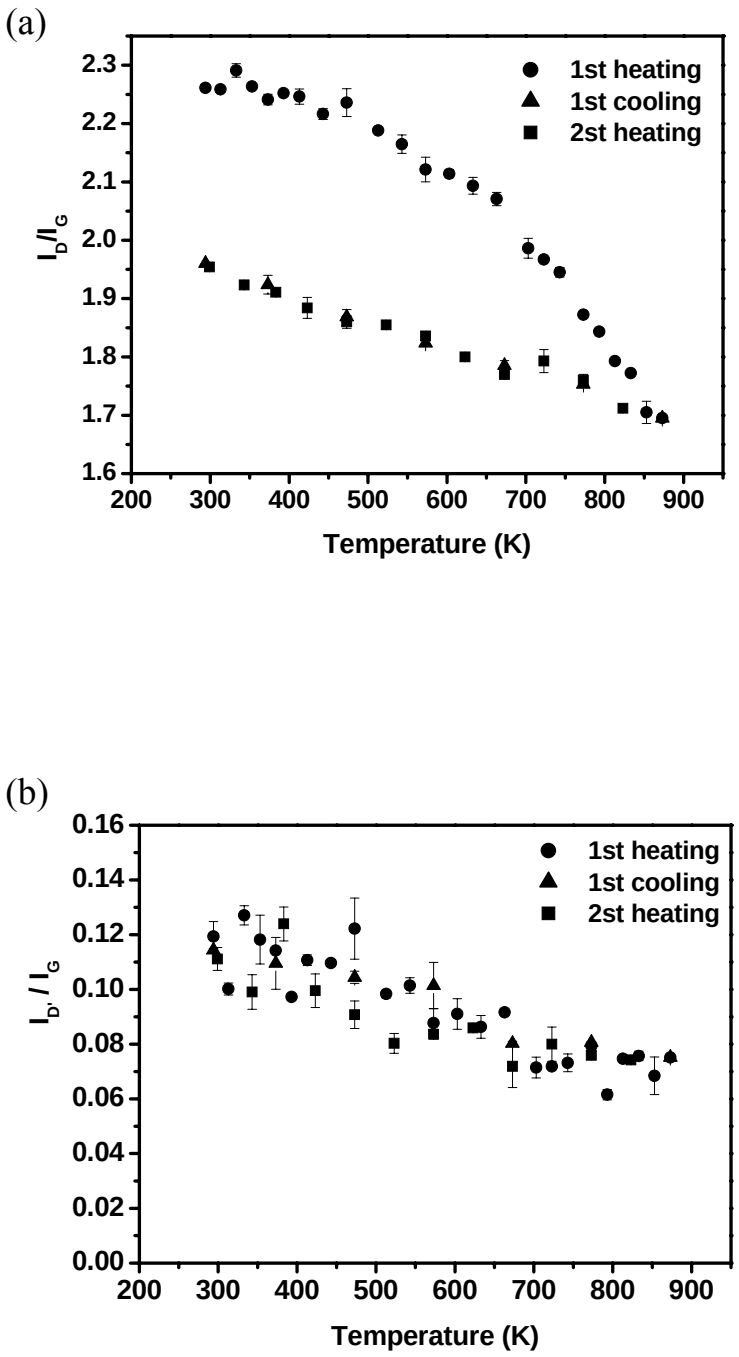

Fig. 7.4 The relative intensity ratio I_D/I_G (a) and $I_{D'}/I_G$ (b) of CNWs at different temperature in the: first heating process, first cooling process and second heating process.

Another focus was how the relative intensity of D mode and G mode (I_D/I_G) changes at high temperature, which is shown in Figure 7.4a. The I_D/I_G is normally used as a measurement of the amount of defects inside carbon materials. This is

because the D mode intensity is proportional to the amount of defects of materials as had been explained by the double resonance theory.[5] In Figure 7.4a, the squares represent the I_D/I_G at each temperature during the heating process. It is obvious that the intensity ratio showed a sub-linear behavior as the temperature increased. After reaching the highest temperature 600 ℃, the sample was cooled down. The circles represent the I_D/I_G at each temperature during the cooling process. The I_D/I_G increased almost linearly as the temperature decreased, indicating that the behaviors of the sample at high temperature were not reversible. After the CNWs were cooled to room temperature, the I_D/I_G ratio of CNWs decreased to 1.95 as compared to 2.3 before anneal. The difference is attributed to the oxidation of surface amorphous carbon during heating. As can be seen from the TEM result (Figure 7.1b), the carbon nanowall sheet was covered by a layer of amorphous carbon. The surface defect caused by amorphous carbon is one kind of defects which contribute to the intensity of D mode. During the heating process, the amorphous carbon was easily oxidized and removed. As a result, the D mode intensity, hence I_D/I_G, decreased upon heating. The amorphous carbon of CNTs can also be removed when the samples are heated in air/oxygen condition at high temperature.[13,14,15] For comparison, we treated CNWs in high vacuum at 600 ℃ for half an hour, the I_D/I_G ratio did not change, which demonstrated that the removal of surface amorphous carbon due to oxidation contributed to the decrease of I_D/I_G in our high temperature experiment under air ambient. For CNWs, the sub-linear decrease of I_D/I_G during the first heating process can be explained by different rate of oxidation of surface amorphous carbon at

different temperatures.

The I_D/I_G increased during the first cooling process, and it decreased reversibly during the second heating process (as shown in Figure 7.4a). This is attributed to the temperature dependence of the double resonance effect of the D mode. At higher temperature, the D mode is in a less resonant condition, so the I_D/I_G ratio is lower. Our previous results in chapter 6 showed that the I_D/I_G ratio of CNWs changes with the excitation laser energy,[16] which was also because of the resonance effect.[17,18] The resonance effect explains well the reversible behavior of the I_D/I_G ratio observed in the second heating process. In the first heating process, both the oxidation of amorphous carbon and resonant effect contributed to the nonlinear decrease of I_D/I_G, with oxidation being the dominating factor. In the cooling process, the effect of surface amorphous oxidation was very weak because the surface amorphous carbon was almost oxidized, so the increase of I_D/I_G was mainly attributed to the resonant effect.

It was worth noting that after the CNWs were heated to 600°C, the D mode intensity decreased only about 20%, while for CNTs, the D mode was completely eliminated at the range of 400°C to 500 °C.[4,13] We conclude that the surface defects caused by amorphous carbon is not the main contributor to the intensity of D mode of CNWs. We take this as a confirmation of the fact that CNWs contain more structural defects than CNTs. The high edge density of CNWs may also contribute to the extremely strong D mode.

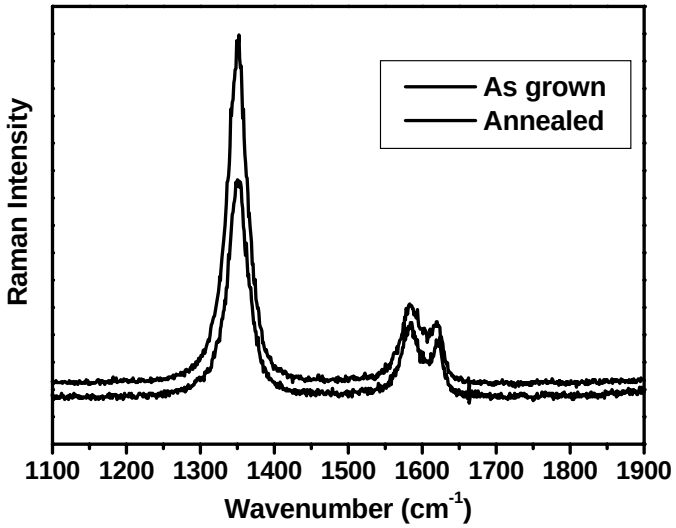

Fig. 7.5 The Raman spectra of CNWs before and after the heating process. The sample was grown with the presence of a small amount of water vapor in the growth chamber, and it had narrow peak width and separated G and D′ mode.

Besides the D mode, the D′ mode is also of interest. The $I_{D'}/I_G$ ratio dependence with temperature is shown in Figure 7.4b. The fitting error of $I_{D'}/I_G$ was much bigger than I_D/I_G because the D′ mode was relatively weak and also overlapped with the G mode. However, we can still see that the $I_{D'}/I_G$ showed a reversible behavior under high temperature, which differed a lot from the result of I_D/I_G. In order to confirm this result, we studied CNWs samples that were grown with the presence of a small amount of water vapor in the growth chamber. The Raman bands were much narrower for such samples, so that the G mode and D′ mode can be easily distinguished. Figure 7.5 shows the Raman spectra before and after anneal at 550 ℃ for 30 min. Noted that the G mode intensity almost unchanged within the experiment error after anneal. We could clearly see that the D′ mode intensity did not show noticeable change relative to

the G mode intensity ($I_{D'}/I_G$ slightly changed from 0.318±0.005 to 0.323±0.005), while the D mode intensity decreased significantly after anneal (I_D/I_G changed from 3.610±0.010 to 3.020±0.010). As mentioned above, both D and D′ modes are defects-related. However, defects affect the two modes differently. While both the intrinsic defects in the crystals and the surface amorphous carbon on the sample surface contribute to the D mode, the D′ mode may be mainly due to the intrinsic defects, because the disappearance of amorphous carbon did not affect the intensity ratio of $I_{D'}/I_G$. This may be the reason that the D′ mode was not easily observed in CNTs, as CNTs have less intrinsic defects.

7.4 Conclusion

In summary, we have demonstrated that the I_D/I_G ratio of CNWs changed from 2.3 to 1.95 after the sample was heated in air ambient to 600 ℃. The reason for the ratio decrease was found to be removal of surface amorphous carbon on the CNWs surface due to oxidation. In addition to the surface amorphous carbon, other causes of the extremely strong D mode of CNWs are the high structural defect density in CNWs and the high density of edges. In contrast to I_D/I_G, the $I_{D'}/I_G$ ratio did not change much after the heating process, implying that the surface amorphous carbon and surface impurity do not contribute as much to the intensity of D′ mode.

7.5 References

[1]. E. S. Zouboulis, M. Grimsditch, *Phys. Rev. B* **1991**, 43, 12490.
[2]. P. H. Tan, Y. M. Deng, Q. Zhao, W. C. Cheng, *Appl. Phys. Lett.* **1999**, 74, 1818.
[3]. L. J. Ci, Z. P. Zhou, L. Song, X. Q. Yan, D. F. Liu, H. J. Yuan, Y. Gao, J. X. Wang, L. F. Liu, W. Y. Zhou, G. Wang, S. S. Xie, *Appl. Phys. Lett.* **2003**, 82, 3098.
[4]. S. Osswald, E. Flahaut, Y. Gogotsi, *Chem. Mater.* **2006**, 18, 1525.
[5]. C. Thomsen, S. Reich, *Phys. Rev. Lett.* **2000**, 85, 5214.
[6]. R. J. Nemanich, S. A. Solin, *Phys. Rev. B* **1979**, 20, 392.
[7]. R. Saito, A. Joria, A. G. SouzaFilho, G. Dresselhaus, M. S. Dresselhaus, M. A. Pimenta, *Phys. Rev. Lett.* **2002**, 88, 027401.
[8]. E. B. Barros, N. S. Demir, A. G. SouzaFilho, J. MendesFilho, A. Jorio, G. Dresselhaus, M. S. Dresselhaus, *Phys. Rev. B* **2005**, 71, 165422.
[9]. C. Postmus, J. R. Ferraro, S. S. Mitra, *Phys. Rev.* **1968**, 174, 983.
[10]. W. J. Borer, S. S. Mitra, K. V. Namjoshi, *Solid State Commun.* **1971**, 9, 1377.
[11]. J. Heremans, I. Rahim, M. S. Dresselhaus, *Phys. Rev. B* **1985**, 32, 6742.
[12]. A. M. Rao, E. Richter, S. Bandow, B. Chase, P. C. Eklund, K. A. Williams, S. Fang, K. R. Subbaswamy, M. Menon, A. Thess, R. E. Smalley, G. Dresselhaus, M. S. Dresselhaus, *Science* **1997**, 275, 5297.
[13]. S. Osswald, E. Flahaut, H. Ye, Y. Gogotsi, *Chem. Phys. Lett.* **2005**, **402**, 422.
[14]. N. E. Tran, S. G. Lambrakos, *Nanotechnology* **2005**, 16, 639.
[15]. E. Borowiak-Palen, T. Pichler, X. Liu, M. Knupfer, A. Graff, O. Jost, W. Pompe, R. J. Kalenczuk, J. Fink, *Chem. Phys. Lett.* **2002**, 363, 567.
[16]. Z. H. Ni, H. M. Fan, Y. P. Feng, Z. X. Shen, B. J. Yang, Y. H. Wu, *J. Chem. Phys.* **2006**, 124, 204703.
[17]. Y. Wang, D. C. Alsmeyer, R. L. McCreery, *Chem. Mater.* **1990**, 2, 557.
[18]. T. P. Mernagh, R. P. Cooney, R. A. Hohnson, *Carbon* **1984**, 22, 39.

Chapter 8

High Pressure Raman and Photoluminescence studies of ZnCdSe Quantum Dots

8.1 Introduction

Ⅱ-Ⅵ wide band-gap semiconductors, (such as CdSe, ZnSe,) have attracted much attention in the past decade. Their optical properties make them suitable for visible light emitting diodes (LEDs), lasers, and other optoelectronic devices.[1,2] The alloy $Zn_xCd_{1-x}Se$ is also a very important semiconductor, its compositional dependent band-gap can be tuned to cover the entire visible range. Recently, different nanostructured $Zn_xCd_{1-x}Se$ have also been synthesized, such as $Zn_xCd_{1-x}Se$ quantum well, nanowires, nanorods, and QDs.[3-7] The nanoscale structures bring out new properties. High-quality $Zn_xCd_{1-x}Se$ QDs have been successfully prepared by the high temperature solution method.[7] These alloy QDs show high PL efficiency (70-85%) and narrow band width (22-30nm), which are comparable to the best reported CdSe-based QDs. The $Zn_xCd_{1-x}Se$ QDs can be very promising nanomaterial for applications as biological labels and short wavelength optoelectronic devices such as quantum dot lasers and photovoltaic cells.[7]

As is well known, the stability of QDs is not only essential issue for understanding their fundamental physical process related to emission and Raman scattering, but is also vital to their applications. The alloy $Zn_xCd_{1-x}Se$ QDs have been

demonstrated higher thermal and chemical stability due to its larger particle size, high crystallinity and "hardened" lattice structure, compared with bare CdSe QDs. However, the structural stability of such alloy QDs is little known.

High pressure PL and Raman spectroscopy are the popular way to study the electronic structure and phase transition of semiconductor materials related to their structural stability. Tolbert and Alivisatos have reported the pressure induced wurtzite to rock-salt structural transformation in CdSe QDs.[8,9] They showed that both the thermodynamics and kinetics of this transformation were strongly altered in QDs due to its small size and high surface energy. For the alloy materials, three phase transitions were observed by Arora *et al*. on $Zn_{1-x}Mn_xSe$ under pressure.[10,11] It seems that the alloy sample may behave in a more complicated manner than binary structures (like CdSe) under high pressure. Li *et al.* performed micro-Raman and PL investigation on $Zn_xCd_{1-x}Se$ films (x=0.68) and quantum wells (x=0.74) under high pressure.[12,13] They reported the pressure coefficients of the materials, but did not observe any phase transition up to 66 kbar. Camacho *et al.* also studied the pressure dependence of optical phonons in zinc-blende ZnCdSe films (x=0.5 and 0.6) at low temperature.[14] They did not observe any phase transition up to 75 kbar either. Up to now, no high pressure Raman and PL experiments have been reported on ZnCdSe QDs.

In this chapter, we performed the high pressure Raman and PL experiments on the wurtzite $Zn_xCd_{1-x}Se$ (x=0.2) QDs up to 130 kbar. Two structural phase transitions were observed and discussed: a new unidentified structural phase transition at 25.8

kbar and a wurtzite to rock-salt structural phase transition at 71 kbar. The experimental results of ZnCdSe QDs show significant difference from that of bare CdSe or ZnSe QDs as well as the corresponding bulk materials.

8.2 Experimental

8.2.1 Introduction of diamond anvil cell

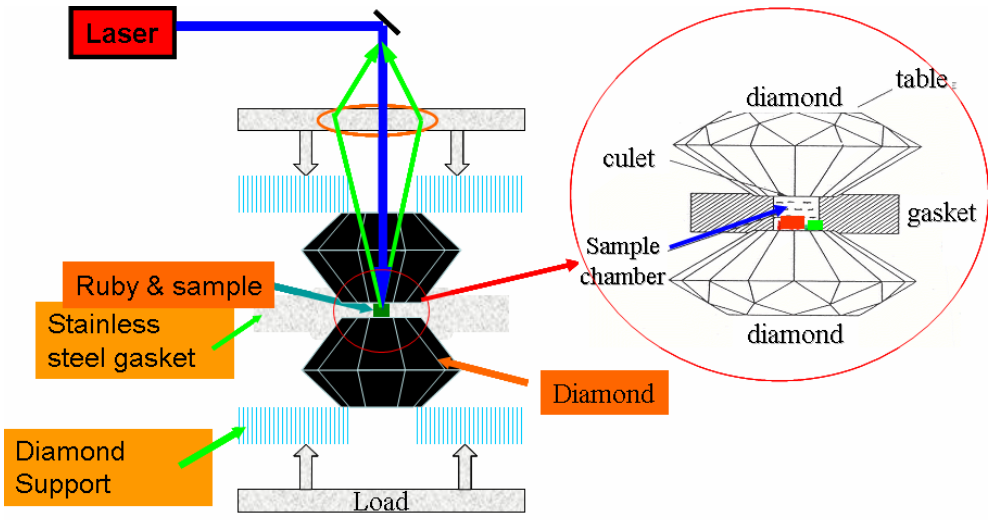

Figure 8.1 Schematic of Diamond Anvil Cell (DAC)

Diamond anvil cells (DAC) are commonly used for the generation of very high pressures.[15-19] The basic principle of the DAC is that when a metal gasket is compressed between the small flat faces of two brilliant cut gem quality diamonds set in a opposed anvil configuration, very high pressure is generated in the gasket hole, which is usually filled with a pressure transmitting medium and samples.

Fig. 8.1 illustrates the compact Bassett cell used in our experiment, which has a threaded gland to apply force on the diamond anvils. The stainless-steel block

comprising the main body of the DAC has suitable apertures for the stationary piston and the sliding one, and the latter is held by a key in a slot to prevent it from rotation. The rockers provide translational motion for pressing the gasket between the upper and lower diamonds. In DAC, the window material is diamond, which serves the dual purpose of transmitting the pressure and being transparent to the laser and Raman signal.

8.2.2 Experimental detail

High-quality $Zn_xCd_{1-x}Se$ QDs were successfully prepared at high temperature by incorporating stoichiometric amounts of Zn and Se into pre-prepared CdSe QDs,[7] and the size of the $Zn_xCd_{1-x}Se$ (x~0.2) QDs was ~4.7 nm as shown by transmission electron microscopy (TEM) image inserted in Fig. 8.2a. Energy-dispersive x-ray analysis (EDX) shows that the mole ratio of zinc: cadmium: selenium is 9.8 : 40 : 50.2, so the zinc composition is around x=0.2. X-ray diffraction (XRD) results reveal that the $Zn_xCd_{1-x}Se$ QDs (x~0.2) are hexagonal wurtzite structure.[7] High pressure was generated by a diamond anvil cell (DAC), with 4:1 methanol–ethanol mixture as pressure medium. A small piece of sample was loaded into a gasket with a hole of ~ 250 μm in diameter and of ~ 100μm in thickness. Pressure was calibrated by the energy shift of the R_1 luminescence line of a ruby crystal. The R_1 line (694.2nm) from ruby is quite strong and sharp and its peak shift is almost linear up with pressure to 300 kbar. The pressure coefficient is 0.365 Å $kbar^{-1}$ or 0.753 cm^{-1} $kbar^{-1}$. The micro-Raman and PL measurements were carried out with a Renishaw inVia Raman system using a 532nm DPSSL laser.

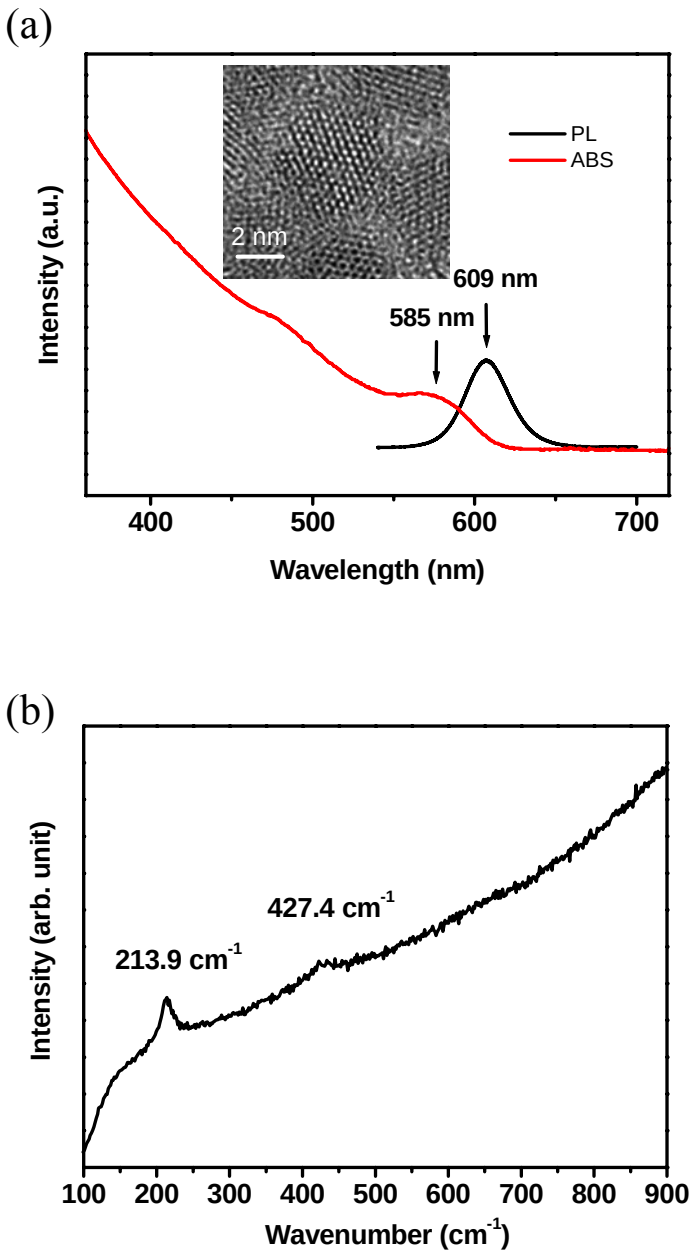

Fig. 8.2 PL (a) and Raman (b) spectra of $Zn_xCd_{1-x}Se$ (x=0.2) QDs at ambient pressure excited by using 532nm laser line.

8.3 Results and Discussion

Fig. 8.2a shows the absorption and PL spectrum of $Zn_xCd_{1-x}Se$ (x=0.2) QDs at ambient pressure. The absorption band of $Zn_xCd_{1-x}Se$ (x=0.2) QDs is around 2.12 eV, which is blueshifted compared to that of corresponding bulk material with the same zinc composition (1.83 eV)[20] due to the quantum confinement effect. The PL spectrum was excited by 532 nm laser line. The band edge emission is at about 2.04 eV (609nm). The PL peak at 609 nm is quite symmetrical and has a full width at half maximum (FWHM) of about 30nm, indicating that the sample is of high quality, with a narrow distribution in the size of QDs.

Fig. 8.2b shows the Raman spectrum of $Zn_xCd_{1-x}Se$ (x=0.2) QDs at ambient pressure. There are two peaks in the spectrum; the stronger one at 213.9 cm^{-1} is the A_1 longitudinal-optical (LO) mode of the alloy QDs, while the weaker peak at 427.4 cm^{-1} is the overtone of LO mode, which is exactly twice the frequency of the LO mode. The sharp drop at about 150 cm^{-1} is caused by the notch filter and the upward slope background is caused by the strong broad photoluminescence, whose maximum is located at about 600nm, as shown in Fig. 8.2a. The FWHM of the LO peak is about 26 cm^{-1}. Compare to the ZnCdSe bulk materials with similar Zn composition (FWHM ~8 cm^{-1}, peak position ~219 cm^{-1}),[21] the LO mode of ZnCdSe QDs shifts to lower frequency and becomes broader. These are due to small physical dimensions of the QDs which leads to the breakdown of q=0 selection rule of phonon dispersion, causing the first order Raman line to shift and broaden.[22]

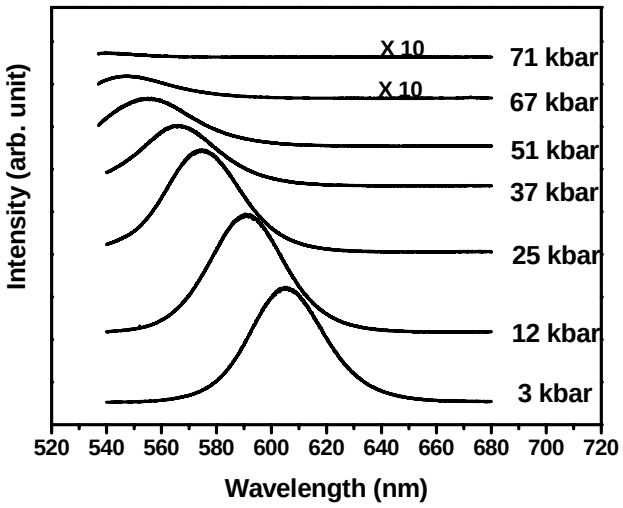

Fig. 8.3a PL spectra taken from $Zn_xCd_{1-x}Se$ (x=0.2) quantum dots under high pressure at room temperature. Above 71 kbar, the PL peak can not be observed because of phase transition.

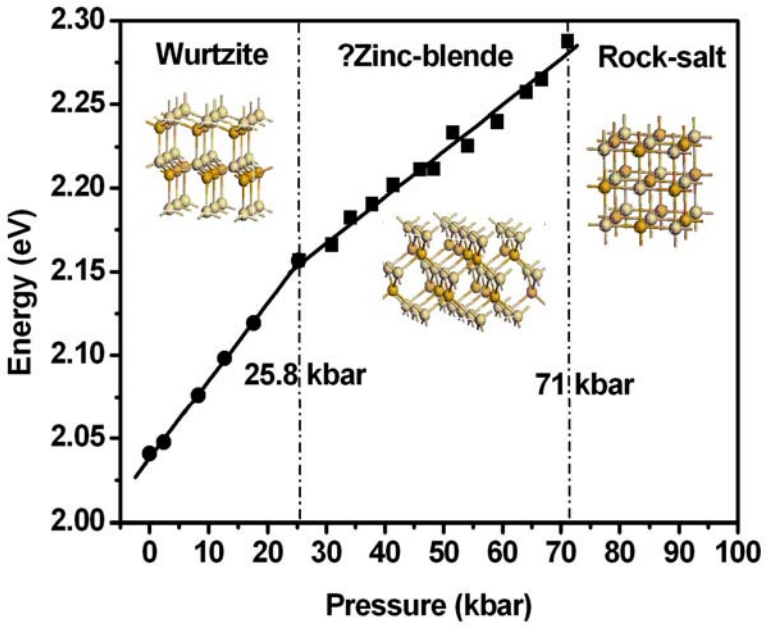

Fig. 8.3b PL peak energy of $Zn_xCd_{1-x}Se$ (x=0.2) QDs as a function of pressure. At 25.8 kbar, the pressure coefficient changed from 4.64 meV/kbar to 2.76 meV/kbar

Next, we studied the Raman and PL of $Zn_xCd_{1-x}Se$ (x=0.2) QDs under pressure. Fig. 8.3a shows the PL spectra with increasing pressure. A large blue shift of the PL peak was observed due to the pressure induced blue shift of bandgap energy. Above the pressure of 71 kbar, the PL peak disappeared, indicating that the QDs undergo a phase transition from a direct-band-gap wurtzite structure to an indirect-band-gap rock-salt structure, which will cause the annihilation of PL emission. We also repeated the high pressure PL experiment using 488nm excitation laser. The results were quite similar to those of using 532nm excitation laser. Most of wurtzite/zinc-blende semiconductors (including CdSe and ZnSe) have this kind of phase transition under high pressure and this phase transition was observed in corresponding nanoscale semiconductor too.[8,23,24] Here the phase transition pressure of $Zn_xCd_{1-x}Se$ QDs (71 kbar) is higher than that of CdSe (20 to 49 kbar)[8,23,24] and lower than that of ZnSe (95 to 130 kbar) with various size.[24] Moreover, phase transition to rocksalt structure of $Zn_{0.5}Cd_{0.5}Se$,which has higher zinc composition than our sample, has not been observed up to the pressure of 75 kbar.[14] Apparently for $Zn_xCd_{1-x}Se$ alloy, the pressure of wurtzite/zinc-blende to rock-salt phase transition increases as the zinc composition increases.

The PL energy as a function of pressure is shown in Fig. 8.3b. We fitted the data with the following formula:

$$E_P = E_0 + \alpha P$$

where E_0 is the ambient pressure PL energy, α is the PL pressure coefficient, and P is the applied hydrostatic pressure in kbar. It was found that at lower pressure, the PL

energy of $Zn_xCd_{1-x}Se$ (x=0.2) QDs shifted linearly with a pressure coefficient of 4.64 meV/kbar. However, above 25.8 kbar, the pressure coefficient changed to 2.76 meV/kbar, and the PL peak also shifted quite linearly with pressure. Obviously there is an electronic structure change at this critical pressure, which may be due to an unidentified structural transition induced by pressure.

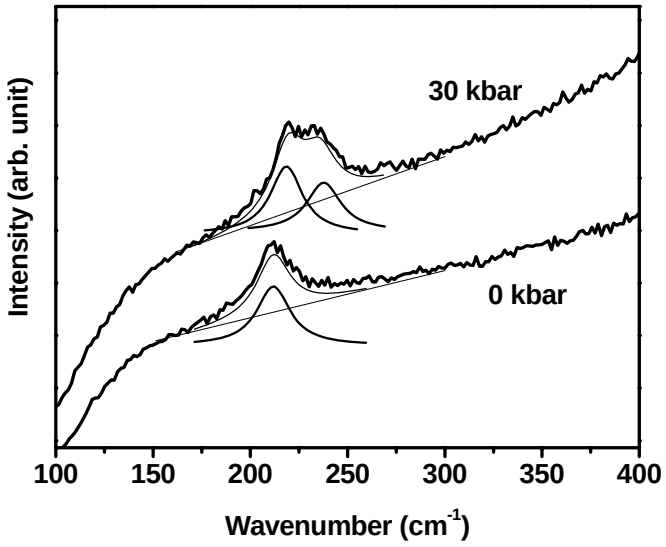

Fig. 8.4a Raman spectra of $Zn_xCd_{1-x}Se$ (x=0.2) QDs at pressure of 0 kbar and 30 kbar. The smooth solid curves are the lorentzian fitting of the peaks.

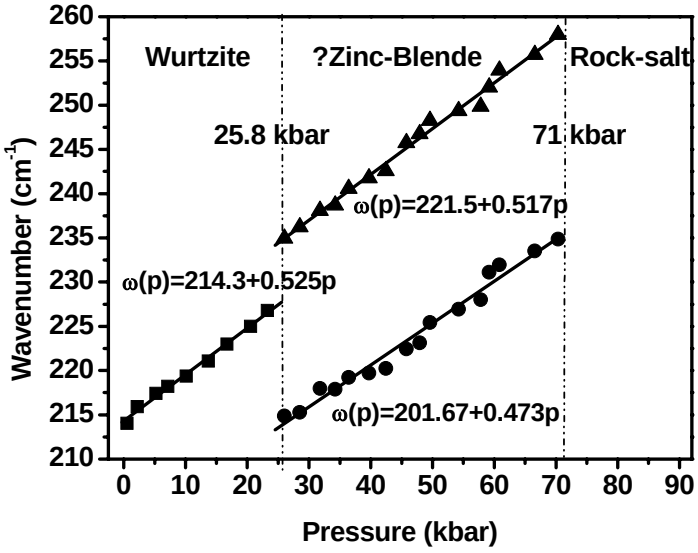

Fig.8.4b Raman shift of LO mode of $Zn_xCd_{1-x}Se$ (x=0.2) QDs as a function of pressure. After 25.8 kbar, a peak splitting was observed. Above 71 kbar, the Raman peaks can not be observed because of the semiconductor-metal phase transition.

High pressure Raman spectroscopy of ZnCdSe alloy QDs were also carried out. Below 71 kbars, the Raman LO mode shifted to higher frequencies with pressure. The LO peak disappeared at 71 kbars, the same pressure at which the PL disappears. The disappearance of LO mode is also attributed to the wurtzite to rocksalt phase transition as Raman scattering of the rocksalt phase is inactive. In order to study the possible structural phase transition at 25.8 kbar, the Raman spectra of ZnCdSe QDs before and after 25.8 kbar were compared. Fig. 8.4a shows the Raman spectra at 0 kbar and 30 kbar, in which a peak splitting is clearly observed. By fitting all the Raman spectra at different pressure, we find that the peak splitting also began at 25.8 kbar. Fig. 8.4b shows the Raman peak position of the LO peak as a function of pressure. The pressure coefficient of the LO mode before 25.8kbar was about 0.525 cm^{-1}/kbar, with a linear fit of $\omega = 214.3\ cm^{-1} + 0.525\ P\ cm^{-1}$/kbar. After splitting, the higher frequency peak has a pressure coefficient of 0.517 cm^{-1}/kbar, with a linear fit of $\omega = 221.5\ cm^{-1} + 0.517\ P\ cm^{-1}$/kbar; and the lower frequency peak has the coefficient of 0.473 cm^{-1}/kbar, with a linear fit of $\omega = 201.67\ cm^{-1} + 0.473\ P\ cm^{-1}$/kbar. The Raman LO mode splitting as well as the PL pressure coefficient sudden change at the same pressure (25.8 Kbar) indicates that there is a new structural phase transition. This phase transition has not been observed in bulk $Zn_xCd_{1-x}Se$ as well as bulk or nanoscaled CdSe and ZnSe.

As we know, for the Ⅱ-Ⅵ semiconductor (such as CdSe), there are two stable structures at ambient condition, which are wurtzite and zinc-blende, or sometimes the mixture of these two structures. Under high pressure, the wurtzite or zinc-blende

structured Ⅱ-Ⅵ semiconductors have their first-order phase transition to rocksalt structure, then may undergo phase transition to intermediate structures, such as cinnabar and Cmcm, followed by the CsCl structure at around 940 kbar.[25-28] The structure of our ZnCdSe QDs at ambient condition is wurtzite, while at 25.8 kbar, it went through an unidentified phase transition. The observed new transition is below that of wurtzite to rock-salt phase transition at 71 kbar, which is confirmed by the disappearance of both Raman and PL intensity. The structure between 25.8 kbar could not be cinnabar or cmcm either, as the energies of these two structures are usually similar or higher than rocksalt,[21] and they are also indirect bandgap structures without PL.

A possible structure would be zinc-blende. Zinc-blende is a direct bandgap structure, which has a strong PL just like wurtzite. This is consistent with our results that the PL signals between 25.8 and 71 kbar were still strong. By the way, although it is well known that wurtzite and zinc-blende have very similar energy, the wurtzite to zinc-blende phase transition has been observed on ZnS by Pan *et al.* [29] on nanocrystalline and Wang et al. [30] on nanobelts with high pressure synchrontron x-ray diffraction experiments. As is well known, at ambient pressure, the bulk ZnCdSe alloy has a phase transition from wurtzite to zinc-blende by increasing the zinc composition. The critical composition for wurtzite to zinc-blende transition in bulk $Zn_xCd_{1-x}Se$ is at x=0.5 to 0.7.[31] Different zinc compositions result in different structures, implying that wurtzite to zinc-blende phase transition is a smooth transition that can easily happen for $Zn_xCd_{1-x}Se$ alloy. Noted that if the QDs were in zinc-blende phase between 25.8

and 71 kbar, the deduced bandgap of the zinc-blende structure at ambient pressure will be 2.08 eV, which is higher than that of wurtzite structure (2.04 eV). This is inconsistent with the fact that bandgap of wurtzite semiconductor is normally higher than zinc-blende, mainly because of the more ionic character of the wurtzite structure.[32] However, the small difference (~0.04 eV) could be caused by the different positions of the elements in the two structures, or the QDs size changing during the phase transition. Besides zinc-blende, there may also be other possible explanations for the new phase transition, such as a new high pressure structure, and a tilted wurtzite structure. Further high pressure x-ray diffraction experiment is necessary to confirm this conclusion

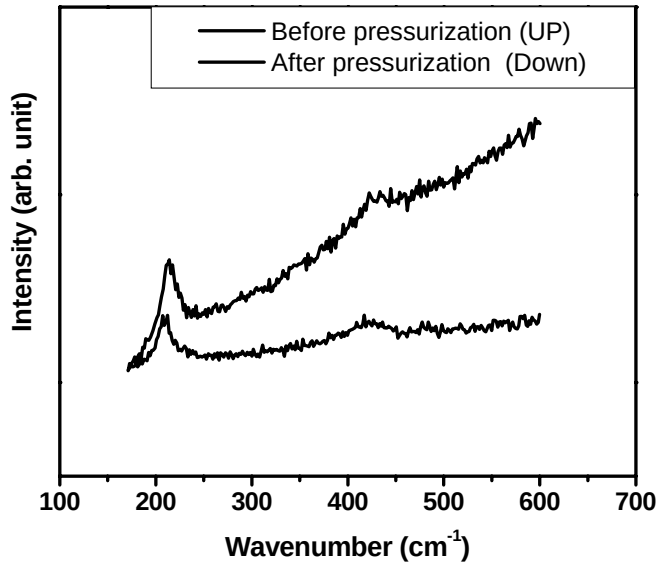

Fig. 8.5a Raman spectra of $Zn_xCd_{1-x}Se$ (x=0.2) QDs before and after applying the pressure.

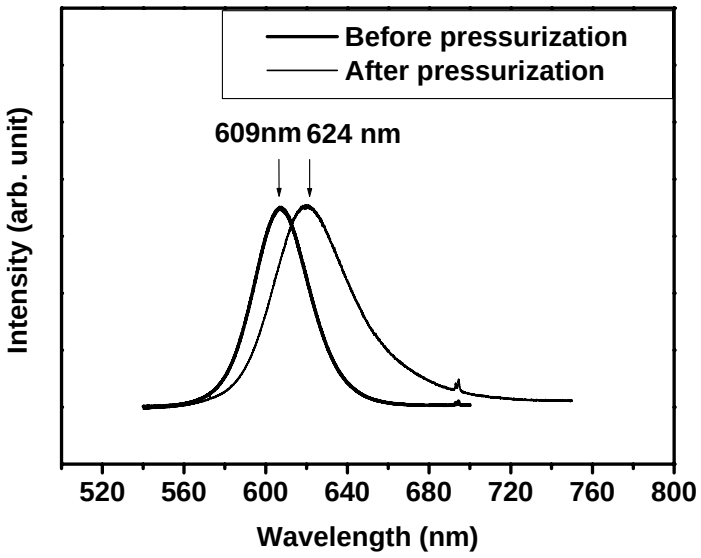

Fig. 8.5b PL spectra of $Zn_xCd_{1-x}Se$ (x=0.2) QDs before and after applying the pressure.

At pressure downstroke, the Raman and PL peaks can be observed at 22 kbar and below. The splitting Raman LO modes recovered to one peak, which means that the QDs transform directly from rock-salt back to wurtzite structure. The wurtzite to rocksalt phase transition of ZnCdSe alloy QDs has a hysteresis of about 71-22=49 kbar, which is comparable to the broad hysteresis of CdSe QDs (around 50 kbar).[8] After releasing the pressure, the recovered LO Raman peak position is about 210 cm^{-1}, which is 4 cm^{-1} lower than peak position before the pressure was applied, as shown in Fig. 8.5a. Besides that, the PL peak becomes asymmetric with a tail to the low energy side, as shown in Fig. 8.5b. The main PL peak energy is at ~1.99 eV, which is 0.05 eV lower than peak energy before the application of pressure. The red shift of Raman peak can not be caused by the smaller size of dots through the phase transition,[9] because smaller size QDs will accompany with higher electronic transition energy, hence the blue shift of PL,[33,34] which is not accordant with our result. Both red shifts in Raman frequency and PL energy were caused by lattice defects that formed under the pressure and phase transition, which will cause the shrinkage of the band-gap, these phenomena were also observed on high pressure phase transition of CdS.[35] The asymmetry of the recovered PL peak may be due to the increased emission of surface states, which are formed by the rearrangement of surface during the phase transition.[9]

8.4 Conclusion

In Summary, Raman and PL experiments have been carried out on $Zn_xCd_{1-x}Se$ (x=0.2) QDs under hydrostatic pressure up to 130 kbar at room temperature. Two structural transitions were observed in the pressure range. The wurtzite to rock-salt was observed at about 71 kbar, indicated by the disappearance of PL and Raman peaks. A new unidentified phase transition was also observed at about 25.8 kbar. At this pressure, the PL coefficient has a sudden change from 4.64 meV/kbar to 2.76 meV/kbar, and also a split in Raman peak was observed. The new phase transition was probably a wurtzite to zinc-blende phase transition. These results for ZnCdSe QDs show significant difference from that of bulk ZnCdSe as well as CdSe and ZnSe QDs, implying that the quantum size effect plays an important role in the structure stability of the alloy QDs.

8.5 References

[1] V. I. Klimov, A. A. Mikhailovsky, S. Xu, A. Malko, J. A. Hollingsworth, C. A. Leatherdale, H. J. Eisler, and M. G. Bawendi, Science **2000**, 290, 314.

[2] S. Coe, W. K. Woo, M. Bawendi, and V. Bulovic, Nature **2002**, 420, 800.

[3] N. Matsumura, K. Yasui, and J. Saraie, J. Crys. Grow. **2002**, 237, 1536.

[4] X. T. Zhang, Z. Liu, Q. Li, and S. K. Hark, J. Phys. Chem. B **2005**, 109, 17913.

[5] H. Lee, P. H. Holloway, and H. Yang, J. Chem. Phys. **2006**, 125, 164711.

[6] R. Venugopal, P. I. Lin, and Y. T. Chen, J. Phys. Chem. B **2006**, 110, 11691.

[7] X. H. Zhong, M. Y. Han, Z. L. Dong, Timothy J White, and W. Knoll, J. Am. Chem. Soc. **2003**, 125, 8589.

[8] S. H. Tolbert, A. P. Alivisatos, Science **1994**, 265, 373.

[9] S. H. Tolbert, A. P. Alivisatos, J. Chem. Phys. **1995**, 102, 4642.

[10] Akhilesh K. Arora and T. Sakuntala, Phys. Rev. B **1995**, 52, 11052.

[11] Akhilesh K. Arora, E. K. Suh, U.Debska, and A. K. Ramdas, Phys. Rev. B **1988**, 37, 2927.

[12] W. S. Li, Z. X. Shen, D. Z. Shen, and X. W. Fan, J. Appl. Phys. **1998**, 84, 5198.

[13] W. S. Li, Y. B. Chi, Y. M. Li, X. W. Fan, B. J. Yang, D. Z. Shen, and Y. M. Lu, Thin Solid Films **1995**, 266, 307.

[14] J. Camacho, I. Loa, A. Cantarero, K. Syassen, I. Hernandez-Calderon, and L. Gonzalez, Phys. Stat. Sol. (B) **2003**, 235, 432.

[15] A. Jayaraman, Rev. Mod. Phys., Vol. **1983**, 55, 65.

[16] G. J. Piermarini, S. Block, J. D. Barnett, J. Appl. Phys. **1973**, 44, 5377.

[17] C. Carlone, N. K. Hota, H. J. Stolz, M. Elbert and H. D. Hochheimer, J. Chem. Phys. **1981**, 75, 3220.

[18] R. A. Forman, G. J. Piermarini, J. D. Barnett, and S. Block, Science **1972**, 176, 284.

[19] J. D. Barnett, S. Block, and G. J. Piermarini, Rev. Sci. Instrum. **1973**, 44, 1.

[20] Y. D. Kim, M. V. Klein, S. F. Ren, and Y. C. Chang, Phys. Rev. B **1994**, 49, 7262.

[21] O. Brafman, Solid State Comm. **1972**, 11, 447.

[22] K. L. Teo, S. H. Kwok, P. Y. Yu, and Soumyendu Guba, Phys. Rev. B **2000**, 62, 1584.

[23] W. Shan, W. Walukiewicz, J. W. Ager III, K. M. Yu, J. Wu, and E. E. Haller, Appl. Phys. Lett. **2004**, 84, 67.

[24] A. Mujica, A. Rubio, A. Munoz, R. J. Needs, Rev. Mod. Phys. **2003**, 75, 863.

[25] O. Zakharov, A. Rubio andM. L. Cohen, Phys. Rev. B **1995**, 51, 4926.

[26] M. Côté, O. Zakharov, A. Rubio, and M. L. Cohen, Phys. Rev. B **1997**, 55, 13025.

[27] R. J. Nelmes, M. I. Mcmahon, Semicond. Semimetals **1998**, 54, 145.

[28] H. M. Fan, Z. H, Ni, Y. P. Feng, X. F. Fan, J. L. Kuo, Z. X. Shen, and B. S. Zou, Appl. Phys. Lett. **2007**, 90, 021921.

[29] Y. W. Pan, S. C. Qu, S. S. Dong, Q. L. Cui, W. W. Zhang, X. Z. Liu, J. Liu, B. B.

Liu, C. X. Gao, and G. T. Zou, J. Phys. : Condens. Matter **2002**, 14, 10487.
[30] Z. W. Wang, L. L. Daemen, Y. S. Zhao, C. S. Zha, R. T. Downs, X. D. Wang, Z. L. Wang, R. J. Hemley, Nature Materials **2005**, 4, 922.
[31] A. S. Nasibov, Y. V. Korostelin, P. V. Shapkin, L. G. Suslina, D. L. Fedorov, L. S. Markov, Solid State Comm. **1989**, 71, 867.
[32] C. Y. Yeh, S. H. Wei, and A. Zunger, Phys. Rev. B **1994**, 50, 2715.
[33] T. Vossmeyer, L. Katsikas, M. Giersig, I. G. Popovic, K. Diesner, A. Chemseddine, A. Eychmüller, and H. Weller, J. Phys. Chem. 1994, 98, 7665.
[34] A. P. Alivisatos, Science **1996**, 271, 933.
[35] X. S. Zhao, J. Schroeder, T. G. Bilodeau, and L. G. Hwa, Phys. Rev. B **1989**, 40, 1257.

Chapter 9

High Pressure Raman and Photoluminescence Investigations of CdSe/ZnS core/shell Quantum Dots

9.1 Introduction

Highly luminescent CdSe/ZnS core/shell semiconductor quantum dots (QDs) have attracted much attention because of their applications in optoelectronics,[1] nonlinear optics,[2] and biology.[3] The epitaxial ZnS shell around the CdSe core can strongly improve ODs' photoluminescence (PL) efficiency, as well as chemical and thermal stability. Though the role of the ZnS shell has been intensively discussed,[4] the influence of the ZnS shell on structural transformation and correlative electronic state properties is little known so far. One way to explore the electronic state and structure phase stability of semiconductor QDs is to apply hydrostatic pressure. Under pressure, solid-solid phase transitions from wurtzite to rock salt have been observed in CdSe QDs.[5,6] Difference from the bulk materials, size-dependent phase transition properties reveal that the surface of QDs plays a dominant role in the relative stability of the phases of such system as well as the electronic state structure.[6] Thus the reconstructed surface by the inorganic ZnS directly relates to the structural stability of QDs. The CdSe/ZnS QDs with "hard" shell are desired to offer significant differences in the kinetics and the mechanism of the phase transitions under pressure from those of organic-stablilized CdSe QDs. Therefore, it is crucial to investigate pressure induced phase transition and electronic state properties of CdSe/ZnS core/shell QDs to gain

further insight into the effects of ZnS shell.

Methods on high pressure studies of QDs have been developed in past decades. Tolbert and Alivisatos have reported their studies on size-dependent phase transition of CdSe QDs using high pressure x-ray diffraction and optical absorption.[5,6] The pressure-induced photoluminescence (PL) of CdSe QDs were measured to determine the electron-phonon coupling in these dimensionally restricted materials.[7] High-pressure experiments for the resistance measurement of PbS[8] and $CoFe_2O_4$[9] nanocrystals were also reported. Among those mentioned above, Raman scattering and PL are popular techniques for the determination of phase transition and electronic state information under high pressure.

In this chapter, we performed PL and Raman spectroscopic studies of CdSe/ZnS core/shell QDs under the pressure up to 160 kbar. Two phase transitions were observed in whole pressure range. An unidentified high-pressure phase of CdSe/ZnS QDs above 79 kbar is observed and discussed. The full width at half maximum (FWHM) of the PL peak was found to anomalously decrease with pressure. These behaviors are quite different from that observed for CdSe QDs and bulk CdSe. We attribute these differences to the effect of the reconstructed surface by the ZnS shell.

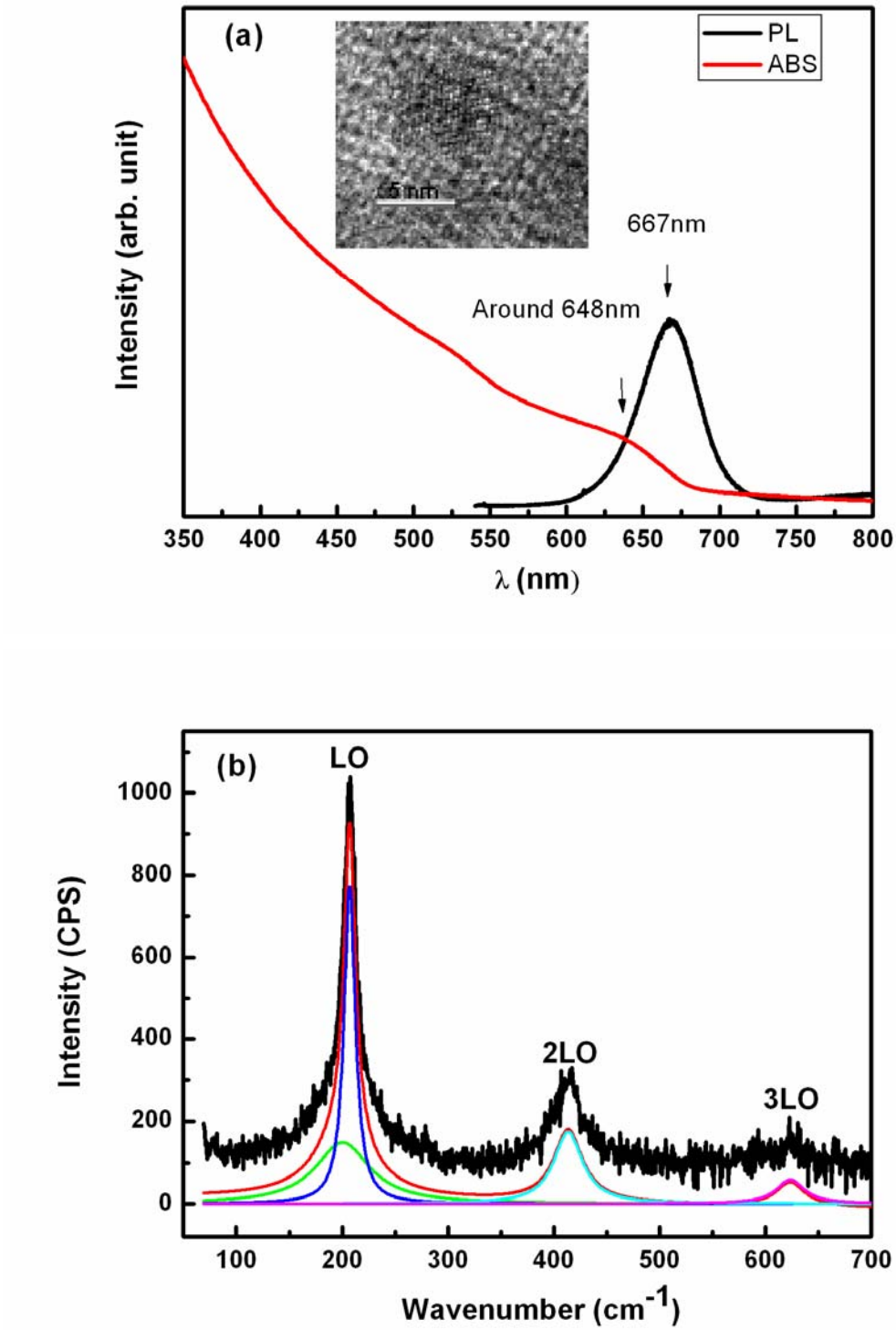

Fig. 9.1 (a) Absorption and PL spectra of CdSe/ZnS QDs. The inset shows the TEM image. (b) Raman spectrum of CdSe/ZnS QDs excited with the 488 nm line from an Ar^+ laser, after subtraction of the PL background.

9.2 Experimental

The CdSe/ZnS QDs were prepared by an organometallic synthetic approach.[10] The thickness of the ZnS shell is estimated to be about 2-3 monolayer; and the ZnS overcoated CdSe QDs obtained by this method exhibit a high quantum efficiency (above 50%) at room temperature, as well as a narrow size distribution (<5%). Absorption spectra were measured by a UV-Visible spectrophotometer (Shimadzu, UV-1700) at room temperature, with the sample dispersed in toluene solution. As shown in Fig. 9.1(a), the absorption band of CdSe/ZnS QDs is around 1.91 eV which is blue-shift compared to that of the corresponding bulk material (1.7eV) due to the quantum size effect. The band edge emission at ambient conditions is 1.85eV. By comparing our results with the absorption band and PL of different-sized CdSe ODs,[6,7,10] we conclude that the size of our CdSe/ZnS QDs is about 5.4 nm. This is in agreement with the estimation from the TEM image (~5.6 nm) inserted in Fig. 9.1(a).

In order to estimate the thickness of the ZnS shell by comparing with Baranov's results,[11] we measured the Raman spectrum of CdSe/ZnS ODs at ambient conditions using a 488 nm Ar^+ laser as the excitation source. As shown in Fig. 9.1(b), all three peaks were assigned to the longitudinal optical (LO) phonon and its overtone phonons of wurtzite structure CdSe core. No peak originated from the ZnS composite was observed. A good fit for the observed LO peaks was obtained by taking the sum of two Lorentzian functions. The peak positions and widths of LO (206.6 cm^{-1}) and surface optical mode (200.4 cm^{-1}) are comparable to those of the CdSe QDs with

0.5-2.2 monolayer ZnS shell. These results agree well with our estimated thickness of the ZnS shell.

Detail of high pressure experiment is the same as described in Chapter 8.

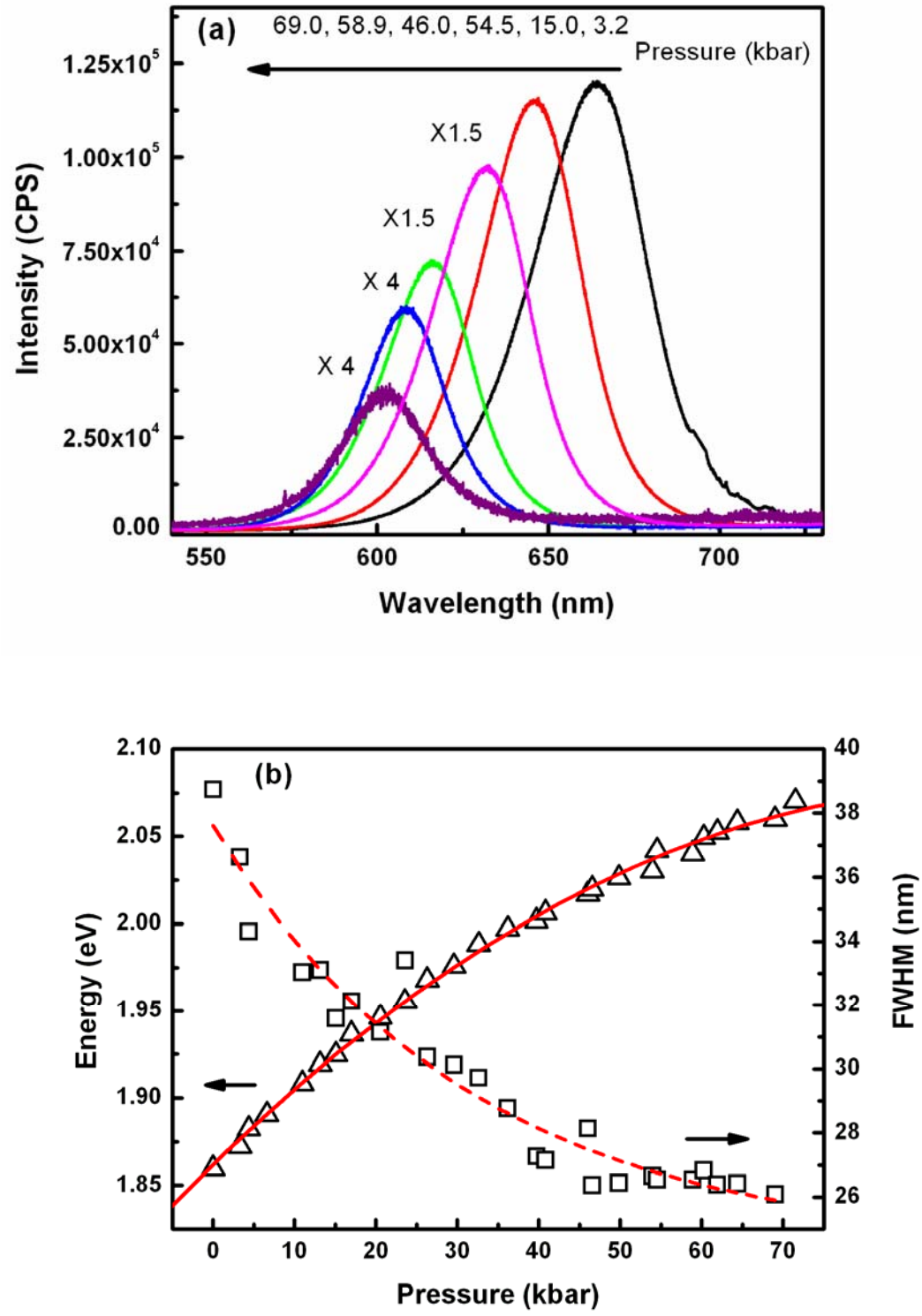

Fig. 9.2. Pressure dependence of PL peak of CdSe/ZnS QDs. (a) PL spectra at different pressure. (b) Energy and FWHM of PL peak as a function of pressure

9.3 Results and discussions

Pressure dependent PL spectra for CdSe/ZnS QDs are shown in Fig. 9.2(a). A blue shift in the emission band with increasing pressure was observed. The most striking feature of the pressure dependent PL data is that the FWHM for the PL band decreases approximately 30% (from 38nm to 26nm) while the PL peaks shifted toward high energy as shown in Fig. 9.2(b). This result is opposite to high pressure studies of CdSe[7] and InP QDs.[12] The mechanism of the decrease in the FWHM of the PL peak is not clear at the moment. One possible reason is that defects induced by interfacial lattice mismatch (ca.12%), which commonly lead to broadening in the PL peak. As CdSe has a smaller bulk modulus (533 kbar) as compared to that of ZnS (760kbar), the mismatch is greatly reduced under higher pressure. The decrease of defects states leads to narrower electron population.[13] i.e., pressure induced surface optimization. The observation of decrease in PL intensity with pressure is signatures of carrier transfer to indirect conduction band states. The emission band is basically quenched above 69 kbar, indicating the phase transition from direct band-gap wurtzite to indirect band-gap rocksalt phase is complete.

The pressure-induced energy shifts of the optical transition related to the direct energy gap are plotted in Fig. 9.2(b). The open triangle corresponds to the PL energy. The solid line is the least-square fit to the experimental data using a quadratic equation:

$$E = E_0 + \alpha P + \beta P^2 \quad (1)$$

where the energy E is in eV and the pressure P is in kbar. The pressure coefficients α and β derived from fit to experimental data are 4.53 meV/kbar and -2.63×10^{-2} meV/kbar, respectively. The values are comparable to that of bulk CdSe (4.81 and -1.9×10^{-2} meV/kbar) [14] and 4.4-nm sized CdSe QDs (4.5 meV/kbar, linear fit). [6]

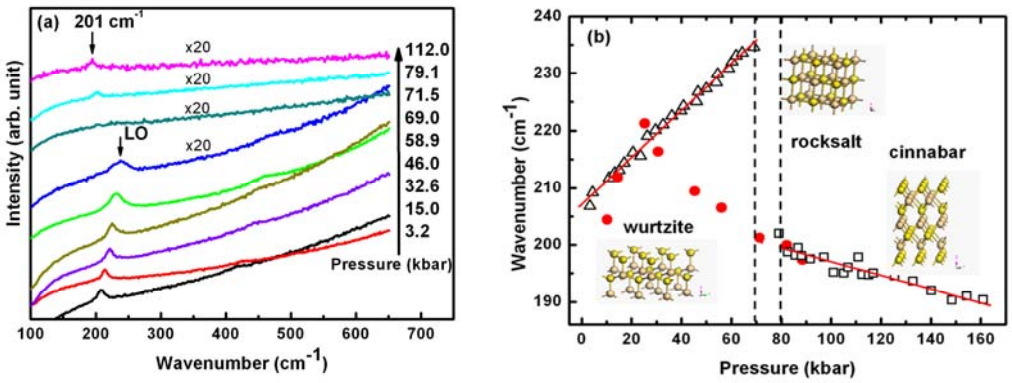

Fig. 9.3. Pressure dependence of phonon frequencies of CdSe/ZnS QDs. (a) Raman spectra at different pressure. (b) Frequency of Raman peaks as a function of pressure. Inserts show their corresponding structures at different pressures.

The resonance Raman spectra of CdSe/ZnS QDs at different pressure are shown in Fig. 9.3(a). Below 69 kbar, the resonance Raman spectra of CdSe/ZnS QDs is dominated by the LO phonon mode and the peak shifted linearly to higher frequencies with pressure. The LO peak disappears at 69 kbar which is the same pressure for the disappearance of PL peak. The disappearance of the LO phonon mode is attributed to the wurtzite to rocksalt phase transition as first-order Raman scattering of the rock-salt phase is inactive. Compared with wurtzite-rocksalt transition pressure for

bulk CdSe (27-30 kbar) and 4.4 nm-CdSe QDs (63 kbar), the elevated transition pressure for CdSe/ZnS QDs is attributed to higher surface free energies arose from the finite size effect and the reconstruction of the surface by ZnS. In the pressure range of 70 to 79 kbar, no peak was observed. At pressures higher than 79 kbar, a weaker peak appeared around 201 cm^{-1}. With increasing pressure, this peak linearly shifted toward lower frequencies. The peak remains visible at the pressures up to 160 kbar. The possibility of local impurity phonon mode of Zn or S interstitial in CdSe core formed by high pressure can be ignored, because no impurity phonon mode was observed at second upstroke below 79 kbar. The observation of the peak near 201 cm^{-1} here indicates another phase transition. This phase transition of CdSe core was not found in both CdSe QDs and the bulk CdSe before.

The transition of CdSe from rocksalt to the CsCl structure is predicted at 940 kbar.[15] However, the existence of transitions to other intermediate phases between rocksalt and CsCl at lower pressures could not be excluded. The theoretical calculation performed by Côté[16] has considered the cinnabar and Cmcm structures as possible intermediate phases. High pressure Cmcm structure of CdSe was found above 270 kbar by Nelmes.[17] In accordance with Côté's calculation, the total energy of cinnabar structure is close to that of the rocksalt structure. Therefore, we suggest the phase transition at 79 kbar is rocksalt to cinnabar structure transformation and the peak is CdSe TO phonon mode in cinnabar structure. Similar pressure dependence of TO phonon mode was also observed in ZnSe.[18] In fact, the phase transition at 79 kbar was not observed for bare CdSe QDs. It seems that the ZnS shell may serve to induce

nucleation of cinnabar structure (a distortion of rocksalt) on the surface of CdSe core at high pressure.

The Raman scattering of CdSe/ZnS QDs in the downstroke of pressure was also recorded. One Raman peak can be observed all the time during whole process. As shown in Fig. 9.3(b), the peak (circle) shifted up at first, and subsequently shifted down at pressures lower than 25 kbar. The abrupt change in slope of $d\omega/dP$ represents the phase transition from high-pressure phase to wurtzite. Noted that transition point in the downstroke of pressure is not constant, we repeated the experiment and found it was in the range of 20 to 40 kbar, which is typical of first order phase transition.

The open triangles and squares correspond to the LO and TO Raman modes of the CdSe core in the upstroke of pressure in Fig. 9.3(b). The solid line is the least-square fit to the experimental data using a linear pressure dependent fit function:

$$\omega_{LO}=207.16 + 0.41P \quad (2)$$

$$\omega_{TO}=209.16 -0.12P \quad (3)$$

where ω was the wavenumber in cm^{-1}. The value of vibrational pressure coefficients of LO mode are in good agreement with the CdSe QDs (>2.8nm).

9.4 Conclusion

In conclusion, we have studied the pressure induced electronic states and phase transition properties of CdSe/ZnS QDs up to 160 kbar using PL and Raman spectroscopy in conjunction with diamond-anvil cell technique. The PL peaks were found to narrow down with pressure, which represents the reduction of defect states. In our pressure range, two phase transitions were observed: wurtzite-rocksalt at 69 kbar and another phase transition at 79 kbar which may be attributed to rocksalt-cinnabar structure transformation. The pressure coefficients for Raman modes were derived from experimental data. These results for CdSe/ZnS QDs show a significant difference from the CdSe QDs as well as corresponding bulk materials, implying the ZnS shell play a dominant role in electronic state and structure phase transition properties under pressure.

9.5 References

[1]. M. Stockman, Nature Mater. **2004**, 3, 423.
[2]. D. Alexander, J. Bruce, C. Zuhlke, B. Koch, R. Rudebusch, J. Deogun and H. Hamza, Optics lett. **2006**, 31, 1957.
[3]. H. Mattoussi, J. M. Mauro, E. R. Goldman, G. P. Anderson, V. C. Sundar, F. V. Mikulec, and M. G. Bawendi, J. Am. Chem. Soc. **2000**, 122, 12142.
[4]. B. O. Dabbousi, J. Rodriguez-Viejo, F. V. Mikulec, J. R. Heine, H. Mattoussi, R. Ober, K. F. Jensen, M. G. Bawendi, J. Phys. Chem. B **1997**, 101, 9463.
[5]. A. P. Alivisatos, T. D. Harris, L. E. Brus, and A. Jayaraman, J. Chem. Phys. **1988**, 89, 5979.
[6]. S. H. Tolbert, A. P. Alivisatos, Science **1994**, 265, 373.
[7]. R. W. Meulenberg and G. F. Strouse, Phys. Rev. B **2002**, 66, 035317.
[8]. J. Z. Jiang, L. Gerward, R. Secco, D. Frost, J. S. Olsen, J. Thruckenbrodt, J. Appl. Phys. **2000**, 87, 2658.
[9]. Z. Y., Wu, Z. X. Bao, L. Cao, C. X. Liu, Q. S. Li, B. S. Zou, J. Appl. Phys. **2003**, 93, 9983.
[10]. K. Hashizume, M. Matsubayashi, M. Vacha, T. Tani, J. Lumin. **2002**, 98, 49.
[11]. A. V. Baranow, Y. P. Rakovich, J. F. Donegan, T. S. Perova, R. A. Moore, D. V. Talapin, Phys. Rev. B **2003**, 68,165306.
[12]. C. S. Menoni, L. Miao, D. Patel, O. I. Mic'ic' and A. J. Nozik, Phy. Rev. Lett. **2000**, 84, 4168.
[13]. D. V. Talapin, I. Mekis, S. Götzinger, A. Kornowski, O. Benson, H. Weller, J. Phys. B **2004**, 108, 18826.
[14]. W. Shan, W. Walukiewicz, J. W. Ager III, K. M. Yu, J. Wu, E. E. Haller, Appl. Phys. Lett. **2004**, 84, 67.
[15]. O. Zakharov, A. Rubio andM. L. Cohen, Phys. Rev. B **1995**, 51, 4926.
[16]. M. Côté, O. Zakharov, A. Rubio, and M. L. Cohen, Phys. Rev. B **1997**, 55, 13025.
[17]. R. J. Nelmes, M. I. Mcmahon, Semicond. Semimetals **1998**, 54, 145.
[18]. C. M. Lin, D. S. Chuu, T. J. Yang, W. C. Chou, J. A. Xu, E. Huang, Phys. Rev. B **1997**, 55,13641.

Chapter 10

Conclusion and Future Work

This thesis contains three parts: First, spectroscopic studies of graphene were carried out; Second, Raman spectroscopy was used to investigate a new kind of carbon nanomaterial – carbon nanowalls (CNWs); Third, two popular semiconductor QDs (ZnCdSe and CdSe/ZnS QDs) were investigated by Raman and PL spectroscopy under high pressure.

10.1 Spectroscopic studies of graphene

1. We have demonstrated that by using contrast spectra, we can easily determine the number of graphene layers. We have also calculated the contrast using the Fresnel's equations and the results show an excellent match with the experimental data. From the simulation, we extracted the refractive index of graphene below ten layers as n_z=2.0-1.1i, which is different from that of bulk graphite. Our experimental values can be directly used as a standard to identify the thickness of graphene sheet on Si substrate with ~300 nm SiO_2 capping layer. We have also given an analytical expression for determining number of layers. From the contrast image, we have demonstrated the effectiveness of this new technique. Although current research mainly focuses on the single and bilayer graphene, we believe that the few-layer (less than 10 layers) graphene also have interesting properties as they still exhibit the

two-dimensional properties. Reflection and contrast spectroscopy provides a fast, non-destructive, easy-to-use, and accurate method to identify the numbers of graphene layers (below 10 layers), which helps future research and application of graphene.

2. Raman spectroscopy studies of graphene with one to four layers have been carried out. The results show that the zone boundary phonon, two-phonon, and the three-phonon modes show broadening and blueshift as the graphene thickness increases. We propose that the double resonance theory in together with the electron-hole interactions can be used to explain these phenomena. The anisotropy of excitons in graphene play an important role, and the energy difference of intra- and inter- layer excitons are about 400 meV, which were calculated from the excitation energy dependent Raman results. Therefore, in addition to the single particle behaviors within graphene layer systems, the excitonic effect e-h interaction should be also taken into account to understand their electronic and optical properties in further experimental and theoretical studies.

3. We have used Raman spectroscopy to investigate the influence of top gate insulator (5 nm SiO_2) on graphene sheets mainly in two important aspects, defects and strain. The results show that defects were introduced in graphene sheets during deposition and the amounts of defects increase as the graphene thickness decreases. After annealing, the defects in graphene can be greatly reduced. Moreover, significant Raman shifts of all the bands of graphene were observed after SiO_2 deposition and annealing, which was attributed to the compressive strain on graphene caused by the SiO_2 top layer. Importantly, the strain can be controlled by the annealing temperature,

which maybe used to tune the optical and electronic properties similar to what has been observed in CNTs. Finally, it was found that the graphene thickness can be modified in a controllable manner using anneal. Our findings provide useful information critical to graphene device engineering and fabrication.

10.2 Raman spectroscopic investigation of CNWs

1. All the observed Raman peaks of CNWs were assigned and compared with that of CNTs and graphite. No radial breathing mode (RBM) was observed, which is the characteristic of CNTs. The G mode of CNWs had a slightly higher frequency and was also broader than that of graphite, which can be attributed to the breakdown of selection rule caused by the small size of CNWs. Different laser lines were used to excite the sample. The frequency of the D band shifts with the laser energy at a rate of 46.19 cm^{-1}/eV, and this result agrees well with the theoretical value by double resonance effect. The 2D and D+G bands shift at the rate of 107.5 cm^{-1}/eV and 48.98 cm^{-1}/eV respectively. The decreasing intensity ratios I_D/I_G and $I_{D'}/I_G$ with the increasing laser energy are observed and discussed.

2. High temperature Raman experiments were carried out on carbon nanowalls (CNWs). The intensity of the defect-induced D mode decreased significantly after the sample was heated up in air ambient. The Raman intensity ratio of D mode and G mode, I_D/I_G, changed from 2.3 at room temperature to 1.95 after the sample was heated to 600℃. This change was attributed to the removal of surface amorphous

carbon by oxidation. In contrast to I_D/I_G, the intensity ratio of D′ mode and G mode, $I_{D'}/I_G$, did not change much after the heating, indicating that the surface amorphous carbon and surface impurity do not contribute as much to the intensity of D′ mode. The finding also indicates that the dominant contributor to the D′ mode could be the intrinsic defects. Through this work, we have provided evidence that although the D′ mode is defects induced, it may have different origin of defects from the D mode.

10.3 High pressure Raman and PL spectra study of semiconductor QDs (ZnCdSe and CdSe/ZnS QDs)

1. Raman and PL study of wurtzite alloy $Zn_xCd_{1-x}Se$ (x=0.2) QDs were carried out under hydrostatic pressure up to 130 kbar at room temperature using the diamond anvil cell technique. The structural phase transition from wurtzite to rocksalt, indicated by the disappearance of both PL and Raman peaks, was observed at 71 kabr. Besides, the abrupt change of PL pressure coefficient and Raman peak splitting were observed at about 25.8 kbar, which may indicate a new unidentified structural phase transition of the alloy QDs. The results of alloy ZnCdSe QDs differ greatly from that of bare CdSe or ZnSe QDs as well as the corresponding bulk materials, implying that the quantum size effect plays an important role in the structure stability of the alloy QDs.

2. Pressure-dependent PL and Raman spectroscopic study of CdSe/ZnS core/shell QDs were also presented. The PL and Raman measurements were performed as a function of applied hydrostatic pressure up to 160 kbar. The PL and Raman peaks

shifted toward higher energy with increasing pressure. The full width at half maximum (FWHM) for PL peaks was found to decrease approximately 30%, which represents the reduction of defect states. Two phase transitions at 69 and 79 kbar were found, and they correspond to wurtzite-rocksalt and rocksalt-cinnabar structure transformation, respectively. The high pressure cinnabar structure of CdSe was predicted by theoretical calculation and has confirmed for the first time in this experiment. The experimental results of CdSe/ZnS QDs show significant difference from those of CdSe QDs as well as bulk CdSe, implying the ZnS shell plays a dominant role in structure stability and electron state of such system.

The above works on ZnCdSe and CdSe/ZnS QDs suggest that analyzing both the high pressure Raman and PL spectra is a good strategy for the study of structural stability of semiconductor QDs, since it can provide information of the materials both in terms of energy bandgap and crystal structure changes under high pressure.

10.4 Future work

For the spectroscopic studies of graphene, further studies include: 1. Raman studies of electron-phonon coupling of graphene under the electric field. In this part, the electrical field can tune the band structure of graphene, which will affect the Raman spectra and show interesting phenomena. 2. High pressure Raman studies of graphene. The 2D structured graphene may exhibit different properties from that of bulk graphite and carbon nanotubes. 3. Polarization Raman studies of graphene

nanoribbons. Graphene nanoribbons is a 1D carbon nanomaterials which has been predicted to have extraordinary properties, i.e. the edge of nanoribbon can tune the nanoribbon from semiconductor to metallic. The polarization Raman studies of this 1D structured material may give the information of how the edge affects the properties.

For the Raman study of CNWs, several aspects are still unclear. In the high temperature Raman study of CNWs, it was found that CNWs has a much greater thermal coefficient (0.029 cm^{-1}/K) than that of graphite (0.011 cm^{-1}/K). It was speculated that this difference was caused by the great amount of defects and small domain size of CNWs. However, the different intrinsic (pure) temperature effects of CNWs and graphite could also be the reason. High temperature experiments needs to be carried out to address this issue. The thermal coefficients of CNWs, single-wall CNTs, multi-wall CNTs, and graphite with different amount of defects can be compared to identify the role of pure temperature effect on the thermal coefficient of carbon materials.

For the high pressure study of $Zn_xCd_{1-x}Se$ QDs, the new structural phase transition at about 25.8 kbar is still unassigned. It could be a wurtzite to zincblende phase transition, or a phase transition to an intermediate phase between wurtzite and rocksalt. Further high pressure x-ray diffraction experiment is necessary to clarify this new phase transition. Moreover, experiments on $Zn_xCd_{1-x}Se$ QDs with different zinc composition should also be carried out. Such experiments may provide information on how the compositions of alloy QDs affect the structural stability of alloy QDs.

For the high pressure study of CdSe/ZnS QDs, since the ZnS shell plays a dominant role in structure stability and electron state of the core/shell system, it will be very interesting to carry out further study on QDs with different shell thickness, or different materials of shell. These future works can provide clearer information on how the shell affects the structure of QDs.